

6. STUDY OF ALUMINIUM RODS

6.1 Introduction

The work presented here was performed by Anne Marie Habraken with the help of Wang Xiao Chuan thanks to the Dynamic Forging Modeling project supported by the Région Wallonne. Then Zhang Li Hong and Sylvie Castagne have brought their collaboration to improve Bodner's and Zhu's models.

The manufacturing process of the studied aeronautic rod has been provided by Technical Airborne Components industry; it consists in 3 stages of rotary forging: preliminary round-round forging, round-rectangle pre-crushing and final rectangle-rectangle forging as summarized by Figure 6-1. The rotary forging process is described by Figure 6-2 showing longitudinal and transversal views and by Figure 6-3 presenting the hammer system of a forging machine.

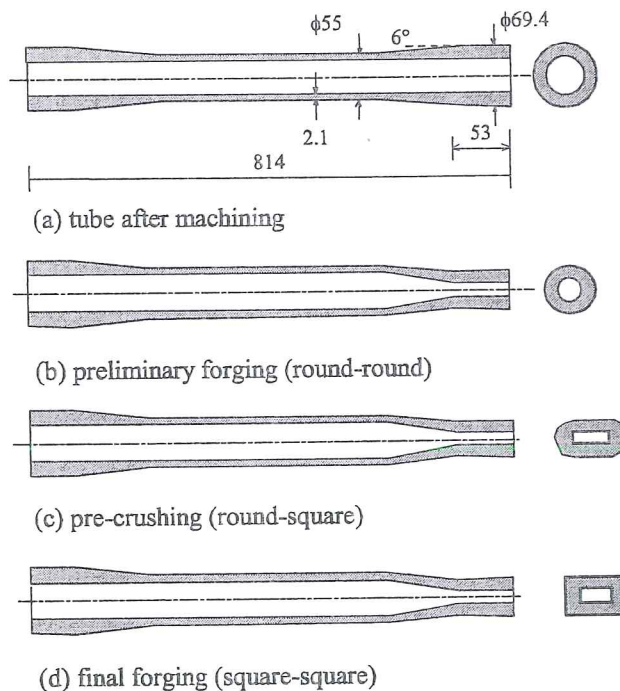


Figure 6-1 Industrial aeronautic rod manufacturing process (adapted from Wang & Habraken 1996).

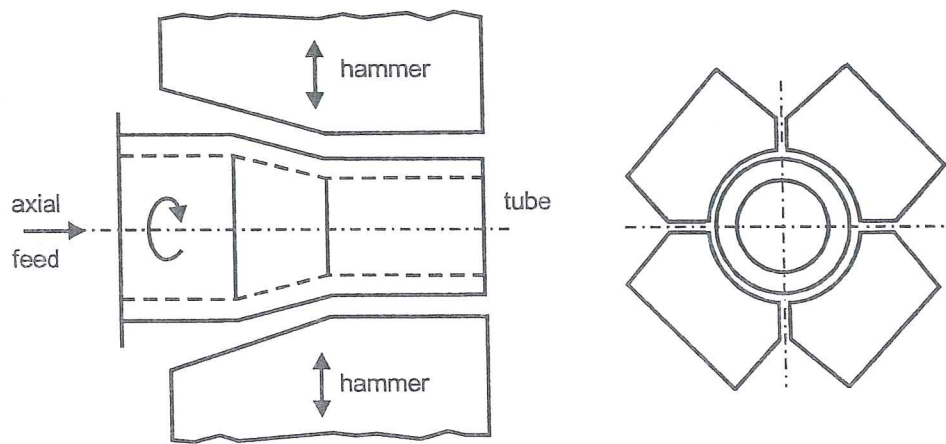


Figure 6-2 Studied rotary forging process (from Habraken & Wang 1996).

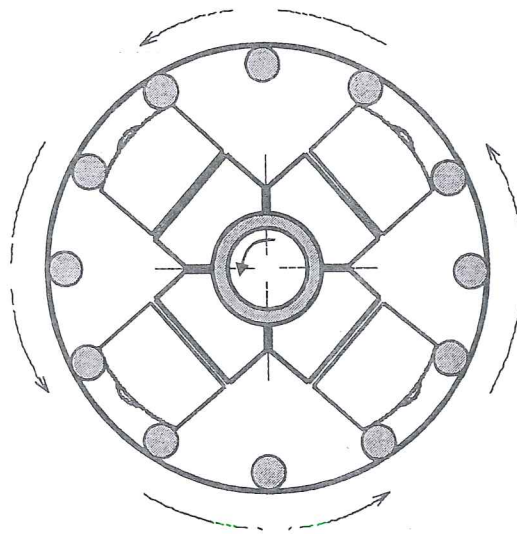


Figure 6-3 Hammer system of a forging machine (from Wang *et al.* 1995).

In fact, if relative rotation between rod and hammers exists, the circular shape of the tube is retained; otherwise the hammer shape is progressively imposed on the tube. Of course, the FE simulation requires the tools and the tube geometry and a kinetic description of the process; however the difficulties concern general choices:

- Isothermal mechanical simulation or thermomechanical one?
- Static or dynamic analysis?
- Elasto-plastic or elasto-visco-plastic assumption?
- Best strategy to represent numerically the round-round forging by an axisymmetric state?

All these points were studied and details can be found in Wang *et al.* 1994a, Wang *et al.* 1994b, Wang *et al.* 1995, Wang & Habraken 1996. The general automatic simulating procedure is summarized by Figure 6-4, and FEM results are presented on Figure 6-5.

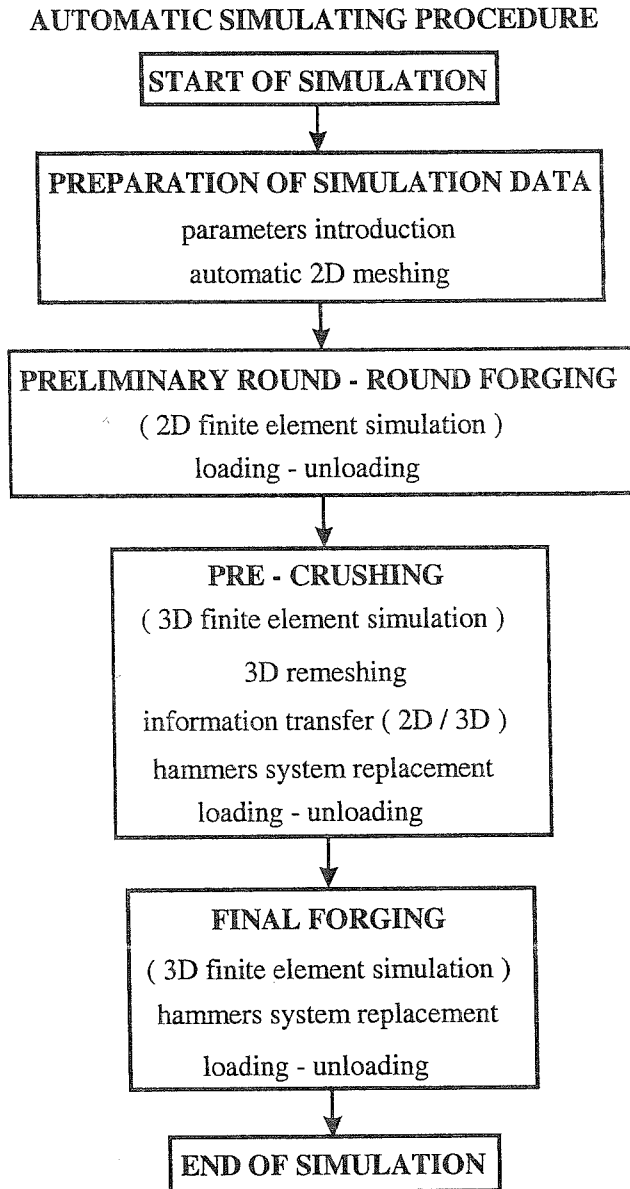
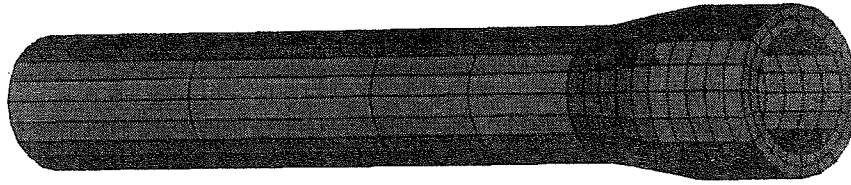
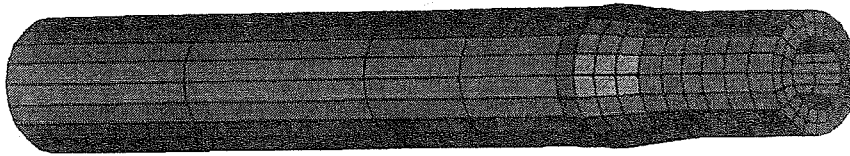


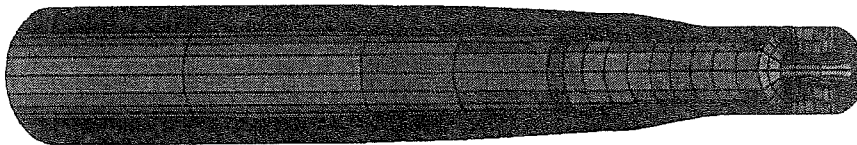
Figure 6-4 Automatic simulation procedure (adapted from Wang *et al.* 1995)



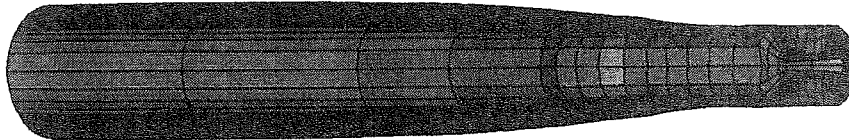
FINITE ELEMENT MESH (2D)



PRELIMINARY FORGING SIMULATION 2D



PRE-CRUSHING SIMULATION 3D



FINAL FORGING SIMULATION 3D

FE MODELLING OF FABRICATION PHASES OF AERONAUTIC RODS

Figure 6-5 Forged tube after different manufacturing steps, (adapted from Wang & Habraken 1996)

The various heat treatments applied between the forging steps prevent to really stick to the real process in this research, because the constitutive law was just identified once on the annealed state, and not 3 times, after each heat treatment. Nevertheless, it is interesting to note that Bodner's damage model presented hereafter could predict zones of maximum damage where the industry effectively observed cracks (Figure 6-6). This model allows a parametrical study, which could help to decrease damage according to process conditions.

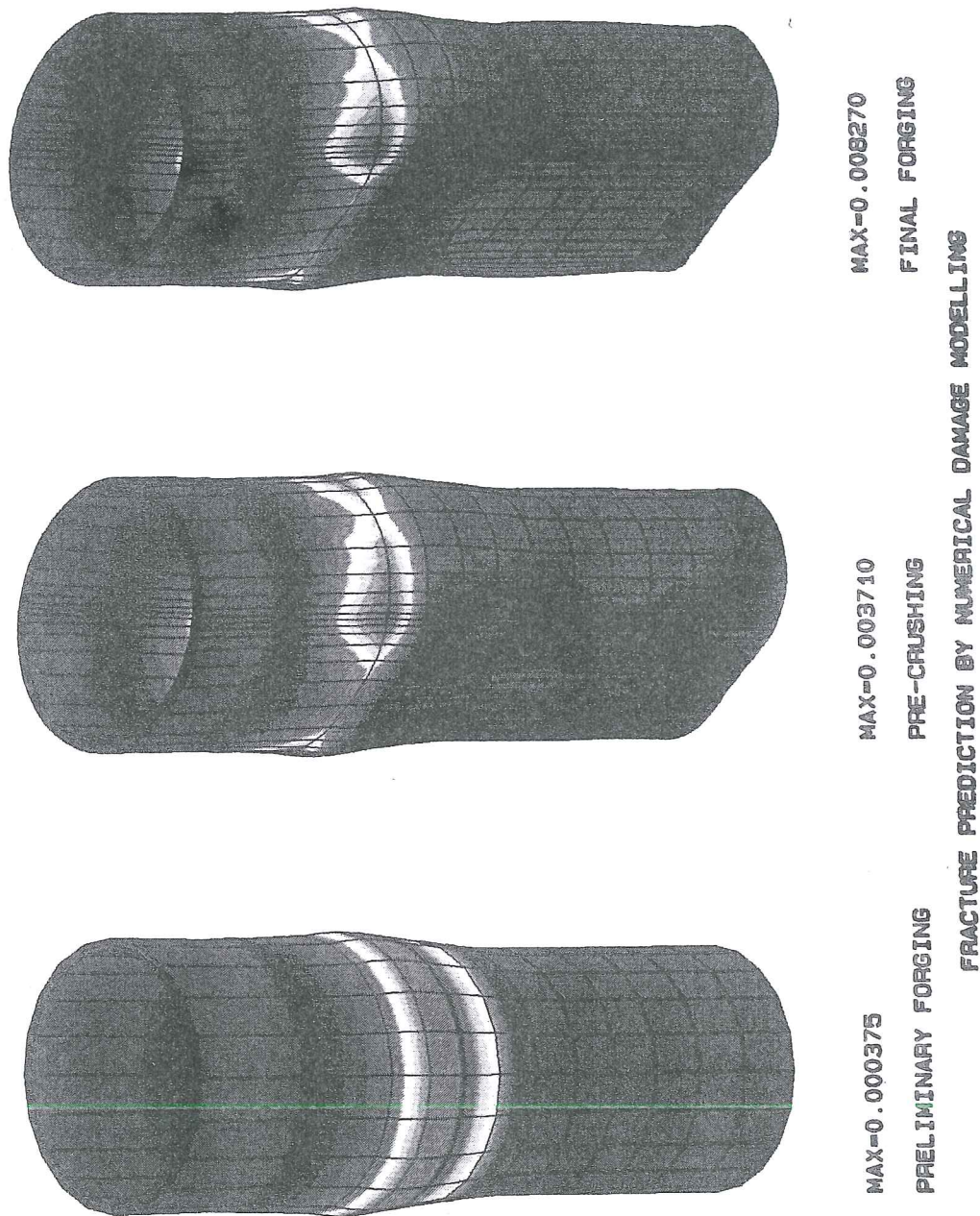


Figure 6-6 Damage distribution after different manufacturing steps (from Wang & Habraken 1996).

Note that as described in Habraken & Wang 1996, for notch test experiments and two cases of cylinder upsetting, 6 criteria from Chapter 4, table 4-1 (Freudenthal, Cockroft, Brozo, Ghosh, Oyane, Mc Clintock) have been applied with the stress and strain fields computed with Bodner's damage model. The conclusion was that for this

set of experiments it was not possible to find one criterion able to predict the right location of fracture with a unique threshold value.

The goal of this thesis is not to summarize all this project results, they can be found in the final project reports (Cescotto *et al.* 1993, Habraken *et al.* 1996). The thesis provides the description of the two damage models that were applied on the annealed state of the rod material (Aluminum alloy 2024). This material was only available in form of tubes (see Figure 6-7), which explains the chosen shape of samples for identification and validation experiments. A clear weakness of this research is the lack of microscopic investigations on the material. This task was not in the Région Wallonne project and the efforts to perform it after the end of the project have failed. Present closer links with the metallurgical department should avoid such a mistake in the future.

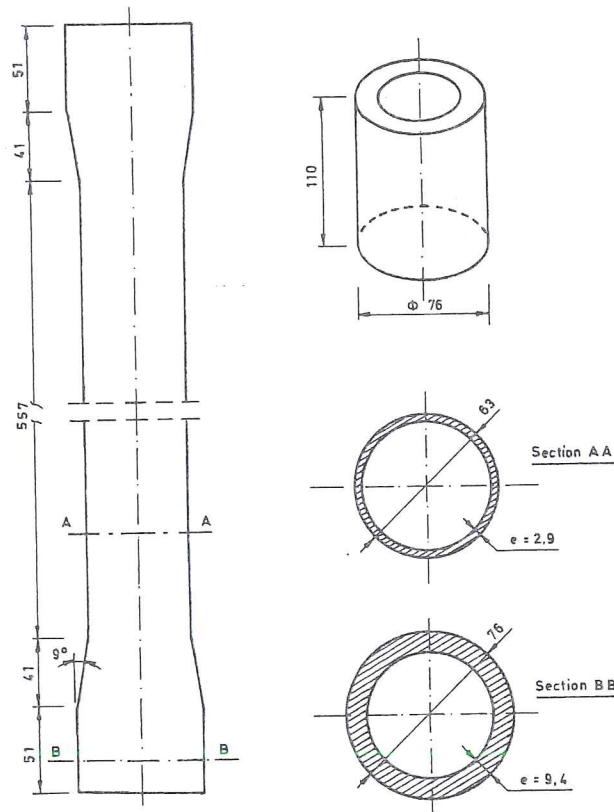


Figure 6-7 Description of the tube (Habraken & Wang 1996).

Respecting chronological order, the elasto-visco-plastic damage model of Bodner's type is first described (section 6.2) with its identification and validation, then the damage elasto-plastic law of Zhu is applied on the same experimental data (section 6.3). All the simulations are performed with 2D and 3D finite elements of mixed type (Zhu & Cescotto, 1994b, 1995b) implemented in the LAGAMINE code.

6.2. An elastic-visco-plastic-damage model

6.2.1. The model choice

The literature review by Zhu & Cescotto 1991 about elasto-visco-plastic models easily coupled with damage and able to represent material behavior in various conditions of strain rates and temperatures has pointed out the qualities of the Bodner & Partom's 1975 model. The article of Zhu & Cescotto 1994 collects the parameters of Bodner Partom's model for a large number of metals and alloys which proves the large application field of this law.

This literature analysis explains the choice of this model to be implemented in LAGAMINE. The simulations of the process of aluminum rod forging have shown that strain rate could reach 50 s^{-1} . The experimental tests demonstrate a low viscous effect at room temperature. As one particularity of Bodner's model is its application to material with low viscosity, this law has been adopted. This low viscous aspect help to regularize the problem and to prevent numerical strain localization (see Chapter 5). This was effective as proved by the problems encountered further (section 6.3) with the application of damage elasto-plastic model.

6.2.2. Bodner's constitutive law

The model is first described in its initial state without damage extension. The general formulation of Bodner's model (Bodner & Partom, 1975) is based on the additive decomposition of $\underline{\dot{\epsilon}}$ the total strain rate tensor, symmetric part of the velocity gradient tensor, into $\underline{\dot{\epsilon}}^e$ elastic and $\underline{\dot{\epsilon}}^p$ inelastic components which are both non-zero for all loading and unloading conditions:

$$\underline{\dot{\epsilon}} = \underline{\dot{\epsilon}}^e + \underline{\dot{\epsilon}}^p \quad (6-1)$$

The elastic behavior follows the classical Young's law, here written separately for the deviatoric Cauchy's stress tensor $\underline{\hat{\sigma}}$ and the mean stress value σ_m . As in previous sections, hereafter the superscript \wedge identifies a deviatoric tensor, the superscript ∇ the objective Jaumann's rate and the subscript m a mean tensor value, G and χ are respectively the elastic shear and bulk moduli, computed from Young's modulus E and Poisson's ratio ν .

$$\begin{aligned} \underline{\hat{\sigma}}^\nabla &= 2G(\underline{\dot{\epsilon}}^\wedge - \underline{\dot{\epsilon}}^p) \\ \dot{\sigma}_m &= 3\chi\dot{\epsilon}_m \end{aligned} \quad (6-2)$$

The generalized Prandtl-Reuss' flow law is used together with the volume conservation to establish a tensorial relation between deviatoric Cauchy's stress $\hat{\sigma}$ and inelastic strain rate $\dot{\epsilon}^p$:

$$\dot{\epsilon}^p = \frac{D_o}{\sqrt{J_2}} \exp\left(-\frac{1}{2}\left(\frac{Z^2}{3J_2}\right)^n\right) \hat{\sigma} \quad \text{with} \quad J_2 = \frac{1}{2} \hat{\sigma} : \hat{\sigma} \quad (6-3)$$

where D_o is an assumed limit value of plastic strain rate in shear for large J_2 , n is the rate sensitivity coefficient, Z is a total scalar hardening variable, sum of an isotropic part K and a directional part Z_D :

$$Z = K + Z_D \quad (6-4)$$

The directional component Z_D is computed by the projection of $\underline{\beta}$, a directional hardening symmetric tensor, on the direction \underline{u} of the stress tensor:

$$Z_D = \underline{\beta} : \underline{u} \quad \text{with} \quad \underline{u} = \underline{\sigma} / \sqrt{\underline{\sigma} : \underline{\sigma}} \quad (6-5)$$

When the stress direction \underline{u} is strongly modified, the directional component Z_D undergoes large magnitude changes and affects material response. This is the physical meaning of the scalar directional hardening component Z_D . Let us note that such concept is also used for hardening by Phillips *et al.* 1974, Basuroychowdhury & Voyiadjis 1998.

The isotropic and directional hardening are both assumed to occur under the action of two simultaneously competitive mechanisms: a hardening process due to deformation (first term of relations 6-6 below) and a softening or recovery process evolving with time and temperature (represented by the second term of relations 6-6):

$$\dot{K} = m_1 (K_1 - K) \dot{W}^p - A_1 K_1 \left(\frac{K - K_2}{K_1}\right)^{r_1} \quad (6-6a)$$

$$\dot{\underline{\beta}} = m_2 (D_1 \underline{u} - \underline{\beta}) \dot{W}^p - A_2 K_1 \left(\frac{\sqrt{\underline{\beta} : \underline{\beta}}}{K_1}\right)^{r_2} \frac{\underline{\beta}}{\sqrt{\underline{\beta} : \underline{\beta}}} + (\underline{\Omega} \cdot \underline{\beta} - \underline{\beta} \cdot \underline{\Omega}) \quad (6-6b)$$

where \dot{W}^p is the plastic work rate. The initial value of K at zero inelastic strain is K_0 ; K_1 is the maximum value of K , K_2 is the minimum value of K at a given temperature at which creep is occurring. The initial and minimum value of $\underline{\beta}$ is zero corresponding to the isotropic state. m_1 , A_1 , r_1 , m_2 , A_2 , r_2 are material parameters defining the hardening evolution laws. The last term of equation (6-6b) is due to Jaumann's objective correction used for large strains, where $\underline{\Omega}$ is the antisymmetric part of the velocity gradient tensor.

Bodner's model is totally defined by 14 parameters : $E, \nu, D_o, K_o, K_1, K_2, D_1, m_1, m_2, A_1, r_1, A_2, r_2$ and n . At room temperature, the terms related to the thermal recovery can be omitted and the number of parameters is reduced to 10.

6.2.3. Damage theory

Two scalar damage variables, called d the deviatoric component and δ the volumetric component, are used to represent the average material degradation which reflects the various types of damage at the micro-scale (see section 3.2.1 for the definition of damage variables). The damage due to nucleation, growth and coalescence of voids, to micro-cracks and to other microscopic defects is globally represented by d . And δ . According to Ladevèze 1984, these two variables are necessary to modify both elastic modulus and Poisson's ratio with damage growth.

As already presented in chapter 3, the continuum damage approach assumes the existence of a "true" stress tensor $\underline{\sigma}$ computed from macroscopic loading and area measurements and an associated "effective" stress tensor $\overline{\underline{\sigma}}$ theoretically closer to the actual average microscopic stress state existing between defects. The equivalent virgin state is related to the average material state, once the defects have been dropped. It is represented by effective tensors indicated by the superscript $\bar{\cdot}$. The developed model is a phenomenological one, not directly deduced from micro-macro transition. So, contrary to Gurson 1977 or Perzyna 1986 models, a direct connection between damage variables and void volume fraction is not assumed; other defect types could be covered by these damage components. As usual, true and effective stress tensors are related through the damage variables d and δ :

$$\overline{\underline{\hat{\sigma}}} = \frac{\underline{\hat{\sigma}}}{(1-d)} \quad \overline{\sigma}_m = \frac{\sigma_m}{(1-\delta)} \quad (6-7)$$

From the viewpoint of energy conservation (Cordebois & Sidoroff 1979), the energy equivalence seems to be of more physical significance, so the following relation is applied in the elastic part:

$$\overline{\underline{\hat{\varepsilon}}^e} = \underline{\hat{\varepsilon}}^e (1-d) \quad \overline{\varepsilon}_m^e = \varepsilon_m^e (1-\delta) \quad (6-8)$$

So one can check from (6-7) and (6-8) that elastic energy is equal in both states. Concerning plasticity, the plastic work rate \dot{W}^p is conserved, this leads to:

$$\overline{\underline{\hat{\varepsilon}}^p} = \underline{\hat{\varepsilon}}^p (1-d) \quad (6-9)$$

The damage evolution law comes from the one proposed by Lemaître 1985. It has been adapted to a multiaxial state and a two damage variables model:

$$\dot{d} = \frac{1}{2(1-d)} \left(\frac{\langle F(\underline{\sigma}) - \sigma_D \rangle}{A(1-d)} \right)^s \dot{\varepsilon}_{eq}^r \quad (6-10)$$

with $\langle x \rangle = x$ if $x > 0$ and $\langle x \rangle = 0$ if $x \leq 0$ and where $F(\underline{\sigma})$ is a triaxiality function necessary to transform a triaxial stress state to a reference uniaxial state, σ_D is a threshold value for damage increase, A, r, s are material constant. The chosen triaxiality function is the following one which has the advantage to separate tensile, compression and shear stress states and to introduce only one new parameter α :

$$F(\underline{\sigma}) = (1 - \alpha)\sqrt{3J_2} + 3\alpha\sigma_m \quad (6-11)$$

One should notice that the so-called deviatoric damage component is not strictly dependent on shear component J_2 as the triaxiality function is modified by the mean stress σ_m .

The volumic damage variable evolution is directly related to the deviatoric damage component evolution and reflects the assumption of no volumic damage increase in compression state :

$$\begin{aligned} \dot{\delta} &= \frac{\delta}{d} \dot{d} \quad \text{in tensile state } \sigma_m > 0 \\ &= 0 \quad \text{in compression state } \sigma_m \leq 0 \end{aligned} \quad (6-12)$$

It has been checked experimentally that the ratio δ/d can be assumed constant in tensile state for common materials (Gattoufi, 1984). This ratio is named τ , so finally damage is characterized by 6 parameters : $A, r, s, \sigma_D, \alpha, \tau$. This model allows to recover the well-known Kachanov's creep law for $\tau = 1, s = \sigma_D = 0$.

6.2.4. Damage extension of Bodner's model

According to damage theory, effective stress and strain tensors follow classical behavior law. Consequently replacing $\underline{\sigma}$ by $\bar{\underline{\sigma}}$ and $\underline{\varepsilon}$ by $\bar{\underline{\varepsilon}}$ in Bodner's relations (6-1) to (6-6) and using relations (6-7) to (6-9) between true and effective tensors, one can get the final equations:

$$\bar{\underline{\dot{\sigma}}} = 2G(1-d)^2(\underline{\dot{\varepsilon}} - \underline{\dot{\varepsilon}}^p) - 4G(1-d)(\underline{\dot{\varepsilon}} - \underline{\dot{\varepsilon}}^p)\dot{d} \quad (6-13)$$

$$\dot{\sigma}_m = 3\chi(1-\delta)^2\dot{\varepsilon}_m - 6\chi(1-\delta)\varepsilon_m\dot{\delta} \quad (6-14)$$

$$\underline{\dot{\varepsilon}}^p = \frac{D_o}{\sqrt{J_2(1-d)}} \exp\left(-\frac{1}{2}\left(\frac{Z^2(1-d)^2}{3J_2}\right)^n\right) \bar{\underline{\dot{\sigma}}} \quad (6-15)$$

Z hardening variable is assumed equal in the actual damaged state and in the equivalent virgin state, since, its evolution is mainly defined by the plastic work rate which is equal in both states.

6.2.5. Numerical integration technique

The elasto-visco-plastic laws are well-known to be stiff and difficult to integrate. Another problem is related to the time consuming matrix inversions necessary to perform iterations at the constitutive law level. The integration scheme proposed by Zhu & Cescotto 1994 for their Bodner's model version has been extended to the present damage Bodner's model. In fact, this scheme applies previous work from Szabo 1985 and Dombrovsky 1992. The summary of the integration scheme has been published in Habraken *et al.* 1995; it will not be reproduced here.

6.2.6. Identification, general principle

The parameter identification procedure is summarized by Figure 6-8. The parameters for the damage evolution laws and Bodner's parameters applied on effective behavior in the equivalent virgin state are first computed separately thanks to different experimental tests. Then the model defined by this parameter set is used to simulate uniaxial tensile and compression states and to compare the model results to experimental curves. The final parameters set is reached thanks to an optimization process that modifies the less accurate experimentally defined parameters to reduce the difference between simulated and experimental values.

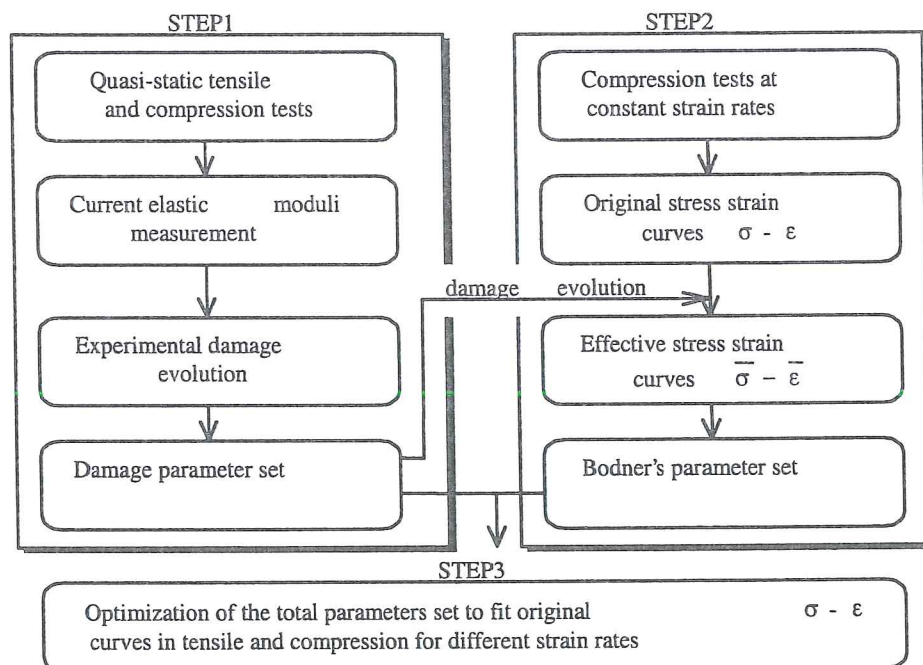


Figure 6-8 Summary of parameter identification procedure for damage Bodner's model (from Habraken *et al.* 2000).

This approach has been preferred to a global inverse procedure in order to preserve the physical meaning of each parameter.

Each step of this parameters identification procedure is now described for the chosen annealed aluminum. This material is only available under the form of tubes of limited thickness (see Figure 6-7).

6.2.7. Damage parameters identification

A. Tensile tests

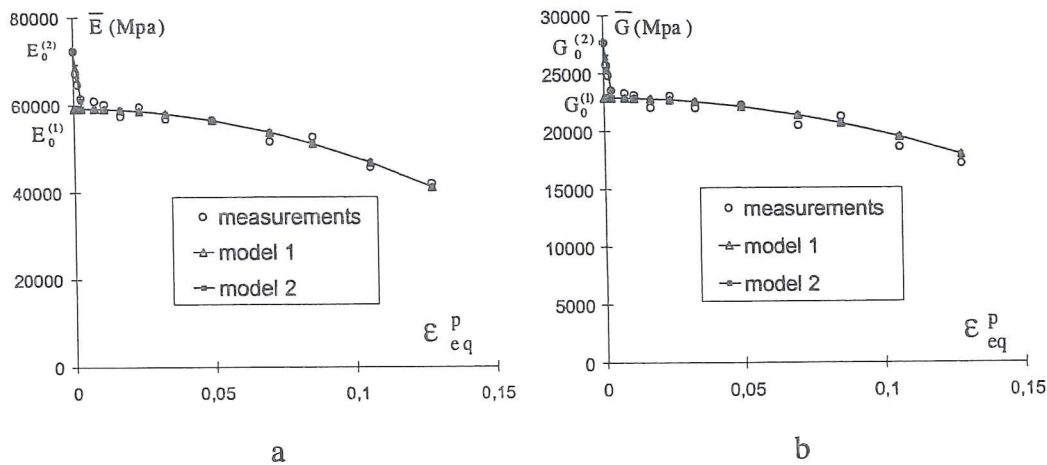


Figure 6-9 Moduli measurements and models versus plastic strain for quasi-static tensile tests, a) apparent Young's modulus, b) apparent shear modulus (from Habraken *et al.* 2000).

Cyclic loading and unloading quasi-static tensile tests performed on the whole tube allow to measure Young's and shear moduli evolution. Figures 6-9a and b show the experimental results and two possible representative analytical curves which neglect or not the phenomena occurring at the beginning of plasticity. The two damage variables are directly deduced from these measures:

$$d = 1 - \sqrt{\frac{\bar{G}}{G_0}} \quad \delta = 1 - \sqrt{\frac{\bar{\chi}}{\chi_0}} \quad (6-16)$$

where $\bar{\chi}$ is the bulk modulus computed by:

$$\bar{\chi} = \frac{\bar{E} \cdot \bar{G}}{3(\bar{3G} - \bar{E})} \quad (6-17)$$

Figure 6-10a and b show the experimental damage evolutions as well as reduced curves used further as explained in part C. of this section.

According to the classical macroscopic damage theory as described by Lemaître & Chaboche 1985, extrapolated value of Young's and shear moduli $E_o^{(1)}, G_o^{(1)}$ (see Figure 6-9) should be used. This gives damage values growing in a monotonic way from zero as represented by model 1 curves on Figure 6-10a and b. The difference between the elastic moduli $E_o^{(2)}, G_o^{(2)}$ and their extrapolated values $E_o^{(1)}, G_o^{(1)}$ is assumed to be related to plasticity entrance and not to damage as specified by Chevalier 1988 in his thesis.

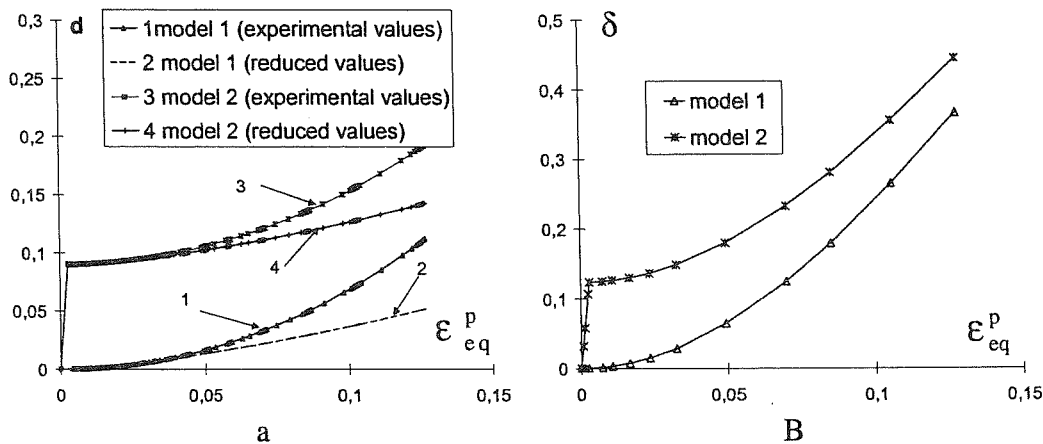


Figure 6-10 Experimental damage evolutions in tensile state according to model 1 or 2, a) deviatoric damage d , b) volumic damage, δ (from Habraken *et al.* 2000).

However looking to the damage theory proposed by Gurson 1977 or one of its late versions (Leblond *et al.* 1995), this fact could also be linked to a void nucleation rate that increases the void volume fraction very quickly at plasticity entrance and is followed by a smoother void growth rate. In the present aluminum 2024 alloy, optic microscopy has demonstrated the presence of precipitates which show a matrix decohesion after plasticity entrance. Such a phenomenon is not seldom. For instance in Pardoën's thesis 1998, which is dedicated to copper and is based on numerous electronic microscopic analyses, an initial void volume fraction is assumed to take into account the precipitate decohesion, that appears after microscopic strain.

Here, as the present research has no real microscopic part and is based on a macroscopic model, it has been decided to work with two assumptions: damage is computed according to $E_o^{(1)}, G_o^{(1)}$ or $E_o^{(2)}, G_o^{(2)}$. Of course this affects the numerical modeling and leads to verify two models: Model 1, where damage evolution is defined according to equations (6-10) and (6-12), and Model 2, where damage follows a quick linear increase at plasticity entrance and, afterwards, respects equations (6-10) and (6-12).

The constant damage ratio $\tau = \delta / d$ assumption is "reasonably" verified. Its variation is [3.24, 4.12] for Model 1 and [1.37, 2.30] for Model 2.

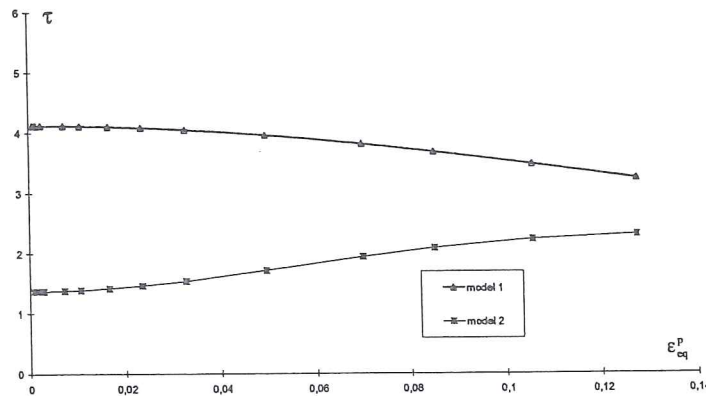


Figure 6-11 Experimental damage ratio in tensile state for model 1 and 2 (from Habraken *et al.* 1999).

B. Compression tests

First, small cubes extracted from the tube wall were compressed in order to check the isotropic behavior of the material. Then cyclic loading and unloading were performed on small cylinders (diameter 7 mm, height 7 mm) and Young modulus was deduced from the force measure and from the press table displacement corrected by the press stiffness estimated from a test without sample. The table lubrication and straightness were carefully checked to avoid barreling and non-uniform contact.

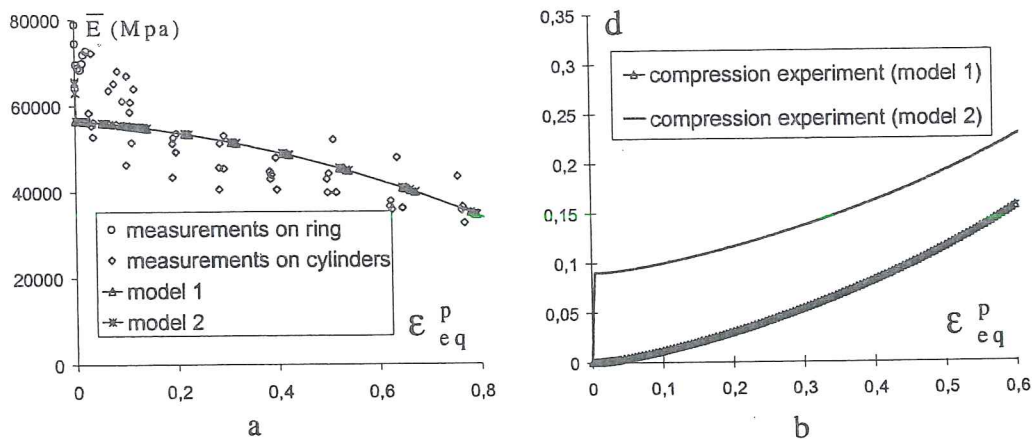


Figure 6-12 Compression state, a) apparent Young's modulus measurements versus plastic strain, b) experimental deviatoric damage (from Habraken *et al.* 2000).

The experimental results present however some dispersion (Figure 6-12a) even if the decreasing character of the modulus is corroborated. To improve accuracy, cyclic compression tests on a ring (slice of the tube) have been performed in the range of

small plastic strains. Here the sample size allows the use of strain gages and a second set of experimental points has been added on Figure 6-12a. Finally, the initial Young's modulus in compression test (78915 MPa) is slightly higher than in tensile state (72250 MPa). It has been assumed that this variance is due to different presses and different measurement techniques. To reach damage parameters in compression, thanks to relations (6-16) and (6-17), effective shear modulus measurements should be available. Practical problems, related to the sample geometry and the barreling for large strain, prevent to measure this modulus accurately. Adding the assumption of no volumic damage in compression (equation 6-12) yields the following relation:

$$d = 1 - (1 - D) \sqrt{\frac{E_0}{3G_0 - 3G_0(1 - D)^2 + E_0(1 - D)^2}} \quad (6-18)$$

where D is the classical damage parameter in a "one damage variable" model :

$$D = 1 - \sqrt{\frac{\bar{E}}{E_0}} \quad (6-19)$$

So, the experimental deviatoric damage evolution is deduced from Figure 6-12a and relations (6-18), (6-19). It is presented on Figure 6-12b.

C. Damage parameters identification

Let σ be the actual value of the stress in uniaxial tests, then F the triaxiality function defined by relation (6-11) is straightforward:

$$F_r(\underline{\sigma}) = (1 - 2\alpha)^\theta \sigma \quad (6-20)$$

with $\theta=0$ in tensile state and 1 in compression state.

For model 1, the integration of the damage evolution law defined by equation (6-10) results in the following relation:

$$d = 1 - \left(1 - \frac{(S + 2)(1 - 2\alpha)^\theta}{2A^S} \int_0^{\varepsilon_{eq}^p} \sigma^S d\varepsilon_{eq}^p\right)^{1/S+2} \quad (6-21)$$

if no strain rate effect on damage evolution ($r=1$) and no threshold value ($\sigma_D=0$) are assumed. These additional hypotheses are related to the experimental damage observations (Figure 6-10a and Figure 6-12b) and to the low viscosity effect observed in section 6.2.8 for this aluminum. For model 2, the principle is identical except that the damage evolution law is first linear until damage has reached a transition value.

The problem is now reduced to a classical inverse method: knowing relation (6-21) and experimental curves (Figure 6-10a and Figure 6-12b) find the best parameters set (S, α, A), that minimizes differences between model and experiments. In fact for tensile state, the reduced values (Figure 6-10a) and not the experimental ones have been used as a target value. This choice, that slows down damage evolution in

tension in the model, was imposed because, otherwise, it was impossible to reach an effective reference curve $\bar{\sigma}_{eq} - \bar{\epsilon}_{eq}$ compatible with tensile and compression experimental curves (see Figure 6-13). Using a reduced damaged curve in traction leads to doubts about both experimental works and theoretical assumptions. One possible explanation is that, due to various thermal treatments applied to the aeronautic rod, the sets of rods used for the tensile tests and for all other tests were different. A posteriori microscopic investigation presents some variance according to the sample origin. Another possibility is a severe lack of accuracy in the damage measurements of tensile tests. However, this is unlikely because, as reported in Wang 1996 and Habraken, Zhang and Wauters 1997, the tests performed on the whole rod have used different types of strain gages and extensometers that yield similar results. A final possibility is the existence of a scale effect in the measurement devices or in the material. Recall that the macroscopic length of all samples covers a quite large scale as the rod diameter is 75 mm and its thickness varies from 9.4 to 2.9 mm. Notch and small compression samples were cylinders of diameter 7 mm, when all other samples were quite larger.

		Model 1	Model 2
S	Stress function exponent in damage model	2,006	2,5274
A (MPa)	Stress function constant in damage model	256.74	250
σ_D	Damage threshold stress	0	0
R	Exponent of equivalent strain rate in damage model	1	1
α	Triaxiality function parameter	0.216	0.2136
d_1	Transition deviatoric damage value (model 2)	0	0,09
ϵ_{eq1}	Transition equivalent strain value (model 2)	0	0,0029

Table 6-1 Parameters sets for damage models 1 and 2 (from Habraken *et al.* 2000).

Table 6-1 summarizes the final damage parameter sets provided by the inverse modeling method. One can check that tensile state is the driving mechanism for damage increase, then comes shear state, and finally compression state. So a tensile state coupled to a large triaxiality ratio leads to the fastest deviatoric damage increase.

6.2.8. Bodner's parameters identification

A. Quasi-static uniaxial tests

The damage evolution defined by the parameter sets from Table 6-1 and equations (6-7) to (6-12) allows the computation of effective curves $\bar{\sigma}_{eq} - \bar{\epsilon}_{eq}$, once experimental curves $\sigma_{eq} - \epsilon_{eq}$ are known.

Applied to quasi-static uniaxial tensile and compression tests ($\dot{\epsilon} = 0.004s^{-1}$), this procedure provides an effective curve $\bar{\sigma}_{eq} - \bar{\epsilon}_{eq}$ that models the actual microscopic behavior of the material in both states (see Figure 6-13). This result was made possible only by adopting reduced values for tensile damage.

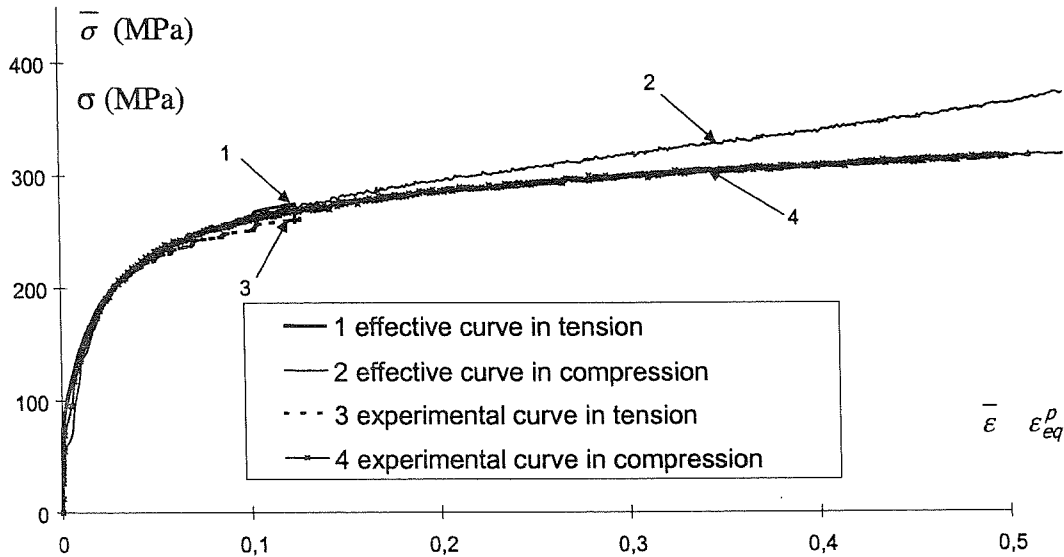


Figure 6-13 Experimental and effective stress strain curves in compression and tensile state for quasi-static experiment, Model 1 (from Habraken *et al.* 1999).

It must be noted that the plastic strain reached during tensile tests is much smaller than in compression. The range $0 \leq \epsilon_{eq}^p \leq 0.12$ covered by tensile tests (Figure 6-9a) corresponds to the region of maximum scatter of the compression results (Figure 6-12a).

B. Compression tests at various strain rate

The experimental device being used is limited to cylindrical samples of 7 mm height for a $20 s^{-1}$ constant strain rate. This strain rate level already means an initial punch velocity of 140 mm/s. For $20 s^{-1}$ constant strain rate, an upsetting test stopped at a strain of 70% is performed in 0.035 second. So, one cannot neglect the temperature increase due to plastic dissipation during the test. Considering classical thermal coefficient for an aluminum and using an adiabatic assumption lead to a temperature increase of $\approx 80^\circ\text{C}$. The temperature dependence of the material behavior has been checked by quasi-static uniaxial compression tests at room temperature (16.5°C) and at 100°C .

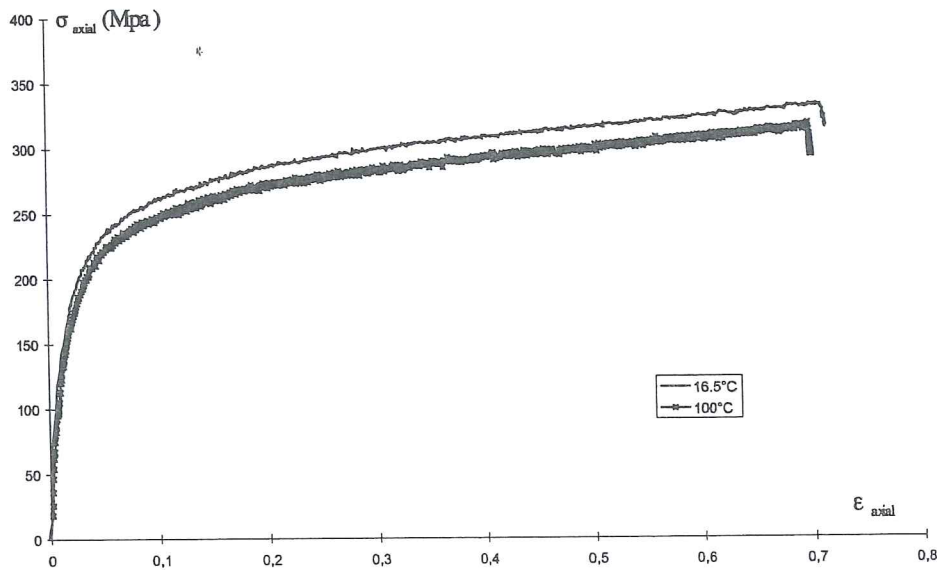


Figure 6-14 Stress strain curves for quasi-static compression tests performed at 16.5°C and 100°C (from Habraken *et al.* 1999).

So using a temperature effect issued from preceding tests, a quasi-adiabatic assumption (for tests performed at $\dot{\epsilon} = 10 \text{ s}^{-1}$ and 20 s^{-1}), as well as the damage evolution law (model 1) defined in preceding sections, the effective stress strain curves (Figure 6-15b) are deduced from experiments (Figure 6-15a).

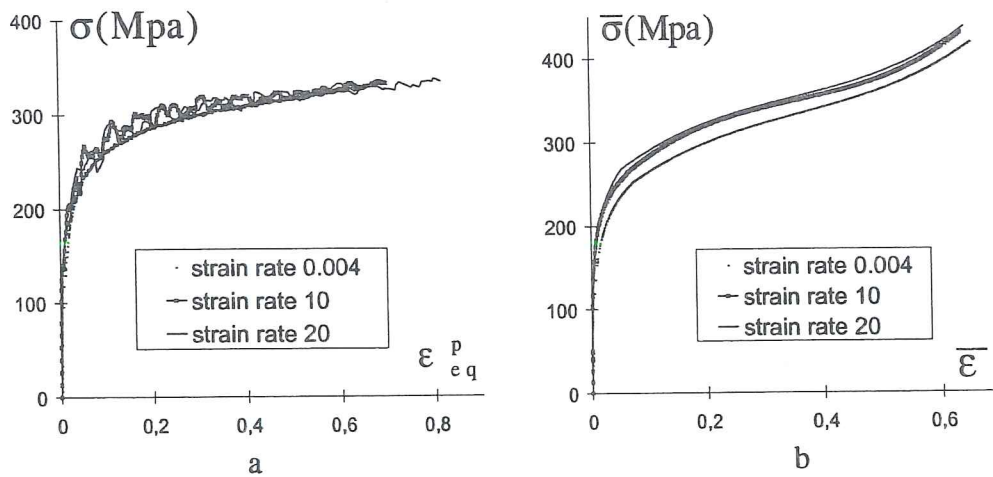


Figure 6-15 Compression at constant strain rates, a) experimental stress strain curves, b) computed effective stress strain curves (from Habraken *et al.* 2000).

Even if the stability of the performed large strain rate tests is limited, Figure 6-15a allows to verify that the viscous effect on this material is limited for the considered

strain rates. The accuracy of computed effective curves (Figure 6-15b) is poor due to the rough thermal correction and the low stability of experimental tests (Figure 6-15a).

C. Bodner's parameters identification

The applied identification procedure of Bodner's parameters partially comes from Chan *et al.* 1988. Bodner's law for a uniaxial test is expressed by the following scalar relation:

$$\frac{\sigma}{Z} = \left[2 \ln \left(\frac{2D_o \sigma}{\sqrt{3} \dot{\epsilon}^p |\sigma|} \right) \right]^{-1/2n} = g \quad (6-22)$$

where $\sigma / |\sigma| = -1$ for uniaxial compression and $\dot{\epsilon}^p$ is constant for the selected tests. As D_o , assumed limit of plastic shear strain rate, is chosen by the user, the constant g is easily computed for each experiment once n is known. At room temperature, the thermal softening effect is negligible, so isotropic and directional hardening laws are reduced to their first term (relations 6-6a and b). Additionally for uniaxial tests, $\underline{\beta}$ the directional symmetric tensor is reduced to one non zero component equal to the directional parameter Z_D . The hardening relations are then:

$$\dot{K} = m_1 (K_1 - K) \dot{W}^p \quad \text{with } K(0) = K_o \quad (6-23)$$

$$\dot{Z}_D = m_2 (D_1 - Z_D) \dot{W}^p \quad \text{with } D(0) = 0 \quad (6-24)$$

$$Z = K + Z_D \quad (6-25)$$

The function $\gamma(\sigma)$, derivative of the stress with respect to plastic work, is then used to find m_1 and m_2 . Its definition and previous relations (6-22 to 6-25) lead to:

$$\gamma(\sigma) = \frac{d\sigma}{dW^p} = g (m_1 (K_1 - K) + m_2 (D_1 - Z_D)) \quad (6-26)$$

Theoretically this function defines 2 linear parts:

-for small plastic strain, isotropic hardening is equal to K_o while directional hardening is increasing:

$$\begin{aligned} K &= K_o \\ Z_D &= Z - K_o = \frac{\sigma}{g} - K_o \end{aligned} \quad (6-27)$$

-for large plastic strain, directional hardening has reached its saturation level D_1 while isotropic hardening is increasing:

$$Z_D = D_1$$

$$K = Z - D_1 = \frac{\sigma}{g} - D_1 \quad (6-28)$$

This theoretical approach is represented on Figure 6-16 which also defines saturation stress σ_s and coefficient a . However, the function γ issued from the effective stress strain curves represented on Figure 6-15b is quite far from this theoretical shape, which leaves quite a large range to chose m_1 and m_2 .

The value of the saturation stress σ_s can be used to find n , the strain rate sensitivity coefficient. Relation (6-22) and the definition of σ_s recalled on Figure 6-16, give :

$$\ln \sigma_s = -\frac{1}{2n} \ln \left(2 \ln \frac{2D_o}{\sqrt{3}\dot{\epsilon}^p} \right) + \ln (K_1 + D_1) \quad (6-29)$$

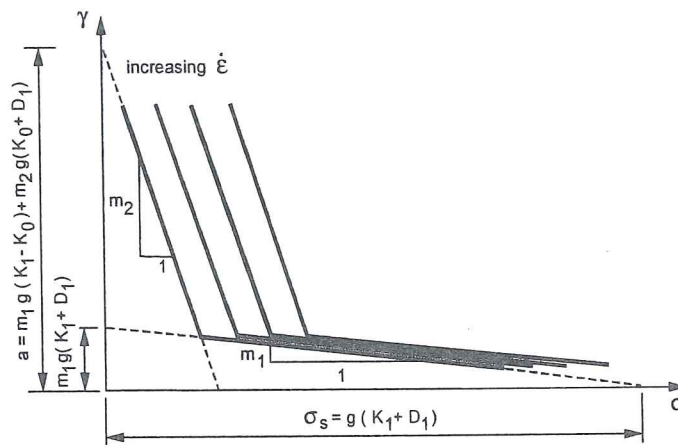


Figure 6-16 Function $\gamma(\sigma)$ for an ideal theoretical case (Habraken *et al.* 2000).

Again the performed tests do not yield co-linear points, which leaves some freedom to define the value of n . The hardening values are extracted from the stress strain curves, relation (6-22) and g value:

$$\sigma_o = g K_o$$

$$D_1 = \frac{\sigma_1}{g} - K_o \quad (6-30a,b,c)$$

$$K_1 = \frac{\sigma_s}{g} - D_1$$

where σ_o is the yield stress value, σ_1 the stress at saturation of directional hardening and σ_s the stress saturation value.

The preceding procedure helps to define the range of the different parameters. The final parameters set is then obtained by optimization. At this level, Tables 6-1 and

6-2 define the whole parameters set of the models 1 and 2 and one can check that simulated curves by Bodner's damage models (1 or 2) are near experimental ones on Figures 6-17a and b representing respectively stress and damage evolution with strain for uniaxial tests. The RR' line defines the experimental rupture in tensile state.

		Damage model 1	Damage model 2
Parameter	Physical meaning	Value set	Value set
E (MPa)	Young's modulus	72250	65660
ν	Poisson's coefficient	0,31	0.31
D_o (s^{-1})	Assumed limit plastic shear strain rate	10^8	10^8
K_o (MPa)	Initial isotropic hardness	106.584	99.506
K_1 (MPa)	Maximum isotropic hardness	341.744	358.661
K_2 (MPa)	Minimum isotropic hardness	106.584	99.506
D_1 (MPa)	Maximum directional hardness	231.445	239.131
m_1	Isotropic hardening parameter	0.091	0.0125
m_2	Directional hardening parameter	0.33	0.43
N	Strain rate sensitivity coefficient	5.5126	6.8524

Table 6-1 Bodner's parameters sets to recover effective stress strain curves, models 1 and 2 (from Habraken *et al.* 2000).

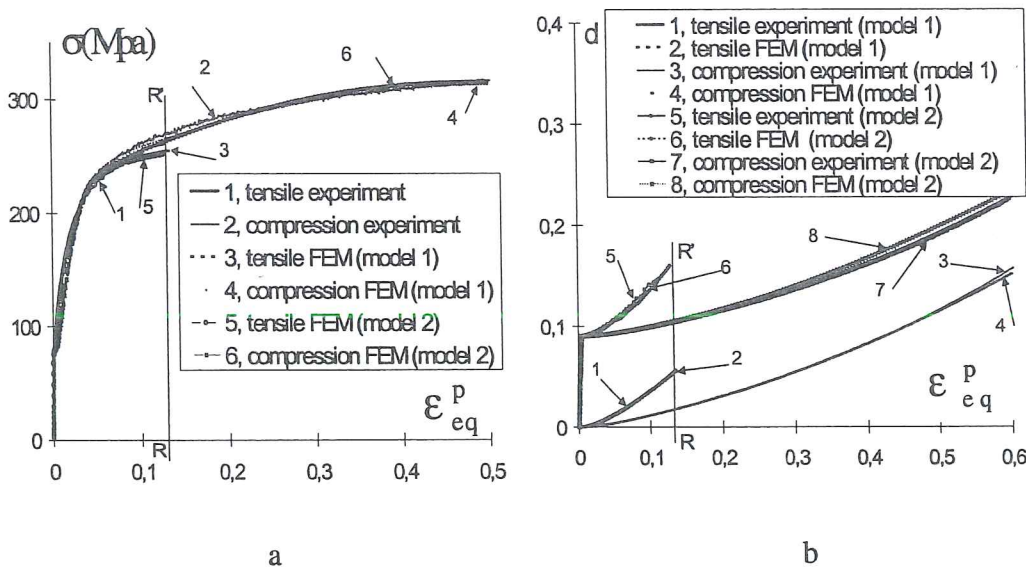


Figure 6-17 Experimental and simulation results in quasi-static tensile and compression state: a) stress-strain curves, b) deviatoric damage evolution with strain, experimental reduced curve in tension (from Habraken *et al.* 2000).

6.2.9 Definition of finite element size

As underlined in chapter 5, the size of the elements used in the mesh is important. So a sensitivity analysis has been performed.

The simulated experiment consists in a tensile test on a cylindrical bar presenting a narrow part in its middle. The geometrical details are given on Figure 6-18, the test is driven by the displacement of one extremity at the constant velocity of 0.005 mm/s while the elongation of the middle part is measured between points AA'.

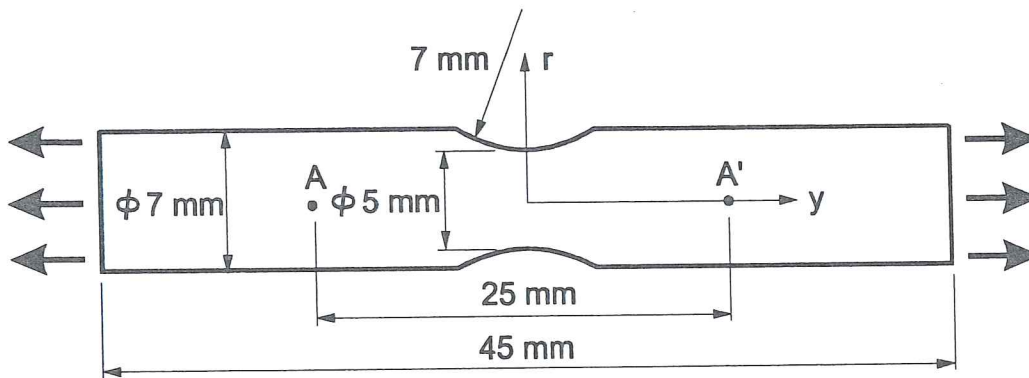


Figure 6-18 Sample description – Notch test (from Habraken *et al.* 2000).

Figure 6-19 presents the experimental global force-displacement curve for each of the four experimental tests. One can verify that the dispersion is quite low.

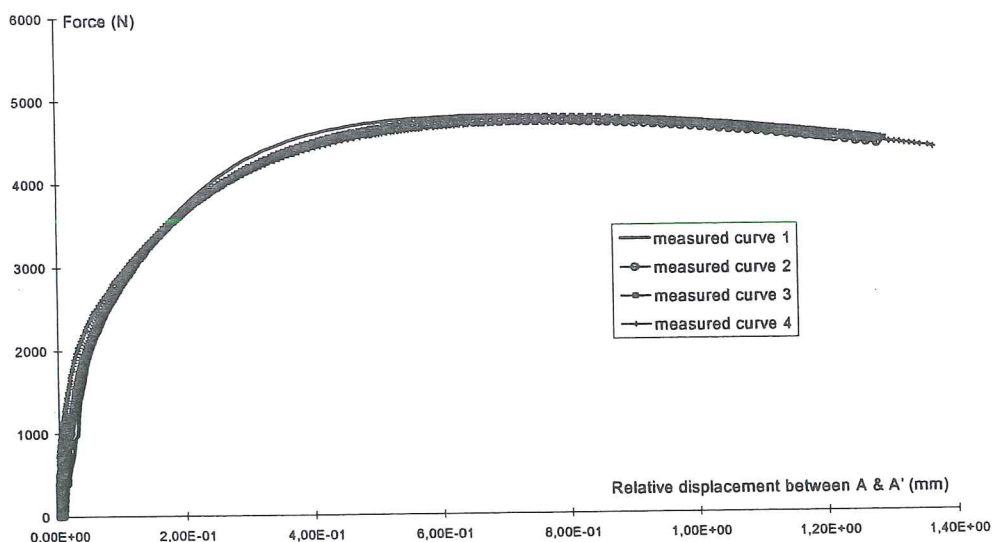


Figure 6-19 Force-displacement curve for the 4 notch test experiments.

The mesh dependence has been verified for the constitutive law using model 1 for the damage evolution rule. The simulations are performed in axisymmetrical state on one quarter of the sample by symmetry. Six different meshes (Figure 6-20) have been used to verify the stability of the simulation results. They differ by the mesh density at the notch level.

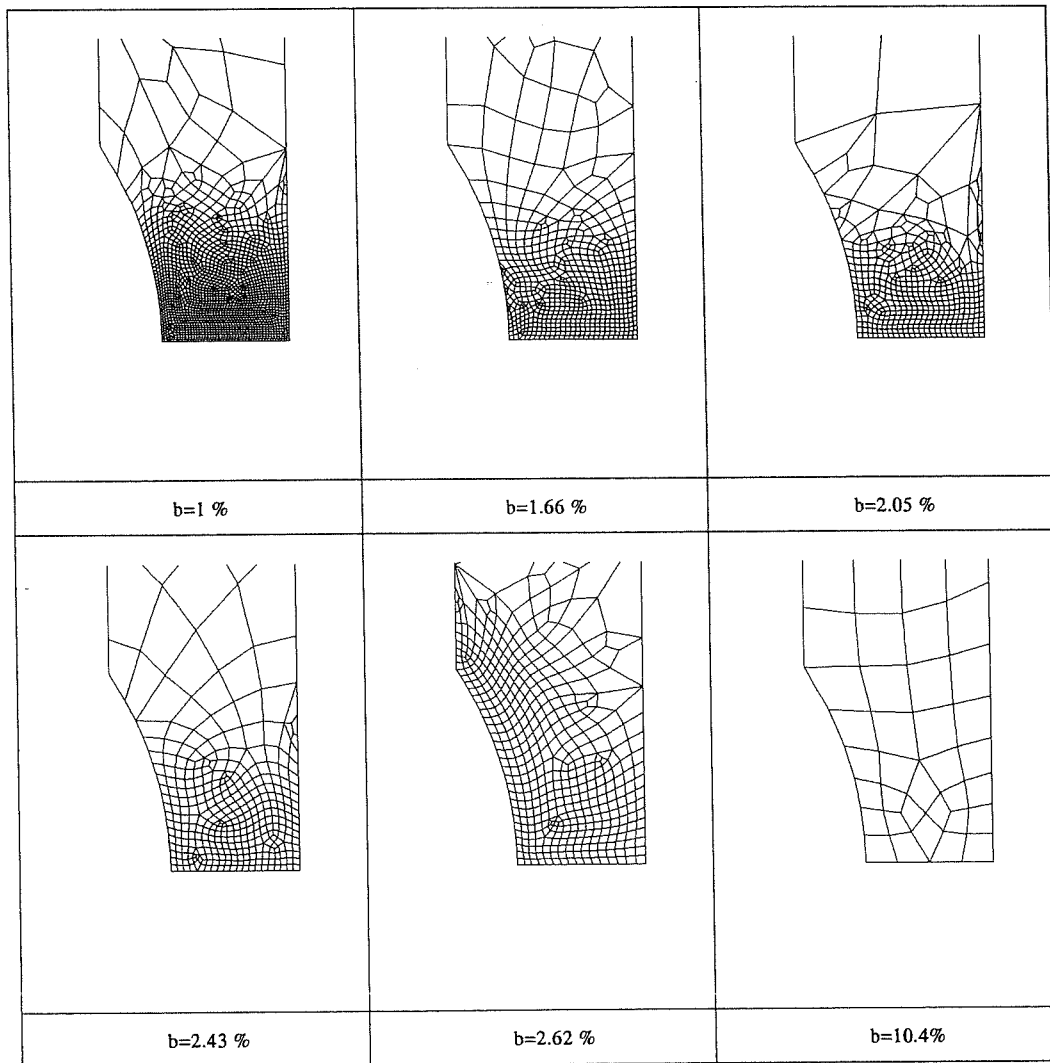


Figure 6-20 Mesh descriptions near the notch, b is the ratio between the diagonal of the smallest element and the notch radius (7 mm), from Habraken *et al.* 1999.

Figure 6-21 collects some of the results of the numerical simulations and one experimental curve since no significant experimental dispersion occurred. The RR' line at relative displacement of 0.96 mm represents what is called "the first experimental rupture". Because the global fracture appears quite later, this initial

rupture location could seem strange. However the force-time curve, not reproduced here, allows detecting the necking beginning for this relative displacement of 0.96 mm. For all other validation tests, the RR' line effectively identifies the moment when the first small macroscopic crack appears. According to the type of the structure, this happens nearly simultaneously or not with the global fracture. From the 4 types of tests described in following sections, the notch test is the only one presenting a clear "macroscopic" necking phase before rupture. As the present Bodner's damage model does not specifically simulate coalescence, necking beginning has been chosen as "experimental rupture" for the notch test analysis.

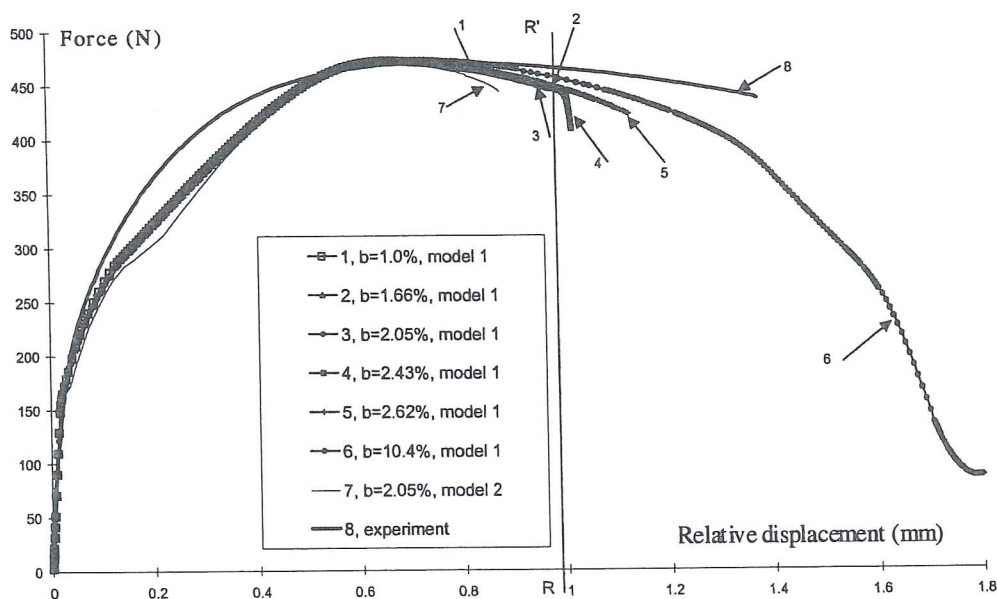


Figure 6-21 Experimental and simulation force-displacement curves, meshes are defined on Figure 6-20 (from Habraken *et al.* 2000).

Figure 6-21 global force-displacement curves show that the hardening model is not perfect, compared to the material behavior. This could have already been suspected from experimental and simulated tensile curves of Figure 6-17. Without serious modifications of the hardening description of Bodner's approach, it is not possible to improve this result. A good point is that the curve maximum is well predicted no matter model 1 or 2 is adopted for damage evolution. The mesh dependence of the result is not observed until this maximum is passed. Then depending on the mesh, the simulation stops because of non convergence, with or without noticeable slope variation in the global force elongation curve. So if this slope variation is taken as criterion for global rupture, simulation results are mesh dependent and not very consistent with experiments.

It is interesting to note that Rousselier 1987 uses the "load-diametral contraction" curve and more specifically its slope after crack initiation to determine accurately the

required finite element size. He applies finite element simulations with an elastoplastic damaged law to notch tests. Then he argues that, numerically, the collapse of the stress happens in the strongly damaged zone. So the growth rate of cracks depends on the finite element size l_c , at the tip of the crack. In ductile fracture, a classical size is the average distance between inclusions and Mudry 1982 proposes to derive l_c from the number of inclusions per unit of volume N_V :

$$l_{c0} = 2 \sqrt[3]{N_V} \quad (6-31)$$

In the present work, the different analyzed meshes have a typical finite element size varying from 0.17 mm to 0.75 mm near the crack initiation. The number of precipitates is unknown. The final experimental slope in the “force-displacement” curve (Figure 6-19) is unavailable either due to the velocity of the breakdown related to the small size of the sample. For the other experiments like the shear test (section 6.2.10 D), the bending test (section 6.2.10 C) and the tensile test of a perforated specimen (section 6.2.10 B), the final slopes of the load displacement curve have been registered and could be used to adjust l_c . However experimental dispersion does not provide accurate information. In conclusion, Rousselier’s approach to adjust finite element size has not been applied here. As the goal of the research is the rupture prediction and not the study of crack propagation, this is acceptable. Note that 2 parameters are responsible for the final slope in numerical simulations: the characteristic size l_c and the damage rate during coalescence and even after as, in the described approach, the elements still exist but with a vanishing stiffness.

Another other way to verify the mesh dependence of the results is to look at the damage variable map. This approach is often far more sensitive than a global force displacement curve. Figures 6-22a and b collect the deviatoric damage curves along r and y axes (defined on Figure 6-18) near the maximum of the global curve.

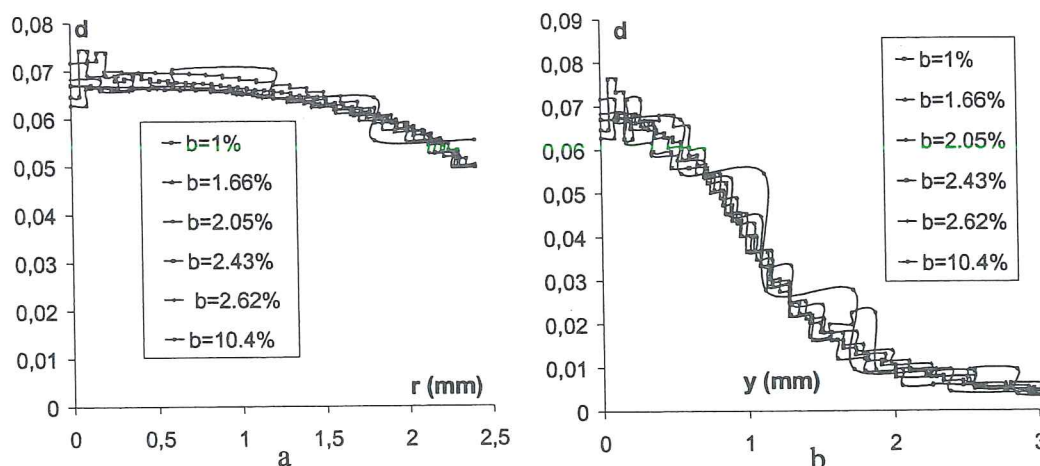


Figure 6-22 Deviatoric damage variable for an elongation of 0.65 mm of the base AA': a) along r axis, b) along y axis (from Habraken *et al.* 2000).

Figure 6-22a shows a small range of variation of the deviatoric damage value with the mesh except for the center point and the coarser mesh. The effect is slightly stronger on Figure 6-22b. Such local variations can explain why the simulation convergence is lost at different moments when damage increases. However, if some smoothing procedure is used to represent the deviatoric damage map, one will find that the level and size of the localized damage zone is quite identical for each mesh even the coarser one.

In conclusion, the damage map for this notch test simulation has a low mesh dependence. The b ratio taking into account the radius of other samples geometry will be used to have an idea of the mesh density in the following sections. In practice, for the validation simulations, the mesh refinement has been applied when the presence of discontinuities in the stress, strain or damage fields indicates errors due to too coarse discretization. As proved by the simulation of the bending test (section 6.2.10 C), the shape ratio of the element is also an important parameter.

6.2.10 Validation

The interest of a macroscopic damage approach consists in its application to different type of material loading. So four different experiments have been performed and simulated:

- tensile test of a notched specimen,
- tensile test of a perforated specimen,
- bending test,
- shear test of a perforated specimen.

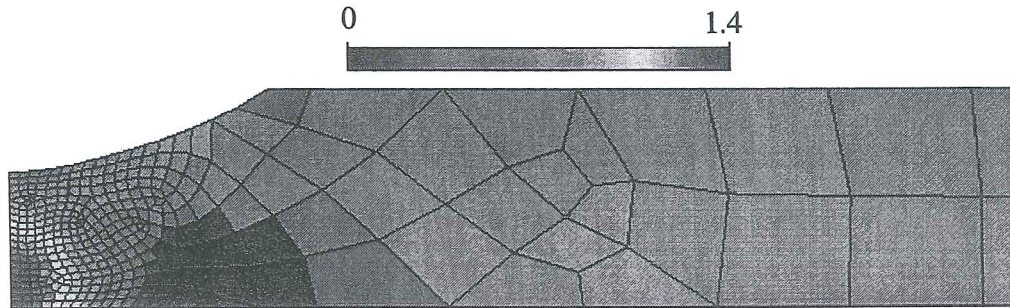
Each case is studied in following sections then a general discussion is proposed in section 6.2.11.

A. Tensile test of a notched specimen

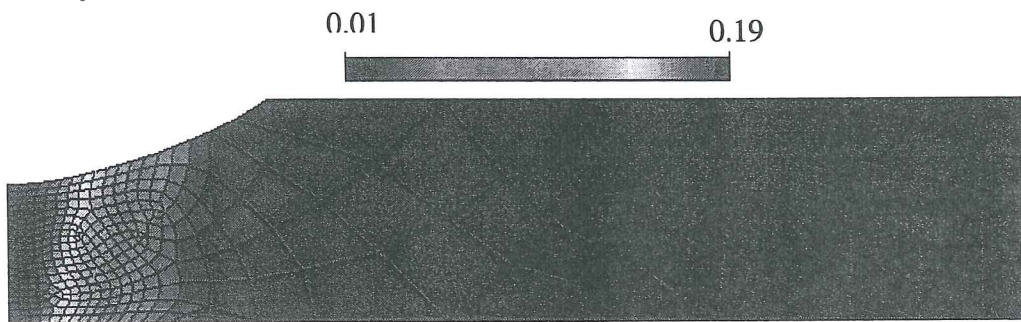
As presented on Figure 6-18, this axisymmetric tensile test has a large notch radius, which means that the damage is maximum at the center of the neck leading to a cup-cone fracture. This well-known fact (Needleman & Tvergaard, 1984) is reproduced by the performed experiments. For this test as shown by Figure 6-23, the stress field is characterized by a very high triaxiality value T of the order of 1.4. This characteristic is computed by :

$$T = \frac{\sigma_m}{\sqrt{1/2 \hat{\sigma} : \hat{\sigma}}} \quad (6-32)$$

Note that, with such triaxiality definition, the value for a uniaxial tensile experiment is $T = 0.57$. In the notch test, the high triaxiality zone covers the middle part of the section at the neck center.



a Triaxiality T .



b Equivalent strain ϵ_{eq} .



c Deviatoric damage d .

Figure 6-23 Notch simulation results (model 1) at RR' moment (partially published in Habraken *et al.* 2000).

The strain field confirms this high triaxial state: for a total displacement of 1.46 mm, an axial strain of 26 % and a radial strain of -12 % are reached in the neck center. The mesh used for the analysis of finite element results is the fourth one shown on Figure 6-20, characterized by a small b coefficient of 2.43.

Figures 6-23a, b and c respectively show the triaxiality factor, the equivalent strain and the deviatoric damage distribution of the simulation results for model 1 at the

moment identified as the “experimental rupture” (see Figure 6-21). Model 2 gives the same distribution for these 3 variables. A difference exists only on the values. For this reason, figures of results for model 2 will not be shown, neither for this example nor for the following ones, but the values will be given in Table 6-6b.

B. Tensile test of a perforated specimen

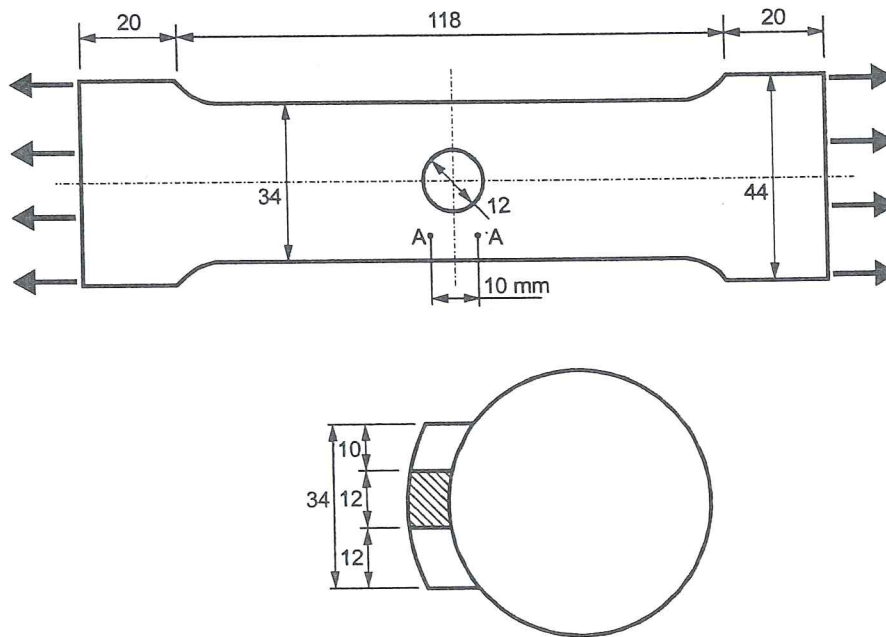


Figure 6-24 Tensile test of a perforated specimen: geometry, (from Habraken *et al.* 2000).

The sample geometry is shown on Figure 6-24. It is cut from the tube wall and is perforated in its center. The hole is not exactly in the center in such a way that one can predict on which side of the hole the fracture will begin and focus the camera on this side. A gauge length AA' is used for regulation: during the test, the extremity displacements are controlled so that a constant relative velocity of 0.01 mm/sec between A and A' is maintained. This is a three-dimensional problem. The specimen is discretized by 8-nodes 3D mixed finite elements (Figure 6-25). The ratio b between the diagonal of the smallest element and the hole radius is 9%. The ratio c between the maximal side and the minimal side of the smallest element is 2.3.

Numerically, it is difficult to keep a constant relative velocity between A and A' by loading. As the extremity displacements were not registered during the test, the measured tensile force has been imposed at the ends of the specimen. The relative displacement of A and A' until the maximum of the load have been verified. However to simulate the termination of the test, it has been necessary to change the loading strategy: after the maximum, the displacements of the ends of the specimen are imposed.

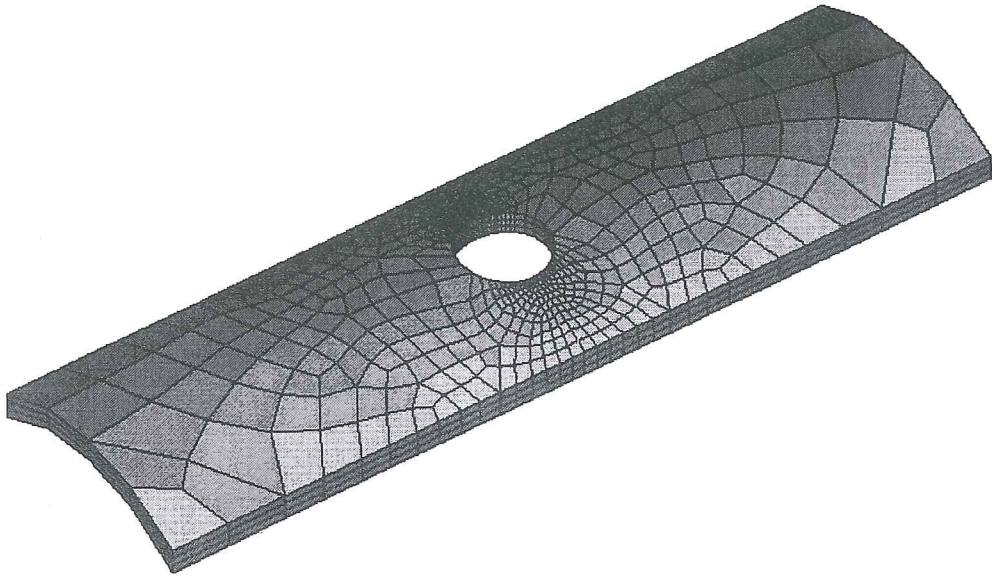


Figure 6-25 Tensile test of a perforated specimen: 3D finite element mesh (from Wang & Habraken 1996).

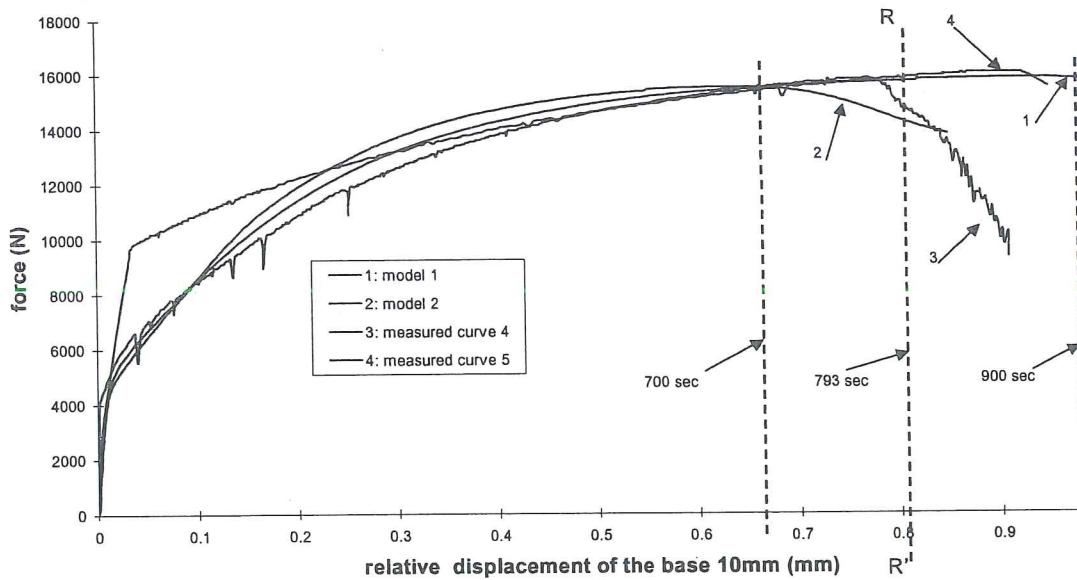


Figure 6-26 Force-relative displacement of the base AA' curves with time references (from Habraken *et al.* 2000).

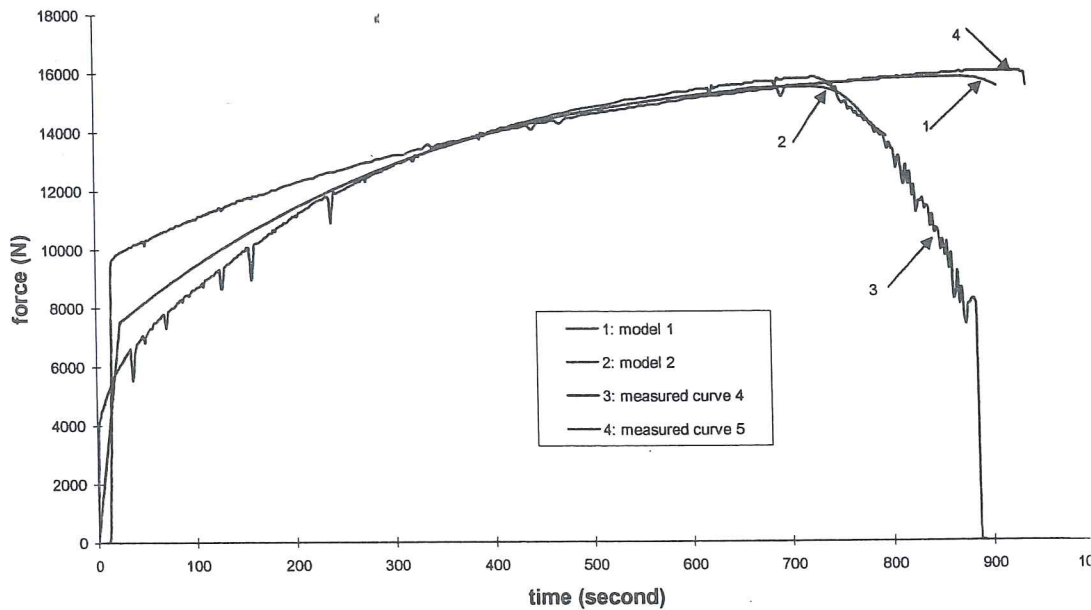


Figure 6-27 Force–time curves of the tensile test of a perforated specimen (from Habraken *et al.* 2000).

The comparison between the experimental measurements and the finite element calculations is given on Figure 6-26 for the force–displacement curves and on Figure 6-27 for the force–time curves. Generally speaking, model 2 is closer to the first test in which fracture takes place earlier, while model 1 is closer to the second test in which fracture happens later. The calculated force–time curves represent very well the drop of the experimental curve both for model 1 and model 2. But for the force–displacement curves, only model 2 follows this sudden drop trend, while model 1 shows only a little decrease of the force. This is due to a quick elongation developed at the moment of fracture.

For these simulations, at the “experimental fracture moment” (time 793 sec defined on Figure 6-26), the stress state is characterized by a relatively homogeneous triaxiality value, from 0.6 to 1.0, in the zone where deformation and damage are important. This value approaches the uniaxial tensile value “0.57”.

Figures 6-28, 6-29 and 6-30 show respectively the triaxiality factor, the equivalent strain and the deviatoric damage distributions for model 1 at RR' moment. The equivalent strain is strongly localized at the two sides of the hole root. The largest equivalent strain reaches 26.3%. The largest axial strain, the largest radial strain and the largest circumferential strain are, respectively, 38.8%, 19% (negative) and 18.9% (negative). For the deviatoric damage, d_{max} reaches 0.15, and all values of d greater than 0.14 are located within 1.2mm from the hole root.

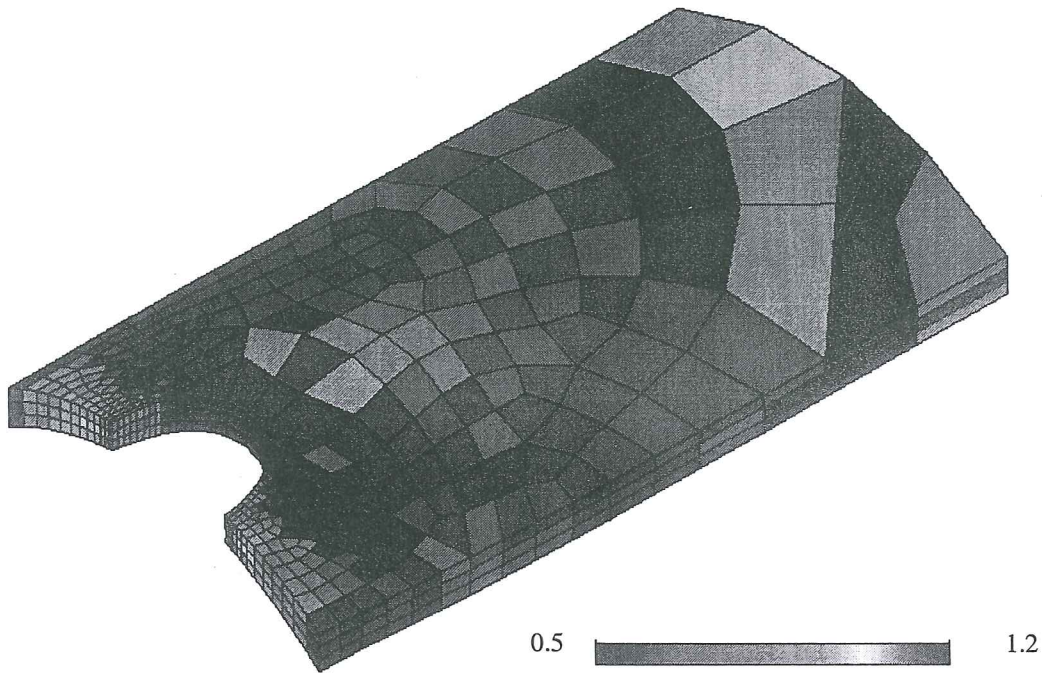


Figure 6-28 Tensile test on a perforated specimen, simulation results (model 1) at RR' moment, triaxiality T .

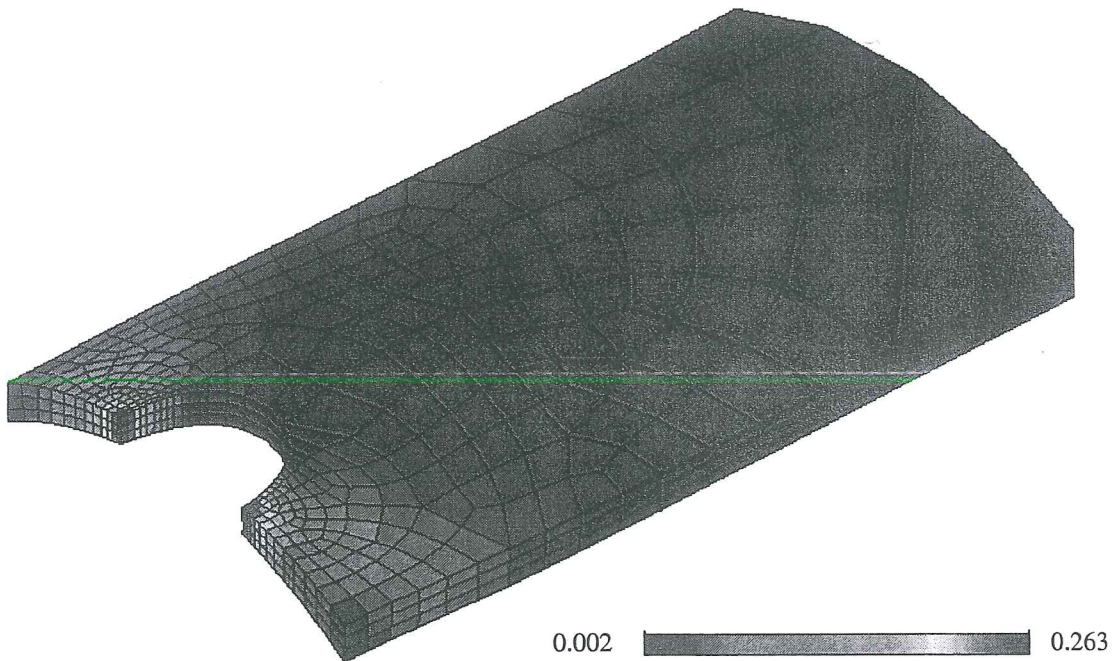


Figure 6-29 Tensile test on a perforated specimen, simulation results (model 1) at RR' moment, equivalent strain ϵ_{eq} .

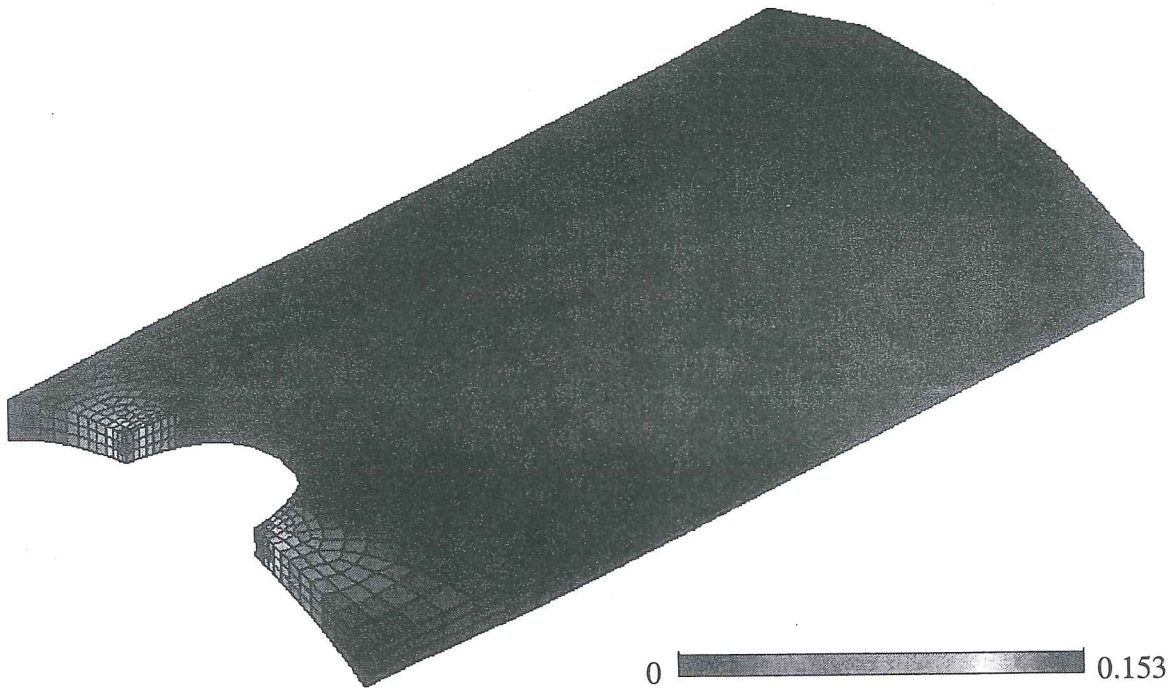


Figure 6-30 Tensile test of a perforated specimen, simulation results (model 1) at RR' moment, deviatoric damage d (from Habraken *et al.* 2000).

C. Bending test

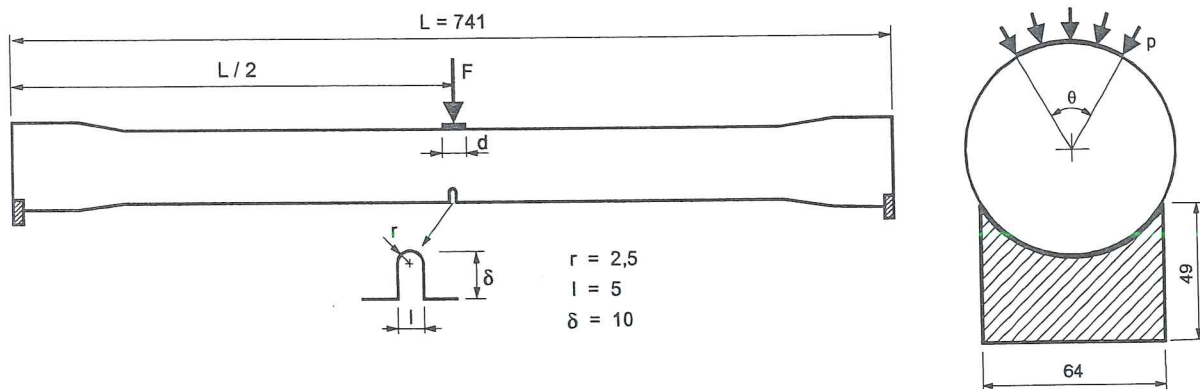


Figure 6-31 Bending test: geometry and loading (from Habraken *et al.* 2000).

The third example is a bending test. The notched whole tube is loaded and supported as a traditional three points bending, see Figure 6-31. The tube is discretized in 8-nodes 3D mixed finite elements (Fig. 6-32). The ratio b between the diagonal of the smallest element and the notch radius is about 12% and the ratio c between the maximal side and the minimal side of the smallest element is 9.5 for the first mesh with one layer of elements through the thickness (Figure 6-33a). This relatively high

c ratio leads to poorly shaped elements near the notch root. So a second mesh with two layers of elements through the tube thickness was used, its c ratio is 4.75, see Figure 6-33b.

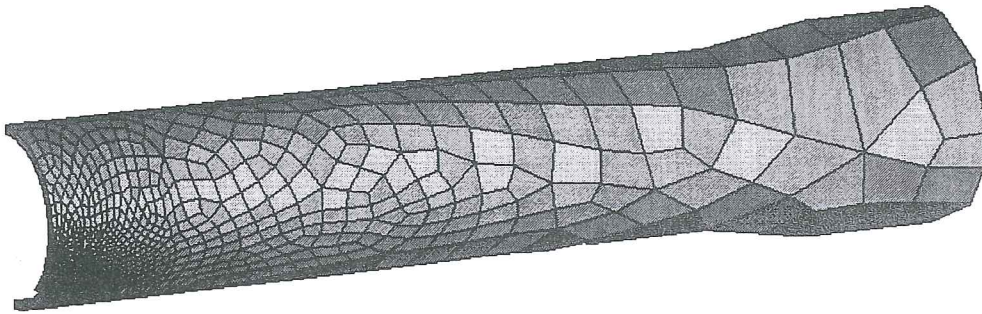


Figure 6-32 Bending test discretization, case of one element layer on the thickness, (from Habraken & Wang 1996).

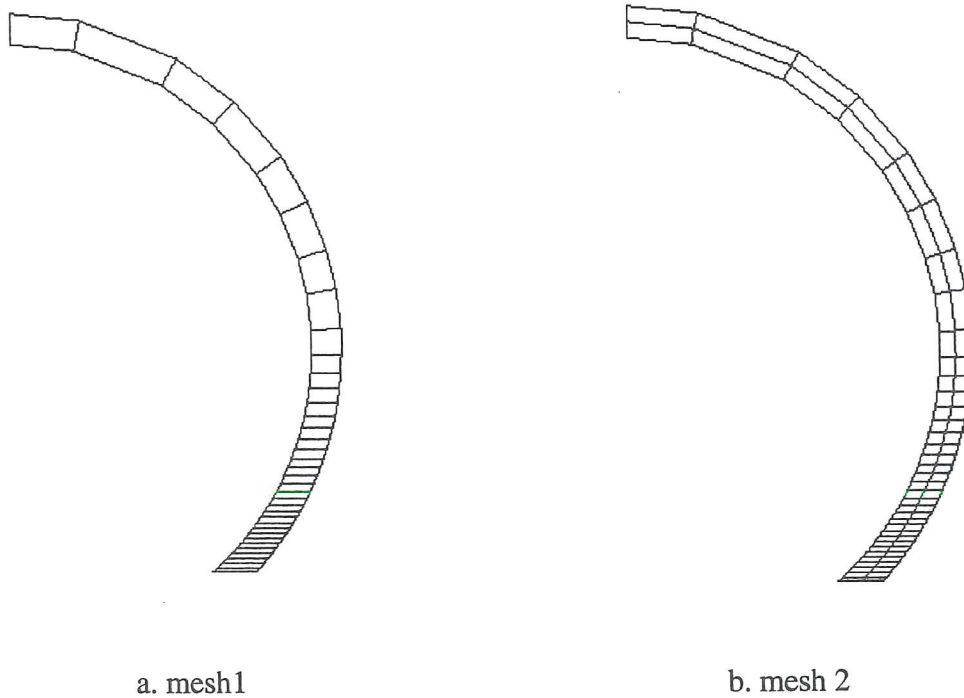


Figure 6-33 Cross section in the bending test mesh: a) one layer , b) two layers.

The measured displacement of the middle section is imposed in the simulation which takes into account the problem symmetry. The numerical result of force-displacement in comparison with the experimental one is given in Figure 6-34.

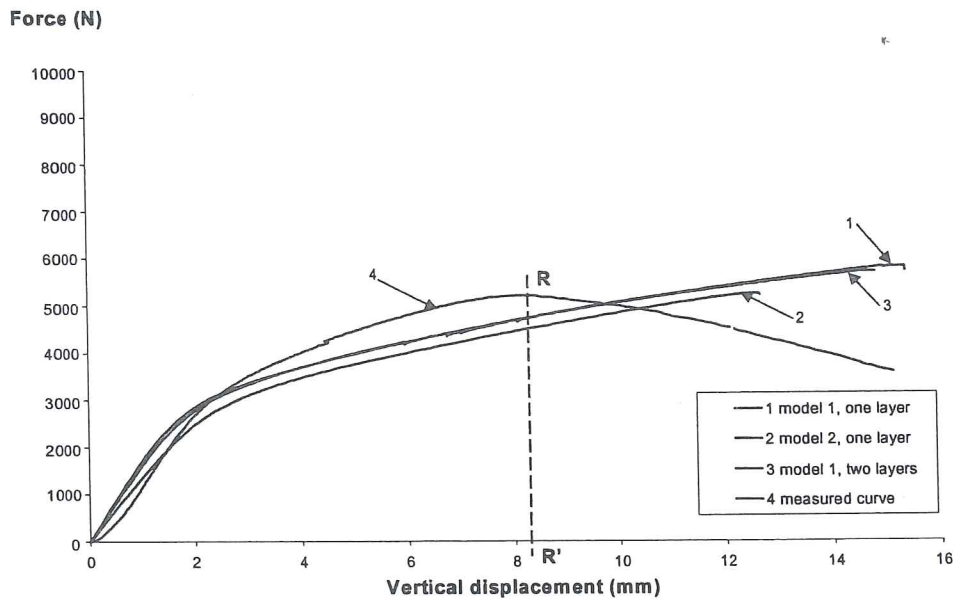


Figure 6-34 Force–displacement curves for the bending test for meshes with one and two layers of element, definition of experimental rupture, from Habraken *et al.* 2000.

The drop of the simulation curves happens much later than in the experimental breakdown. From the experimental observation, it has been checked that local fracture appears earlier than the final rupture due to the high resistance of the tube section. This fact explains why the “experimental local rupture” identified by RR’ line on Figure 6-34 seems far from real structure fracture. Figure 6-35 shows deviatoric damage computed by model 1 with mesh 2. Strain and damage are strongly localized above the notch. When the imposed displacement reaches 8.33mm (the experimental rupture, presented by RR’ in Figure 6-34), Table 6-3 presents the results for both simulations with one or two layers of elements. The shear strains are very low and not presented in the table. Clearly mesh dependence affects the simulation results. In fact in this case, the damage is highly concentrated and cannot be represented with a coarse mesh. To simulate the high damage gradient the *b* and *c* ratios should be even smaller than the smallest one used (*b*=12%, *c*=4.75%). However CPU time and storage memory prevent to go on with finer meshes. A strong damage variation between the internal layer and the external one demonstrates the necessity of low *c* ratio.

simulation	ϵ_{eqmax}	d_{max}	ϵ_x	ϵ_y	ϵ_z
mesh 1 (<i>c</i> =9.5)	16%	0.082	-8.9%	20.3%	-11.1%
mesh 2 (<i>c</i> =4.75)	29.4%	0.156	-9.6%	24.4%	-18.7%

Table 6-3 The results of bending test for mesh 1 and mesh 2 (model 1).

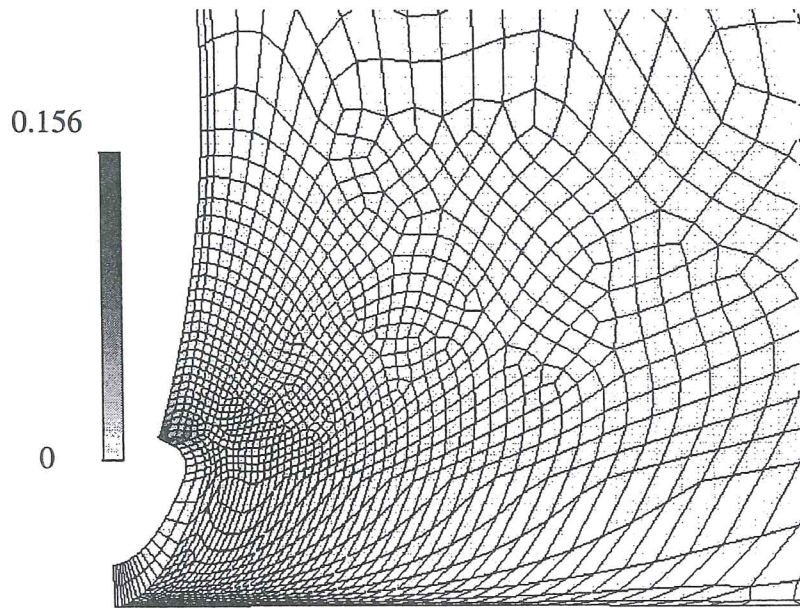


Figure 6-35 Deviatoric damage d computed by mesh 2 and model 1 (from Habraken *et al.* 1999).

D. Shear test of perforated tube

The fourth validation test is a shear test. As shown on Figure 6-36 and 6-37, the end of the tube is perforated for getting a shear-dominated loading. To simulate this test, two finite element meshes are used. The first mesh is shown in Figure 6-38a. Its b ratio is equal to 50% and its c ratio is equal to 2.5. As the b ratio is much larger than the one discussed in section 6.2.9, to get poor results with a lot of strain or damage discontinuities is not astonishing. In order to get reasonable results, a second mesh is used, shown in Figure 6-38b. It has a b ratio of 15% and a c ratio of 4.1, which seems reasonable enough to analyze the results.

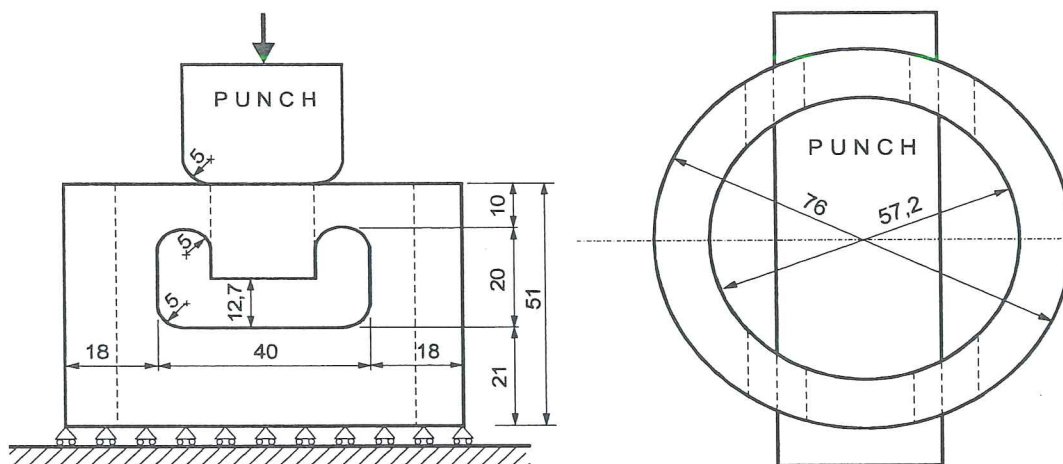


Figure 6-36 Geometry and loading of the shear test (from Habraken *et al.* 2000).

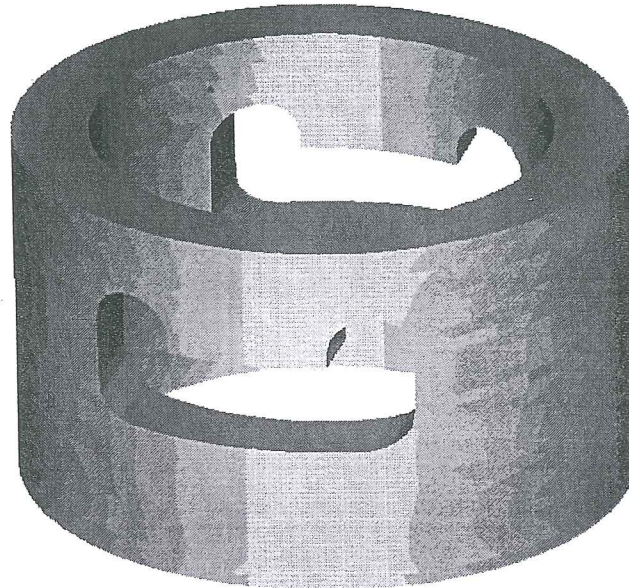
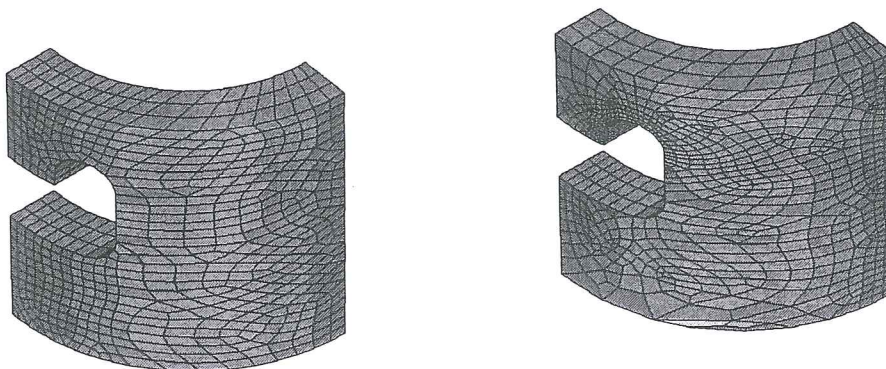


Figure 6-37 Shear test, by symmetry only 1/4 is used in computation (from Habraken & Wang 1996).



a. Shear test: mesh 1

b. Shear test: mesh 2

Figure 6-38 Finite element meshes.

Model 1		Displacement	d_{max}	$\epsilon_{eq\ max}$	$\epsilon_{eq\ outside}$	$\epsilon_{eq\ internal}$
Mesh 1 $b=50\%$	First test fracture	7.0	0.15	42.4%	14-42%	29-36%
	Second test fracture	8.3	0.22	52.4%	19-52%	36-46%
Mesh 2 $b=15\%$	First test fracture	7.0	0.18	39.6%	14-39%	21-36%
	Second test fracture	8.3	0.27	50.7%	18-50%	28-46%

Table 6-4 Results of two meshes for shear test (model 1).

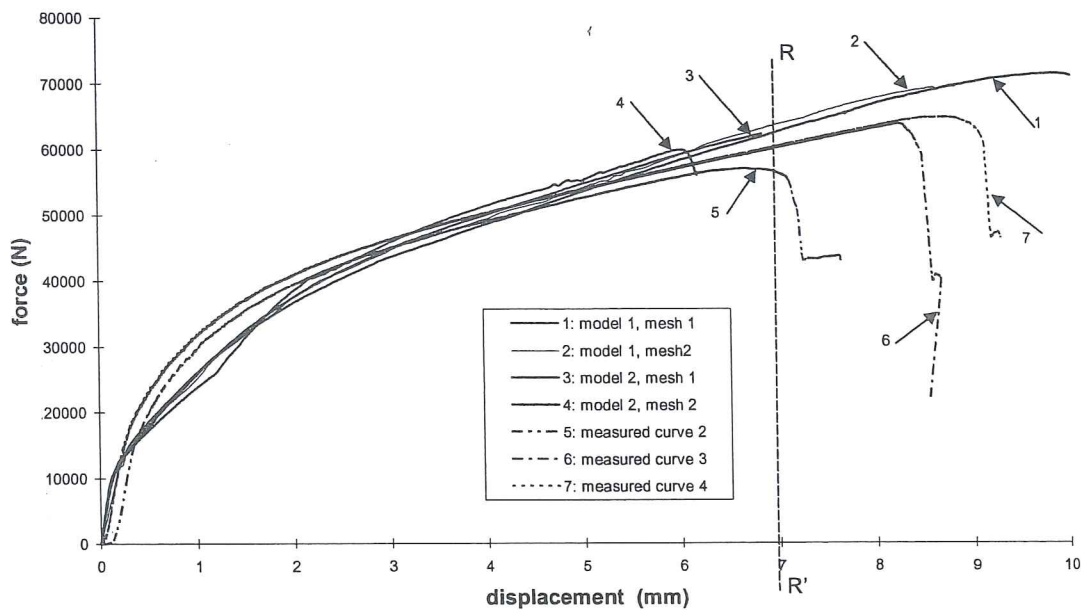
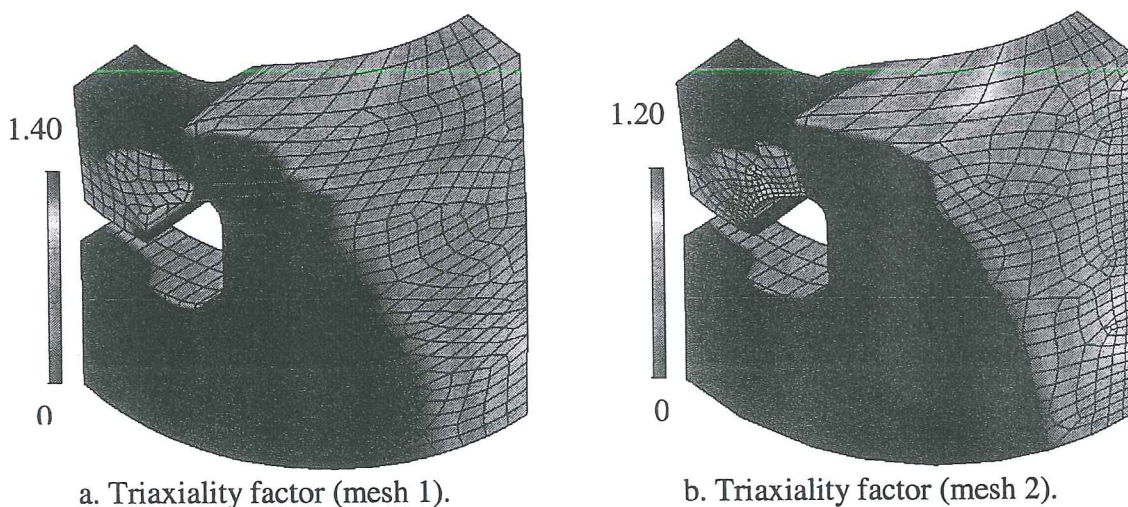


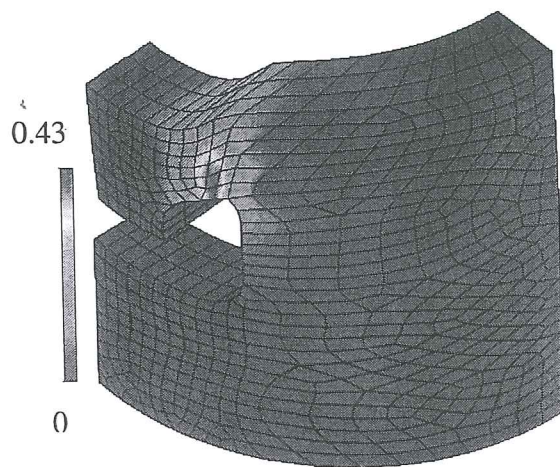
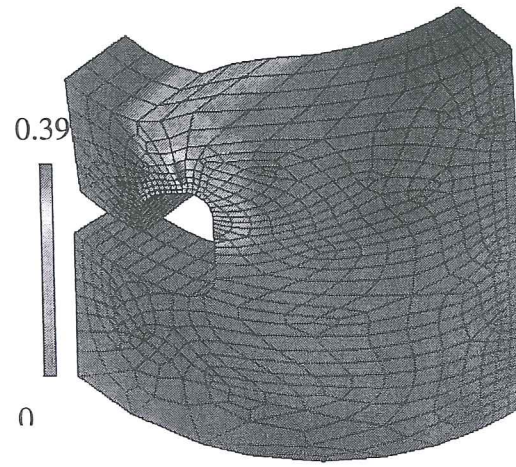
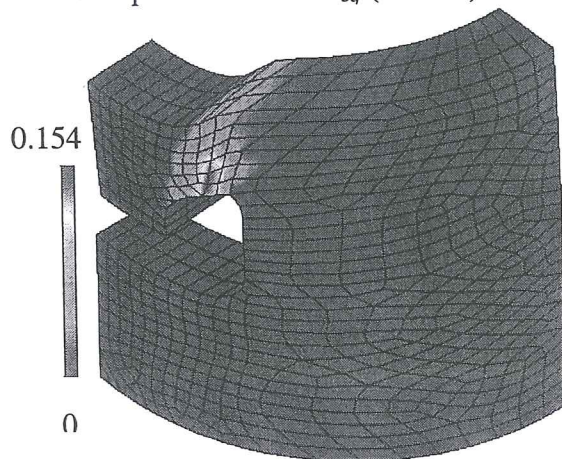
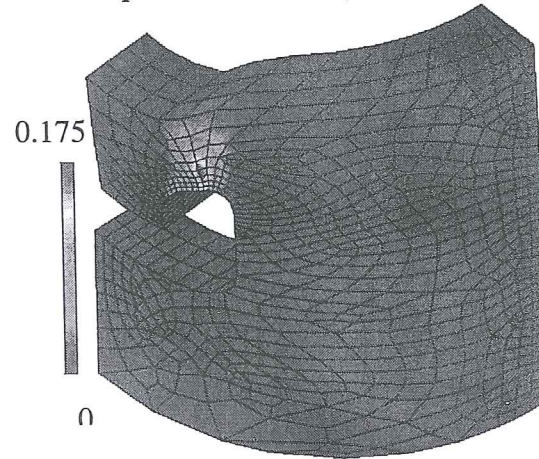
Figure 6-39 Force-displacement curves for the shear test , identification of the “experimental rupture” (from Habraken *et al.* 2000).

Figure 6-39 shows force-displacement curves of the experiments and the calculations. The drop of the simulation curves happens later than in the experiments except for the curves of model 2. Figures 40a to 40f show the triaxiality factor T , the equivalent strain ϵ_{eq} and the deviatoric damage d at the moment of “experimental rupture” (imposed displacement of 7mm defined on Figure 6-39, line RR') for the two meshes. Some simulation results of the two meshes are summarized in Table 6-4.



a. Triaxiality factor (mesh 1).

b. Triaxiality factor (mesh 2).

c. Equivalent strain ϵ_{eq} (mesh 1).d. Equivalent strain ϵ_{eq} (mesh 2).e. Deviatoric damage d (mesh 1).f. Deviatoric damage d (mesh 2).Figure 6-40 Simulation results with model 1 (part f from Habraken *et al.* 2000).

The global simulation results (force-displacement curve, Figure 6-39) are not affected by the discretization, except for the curve drop as for the notch test with large radius. Both meshes and damage models predict the maximum deviatoric damage and the maximum equivalent strain at the experimental fracture location (internal face, above the notch). No matter the chosen damage model, the finer mesh simulates more accurately the damage or strain gradient; higher maxima are reached and they are more localized. Distribution of shear stress shows a maximum above the hole; however local hydrostatic stress concentration induces a strong gradient of the triaxiality factor.

6.2.11 Discussion

Four validation tests have been simulated. The characteristics of the used meshes are summarized in Table 6-5. Then, Tables 6-6 a and b gather the strain and triaxiality levels near the crack for each simulation.


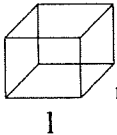
Test description	Problem description	Smallest elements $n > m > l$	$b = \text{diagonal} / R_{\text{notch}}$	$c = n/l$
Notch test	2D axisymmetry problem	m  l	2.4%	/
Hole test	3D problem	m  l	9%	2.3
Bending test mesh 1	3D problem		12%	9.5
Bending test mesh 2	3D problem		12%	4.75
Shear test mesh 1	3D problem		50%	2.5
Shear test mesh 2	3D problem		15%	5.5

Table 6-5 Validation test simulations: Finite element discretizations (from Habraken *et al.* 1999)

Test description	Characteristics	ϵ_{eqmax}	d_{max}
Rod tensile test	Uniaxial stress field, low triaxiality: 0.57	13%	0.06
Axisymmetric large notch bar tensile test, $R=7mm$	Concentrated high triaxiality in the center neck zone: 1.4	20% maximum, $\epsilon_{eq} \geq 17$ for whole central section	$d_{max}=0.154$, maximum at center, $d \geq 0.14$ covers 1/3 center section
Perforated bar tensile test, $R=6mm$	Stress and strain maxima at the hole root, but mean to low triaxiality in the whole middle section (≈ 0.8)	26% maximum, localized at the notch root	$d_{max}=0.154$, maximum localized at the notch root, $d \geq 0.14$ covers 1/6 hole section
Bending test of a grooved rod, $R=2.5mm$ (mesh 1, one-layer)	Stress and strain maxima at the groove root, but mean to high triaxiality above (0.9-1.3)	17% maximum, localized at the groove root	$d_{max}=0.085$, maximum strongly localized at the groove root
Bending test of a grooved rod, $R=2.5mm$ (mesh 2, two-layer)	Stress and strain maxima at the groove root, but mean to high triaxiality above (0.9-1.4)	29% maximum, localized at the groove root, in internal layer	$d_{max}=0.157$, maximum strongly localized at the groove root, in internal layer
Compression test of a perforated ring (shear appearance), $R=5mm$ (mesh 1)	Stress and strain concentration above the hole root, with strong triaxiality inhomogeneity (0.2-1.4), low triaxiality at shear zone (< 0.7)	42% maximum $\epsilon_{eq} \geq 22\%$ covers the whole section above the hole	$d_{max}=0.154$, maximum localized above the hole, $d \geq 0.14$ covers 1/2 section above the hole
Compression test of a perforated ring (shear appearance), $R=5mm$ (mesh 2)	Stress and strain concentration above the hole root, with strong triaxiality inhomogeneity (0.2-1.2), low triaxiality at shear zone (< 0.6)	40% maximum $\epsilon_{eq} \geq 15\%$ covers the whole section above the hole	$d_{max}=0.176$, maximum localized above the hole, $d \geq 0.14$ covers 1/2 section above the hole

Table 6-6a Validation test simulations: calculation results by model 1 at "experimental" rupture, line RR (from Habraken *et al.* 1999).

Test description	Characteristics	ϵ_{eqmax}	d_{max}
Rod tensile test	Uniaxial stress field, low triaxiality: 0.57	13%	$d_{max}=0.16$
Axisymmetric large notch bar tensile test**, $R=7\text{mm}$	Concentrated high triaxiality in the center neck zone: 1.4	20% maximum, $\epsilon_{eq} \geq 17\%$ covers the 1/2 central section	$d_{max}=0.48$, maximum at center, $d \geq 0.36$ covers 1/3 centers section, $d \geq 0.3$ covers 1/2 the section
Holed bar tensile test, $R=6\text{mm}$	Stress and strain maxima at the hole root, but mean to low triaxiality in the whole middle section (≈ 0.8)	30% maximum localized at the notch root	$d_{max}=0.5$, maximum localized at the notch root, $d \geq 0.36$ covers 1/6 the hole section, $d \geq 0.3$ covers 1/5 the section
Bending test of a grooved rod, $R=2.5\text{mm}$ (mesh 1, one-layer)	Stress and strain maxima at the groove root, but mean to high triaxiality above (0.8-1.3)	11% maximum, localized at the groove root	$d_{max}=0.171$, maximum strongly localized at the groove root
Compression test of a holed ring (shear appearance), $R=5\text{mm}$ (mesh 1)	Stress and strain concentration above the hole root, with strong triaxiality unhomogeneity (0.3-1.4), low triaxiality at shear zone (< 0.7)	44% maximum, localized above the hole, $\epsilon_{eq} \geq 20\%$ covers the whole section above the hole, $\epsilon_{eq} \geq 36\%$ covers 1/2 the section	$d_{max}=0.51$, maximum localized above the hole, $d \geq 0.36$ covers 1/3 section above the hole, $d \geq 0.3$ covers 1/2 the section
Compression test of a holed ring (shear appearance), $R=5\text{mm}$ (mesh 2**)	Stress and strain concentration above the hole root, triaxiality unhomogeneity (0.2-0.8), low triaxiality at shear zone (< 0.6)	41% maximum, localized above the hole, $\epsilon_{eq} \geq 18\%$ covers the whole section above the hole, $\epsilon_{eq} \geq 28\%$ covers 1/2 the section	$d_{max}=0.56$, maximum localized above the hole, $d \geq 0.38$ covers 1/3 section above the hole, $d \geq 0.28$ covers 1/2 the section

Table 6-6b Validation test simulations: calculation results by model 2 at "experimental" rupture, line RR' (from Habraken *et al.* 1999).

** The drop of these simulations takes place before the 1st rupture of the test. Only the last results are given for these simulations.

From preceding validation simulations, one can check the following observations:

- The maximum damage zone detected by both models have the same location, and correspond to experimental rupture initiation.
- Higher damage values and damage gradients are produced by model 2.
- The damage value affects the global results, so global force-displacement or force-time curves from damage model 2 present dropping behavior sooner than damage model 1, however before this decrease, the curves from model 1 and model 2 are very close to each other.
- For both models, the dropping behavior of global curves is not an accurate criterion to predict global rupture as there is a clear mesh dependence. According to the validation test, the damage model and the discretization chosen, simulations predict global rupture too early, too late or in time.
- Threshold value applied on deviatoric damage seems a good rupture initiation criterion for mean to high triaxiality cases. If the mesh is reasonably refined, a threshold value of $d=0.16$ for model 1 and of 0.5 for model 2 should detect the rupture at the experimental moment or a little earlier in case of large shear.
- The threshold values of deviatoric damage ($d=0.06$ model 1; $d=0.16$ model 2), which could be deduced from an uniaxial tensile test, characterized by a low triaxiality factor, are not adapted for mechanical state with a mean or high triaxiality factor. The explanation of this experimental observation must be a microscopic one. In fact the Figures 4-14 and 4-15 (section 4.4, in Chapter 4) produced by Benzerga *et al.* 1999 demonstrate that such macroscopic observation could be explained by the initial void fraction or a void distribution effect. The lower critical damage value in tension could be related to a different rupture mechanism in pure tensile test as reported by Gologanu *et al.* 1994. However, as no intensive microscopic study has been performed, this assumption has not been verified.
- From all equivalent strain maps and triaxiality maps, it can be checked that simple threshold value of such variables does not allow the prediction of rupture.

6.2.12 Conclusion about the use of damage extension of Bodner's model

An extension of the elasto-visco-plastic Bodner's model to classical damage approach has been proposed. A parameter identification procedure has been developed, however its application has been difficult because the experimental

work was not straightforward and its accuracy is limited. Tensile and compression tests lead to Young's modulus of similar but not identical values. The damage measurements result from different approaches: in tensile state, cyclic loading is performed on the whole rod, while in compression state, one experiment set considers large scale rings from the rod and the other one treats small cylinders from the rod wall.

The simulations of validation experiments prove that fine meshes adapted to the sample geometry must be used. Clearly the ratio between the element diagonal and the radius defect must stay about 10 % or less and well-shaped elements with edge ratio lower or equal to 5 are necessary. Generally, the use of finer meshes with b ratio of 2 or 3% would have given results leading to better knowledge of actual material fracture as, in this work, mesh independence of results has not been reached for all the validation cases. However CPU time prevents to go on in such a direction.

As the experiments were filmed with a classical camera, this allows to roughly detect the macrocrack appearance and its evolution. Comparisons of the simulation results and the experiments show that damage is correctly localized. The analysis of the results demonstrates that a simple deviatoric damage threshold value is not very accurate to detect rupture but can be used. Staying on a macroscopic level, this research did not try to link damage variable to ductile porosity or to use some microscopic criteria like the ones proposed by Brown & Embury 1973 or Thomason 1993. The present goal to verify if this macroscopic approach is able to handle different types of fracture is fulfilled. However, it is clear that this approach raises many questions without answer. One would like to have a curve defining accurately the damage threshold value according the triaxiality state. This would require for instance:

- systematic notch test study on a macroscopic level;
- microscopic investigation to be able to use microscopic criteria;
- to perform cell models to deduce macroscopic behavior.

A microscopic study would also be necessary to define which damage model (1 or 2) is closer to the reality; however from a macroscopic point of view both models are validated. The nucleation, growth and coalescence events are represented by a unique evolution law for model 1 and by 2 functions, assumed to model respectively nucleation and both growth and coalescence for model 2. This reduces the problem of fitting numerous parameters but prevents from describing accurately the fracture development. In consequence, the experimental final slope from load-displacement curve is not well reproduced. In this research, mesh dependence is strong in the prediction of slope variation in the force-displacement curve. Some regularization method as described in Chapter 5, using the actual material characteristic length, would be better than just using finite elements of equal or smaller size than l_c as suggested by Rousselier.

6.3. An elasto-plastic damage model

6.3.1. Model description

The initial version of this model was proposed by Zhu 1992. With the help of Sylvie Castagne, this model has been applied to the experiments described in section 6.2. The poor agreement between experiments and simulations leads to model modifications described in Castagne 1998 and Castagne *et al.* (to appear). This section 6.3. appears as a summary of Castagne *et al.* (to appear), however it takes into account all the notations and principles already introduced in Chapter 3.

As in Bodner's version of damage, two scalar damage variables are introduced in the model: d , the deviatoric one and δ , the volumic one. They represent the local material degradation as explained in section 3.2.1. Contrarily to Gurson's approach (see Chapter 2), damage is not strictly connected to void volume fraction even if this is the revealing phenomenon in ductile fracture. The damage variables d and δ are not quantitatively linked to void volume fraction.

Again the hypothesis of energy equivalence is assumed to replace the damaged material state by a fictitious undamaged material state, which is characterized by effective stresses and strains $\bar{\sigma}$ and $\bar{\varepsilon}$. These effective tensors are related to true tensors through damage variables by identical functions as in the above Bodner's damage model:

$$\underline{\hat{\sigma}} = \frac{\hat{\sigma}}{1-d} \quad \bar{\sigma}_m = \frac{\sigma_m}{1-\delta} \quad (6-33)$$

$$\underline{\hat{\varepsilon}}^e = (1-d)\underline{\hat{\varepsilon}}^e \quad \bar{\varepsilon}_m = (1-\delta)\varepsilon_m \quad (6-34)$$

where σ_m is the mean value of the stress tensor, $\hat{\sigma}$ its deviator, $\hat{\varepsilon}^e$ the elastic strain tensor deviator and ε_m the mean value of the strain tensor. Equations (6-33) and (6-34) imply the equality of the complementary elastic energy.

Following the thermodynamic formulation, to define a constitutive law, the first step is to choose ψ , the expression of the Helmholtz specific free energy (see equation 6-35). Zhu has applied the same proposal as Lemaître 1985, who assumes that energies related to elastic strains, plastic strains and damage growth are independent. A second assumption, hidden in Zhu's choice of ψ expression, is that elastic properties of the material depend only on the accumulated damage d and δ and not directly on the dislocation density reflected in the variable α and connected to plastic hardening.

$$\psi = \psi^e(\underline{\varepsilon}^e, d, \delta) + \psi^p(\alpha) + \psi^d(\beta) \quad (6-35)$$

where ψ^e is the elastic strain energy, ψ^p the free energy due to plastic hardening and ψ^d the free energy due to damage hardening. The elastic strain energy can be divided into the deviatoric strain energy $\hat{\psi}^e$ and the volumic dilatation energy ψ_m^e :

$$\psi^e(\underline{\varepsilon}^e, d, \delta) = \hat{\psi}^e(\underline{\varepsilon}^e, d) + \psi_m^e(\underline{\varepsilon}^e, \delta) \quad (6-36)$$

with:
$$\hat{\psi}^e(\underline{\varepsilon}^e, d) = G(1-d)^2 \hat{\underline{\varepsilon}}^e : \hat{\underline{\varepsilon}}^e \quad (6-37)$$

$$\psi_m^e(\underline{\varepsilon}^e, \delta) = \frac{9\chi(1-\delta)^2}{2} \varepsilon_m^2 \quad (6-38)$$

The true stress tensor is obtained as derivative of the free energy, see relation (3-21):

$$\begin{aligned} \underline{\hat{\sigma}} &= \rho \frac{\partial \psi}{\partial \hat{\underline{\varepsilon}}^e} = 2G(1-d)^2 \hat{\underline{\varepsilon}}^e \\ \sigma_m &= \rho \frac{\partial \psi}{\partial \varepsilon_m^e} = 3\chi(1-\delta)^2 \varepsilon_m^e \end{aligned} \quad (6-39a, b)$$

Using relations (6-33), (6-34) and (6-39a,b), one can check that effective stress and strain tensors respect the classical Hooke's law. As already presented by relation (3-22), the thermodynamic forces Y_d and Y_δ associated to damage variables d and δ are given by:

$$\begin{aligned} Y_d &= \rho \frac{\partial \psi}{\partial d} = -\frac{\underline{\hat{\sigma}} : \underline{\hat{\sigma}}}{2G(1-d)^3} = -\frac{2\hat{\psi}^e}{1-d} = -\frac{1}{2} \frac{d\hat{\psi}^e}{dd} \\ Y_\delta &= \rho \frac{\partial \psi}{\partial \delta} = -\frac{\sigma_m^2}{\chi(1-\delta)^3} = -\frac{2\psi_m^e}{1-\delta} = -\frac{1}{2} \frac{d\psi_m^e}{d\delta} \end{aligned} \quad (6-40a, b)$$

They are called "damage energy release rates". G is the shear modulus and χ is the bulk modulus. The thermodynamic formulation approach (relations 3-7 to 3-9) justifies the introduction of convex functions F , used as pseudo potentials, to satisfy the Clausius Duhem inequality. As Lemaître 1985 and Hayakawa & Murakami 1998 (relation 3-24), Zhu uses a potential decomposed into two independent components F_p and F_d representing plastic and damage criteria:

$$F_p = \sqrt{\frac{(\underline{\hat{\sigma}} - \underline{\hat{\gamma}}) : (\underline{\hat{\sigma}} - \underline{\hat{\gamma}})}{4G(1-d)^2}} - R_0 - R(\alpha) \quad (6-41)$$

$$F_d = -Y_d - \langle \tau \rangle Y_\delta - B_0 - B(\beta) = \frac{2\hat{\psi}^e}{1-d} + \langle \tau \rangle \frac{2\psi_m^e}{1-\delta} - B_0 - B(\beta) \quad (6-42)$$

where R is the force associated with plastic hardening variable α , $\underline{\hat{\gamma}}$ is the deviator of the tensor $\underline{\gamma}$, which defines the center of the plastic yield surface. The yield stress is determined by $R + R_0$ with R_0 the initial yield stress. B is the damage strengthening,

depending on the internal variable β linked to the micro-voids state. This damage strengthening is added to the initial threshold value B_0 . $\langle \tau \rangle$ is defined by δd in tensile state and 0 in compression state since the volumic damage parameter is not affected by compression. This means it cannot decrease in compression state, it just does not increase anymore. $\langle \tau \rangle$ is considered as a constant in the model implemented by Zhu.

Classically plastic strains are deduced by a normality law and an identical assumption is done for damage evolution. Such an hypothesis has been checked experimentally by Hayakawa & Murakami 1998 (see Figure 3-3):

$$\begin{aligned} \underline{\dot{\epsilon}}^p &= \dot{\lambda}_p \frac{\partial F_p}{\partial \underline{\sigma}} = \frac{\dot{\lambda}_p (\underline{\hat{\sigma}} - \underline{\hat{\gamma}})}{2(1-d) \sqrt{G(\underline{\hat{\sigma}} - \underline{\hat{\gamma}}) : (\underline{\hat{\sigma}} - \underline{\hat{\gamma}})}} \\ \dot{d} &= -\dot{\lambda}_d \frac{\partial F_d}{\partial Y_d} = \dot{\lambda}_d \\ \dot{\delta} &= -\dot{\lambda}_d \frac{\partial F_d}{\partial Y_\delta} = \langle \tau \rangle \dot{\lambda}_d \end{aligned} \quad (6-43a, b, c)$$

where $\dot{\lambda}_p$ and $\dot{\lambda}_d$ are plastic and damage multipliers.

The isotropic and kinematic plastic hardening rules are expressed as follows:

$$\begin{aligned} \dot{R} &= (1-m) \dot{\lambda}_p \frac{dR}{d\alpha} \\ \underline{\dot{\gamma}}' &= 4G(1-d)^2 m \underline{\dot{\epsilon}}^p \frac{dR}{d\alpha} + \underline{\Omega} \underline{\dot{\gamma}}' - \underline{\dot{\gamma}}' \underline{\Omega} \end{aligned} \quad (6-44a, b)$$

where $m \in [0,1]$ is a ratio specifying a combined isotropic-kinematic hardening rule, $\underline{\Omega}$ is the spin tensor contributing to Jaumann's derivative.

The damage hardening rule is given by :

$$\begin{aligned} \dot{\beta} &= -\dot{\lambda}_d \frac{\partial F_d}{\partial B} = \dot{\lambda}_d \\ \dot{B} &= \frac{dB}{d\beta} \dot{\beta} = \frac{dB}{d\beta} \dot{\lambda}_d \end{aligned} \quad (6-45a, b)$$

Finally, the plastic and the damage loading/unloading rules are expressed in Kuhn-Tucker's form by:

$$F_p \leq 0, \quad \dot{\lambda}_p \geq 0, \quad \dot{\lambda}_p F_p = 0$$

$$F_d \leq 0, \quad \dot{\lambda}_d \geq 0, \quad \dot{\lambda}_d F_d = 0 \quad (6-46a, b)$$

These relations imply that no evolution of the plasticity or damage variable occurs if F_p or F_d is negative, respectively. On the other hand, for plasticity or for damage evolution, $\dot{\lambda}_p > 0$ and $F_p = 0$ or $\dot{\lambda}_d > 0$ and $F_d = 0$ are respectively required. This model proposed by Zhu is fully described in his thesis 1992 and can also be found in the international publication Zhu *et al.* 1992, 1995.

6.3.2. Model identification

The identification consists in finding the model parameters with the help of experiments, theory analysis, curve fitting and simulations reduced to one finite element for homogeneous stress-strain states. Such simulations allow to verify the adequacy between the experimental and simulated stress-strain and damage-strain curves.

The principal data to be introduced in the model are the effective equivalent stress-plastic strain curve ($\bar{\sigma}_{eq} - \bar{\epsilon}_{eq}^p$) and the damage strengthening threshold versus deviatoric damage curve $B(\beta) \equiv B(d)$ for a uniaxial test. To compute these curves, the evolution of the uniaxial stress and of the two damage variables versus strain must be known. With the hypothesis of elastic energy equivalence, the deviatoric and volumic damage parameters are linked to the elastic moduli by the same relations as presented in Bodner's damage model (see relations (6-16) and (6-17)). The experimental results presented on Figure 6-9 and 6-12 are used. In fact, the approach called model 1 with reduced values is assumed as damage evolution during an uniaxial tensile test (Figure 6-10a) and an uniaxial compression test (Figure 6-12b).

The knowledge of these (d - ϵ) curves as well as the availability of the (σ - ϵ) experimental curves for quasi-static tensile and compression tests (Figure 6-13) allow to determine the useful data for the model.

The equivalent effective stress, used to compute ($\bar{\sigma}_{eq} - \bar{\epsilon}_{eq}^p$), is given for a uniaxial test by :

$$\bar{\sigma}_{eq} = \left(\frac{3}{2} \overline{\sigma'_{ij}} \overline{\sigma'_{ij}} \right)^{\frac{1}{2}} = \frac{\sigma_1}{1-d} \quad (6-47)$$

where σ_1 is the stress in the loading direction.

As explained in Castagne 1998, the equivalent effective strain can be computed by integrating the following equation:

$$\bar{\dot{\epsilon}}_{eq}^p = (1-d(\epsilon_{eq}^p)) \dot{\epsilon}_{eq}^p \quad (6-48)$$

Finally a unique curve is retained taking the average between the compression and the tensile cases (Figure 6-41).

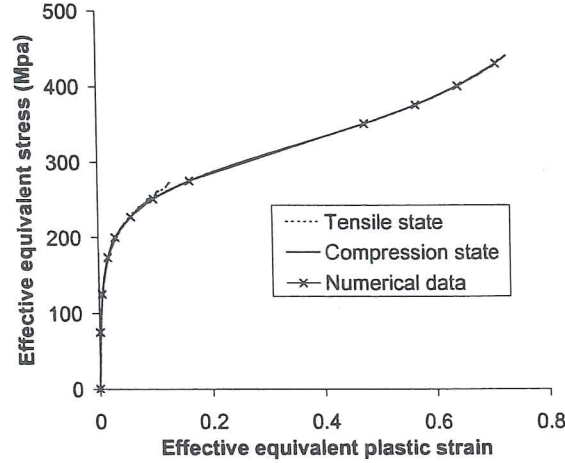


Figure 6-41 Effective equivalent stress versus effective equivalent plastic strain (from Castagne *et al.* to appear).

The second curve to be introduced to characterize the material is the $(B-d)$ curve. Using equation (6-42), the following relation for a uniaxial test is obtained:

$$B_0 + B(\beta) = \left(\frac{1}{3G_0(1-d)^3} + (p)\langle\tau\rangle \frac{1}{9\chi_0(1-\langle\tau\rangle d)^3} \right) \sigma_1^2 \quad (6-49)$$

where G_0 and χ_0 are initial elastic shear and bulk moduli, p is a weight factor explained in section 6.3.3.A. B_0 , the damage threshold is given by:

$$B_0 = \left(\frac{1}{3G_0} + (p)\langle\tau\rangle \frac{1}{9\chi_0} \right) \sigma_d^2 \quad (6-50)$$

with σ_d the initial yield stress according to the hypothesis of simultaneous plasticity and damage entrances ($\sigma_d = 75$ MPa).

Here two different curves are computed, one for the compression test and another one for the tensile test. To model fracture in tensile state, a limit value d_{coales} is introduced, it indicates voids coalescence. As soon as this value is achieved, the slope of the $(B-d)$ curve is multiplied by the factor MP to increase the damage growth (Figure 6-42) and consequently the stress reduction. Without this modification, the curve is assumed to continue with the slope computed between the last two given points. For the compression state, no modification is introduced as no coalescence appears.

The damage ratio τ , also called tensile effect, is supposed to be a constant for the model. Actually, it varies between 1.37 and 2.30 (Figure 6-43). The constant value used in the simulations is 1.57.

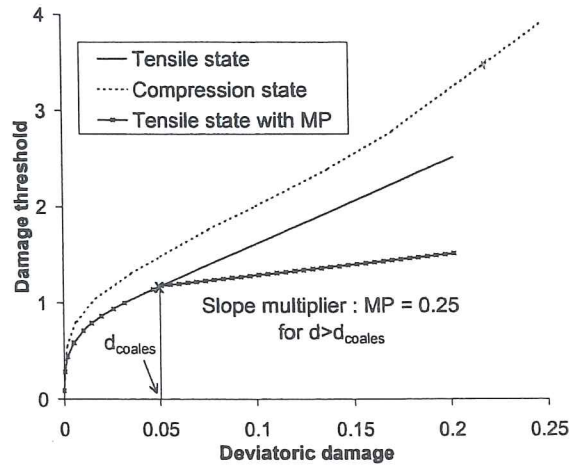


Figure 6-42 $B(d)$ curve relative to tensile and compression states (from Castagne *et al.* to appear).

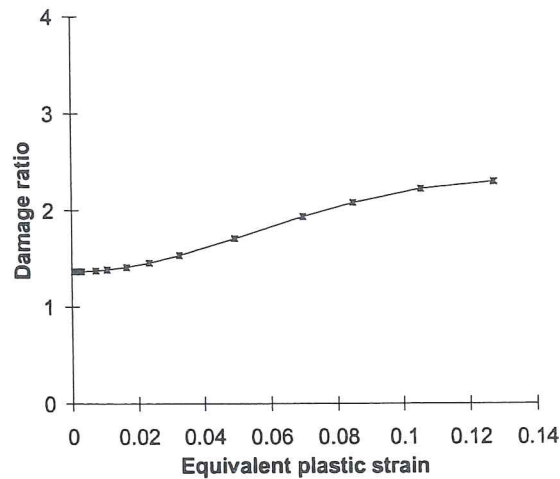


Figure 6-43 Tensile state : τ versus equivalent plastic strain (from Castagne *et al.* to appear).

Finally, the curves to be introduced in the data file are described by Figures 6-41 and 6-42. They are linearized to be written in the data file. A weight factor p will be introduced in the model (see section 6.3.3.A.). Its value has been taken into account in the calibration phase as it modifies the $(B-d)$ curve in tensile state. MP , the slope multiplier, and d_{coales} , the coalescence level, are not easily fitted as explained in section 6.3.3. They have to be adapted according the validation experiment to obtain a better visualization of the rupture event.

Table 6-7 summarizes the final set of scalar data for the analyzed aluminum. Remark that the actual initial Young's modulus of the material is not used in the simulations.

Indeed, all the equations of the model are written using the extrapolated initial Young's modulus E_0 introduced in section 6.2.7.A.

Symbol	Description	Value
E	Material Young's modulus (not used)	72505 MPa
E_0	Extrapolated initial Young's modulus	57852 MPa
ν	Poisson's ratio	0.31
τ	Damage ratio	1.57
d_{coales}	Coalescence limit in tensile state	0.05
MP	Slope multiplier of $B(d)$ in tensile state	0.25
p	Weight factor	0.1

Table 6-7 Material data (from Castagne *et al.* to appear).

After the model identification, the deviatoric damage variable and the equivalent stress represented in Figure 6-44 are in correlation with the experimental results. The rough slope modification for the damage variable in the tensile state takes account of coalescence. In fact, the performed experiments are not accurate enough to precisely analyze the damage increase during the coalescence events. The damage evolution after the point of coalescence aims to reproduce the drastic decrease of stress (see Figure 6-44b) in order to model the presence of rupture and the loss of rigidity of elements representing these material points. Theoretically, the final slope of curves describing macroscopic fracture experiments should help to define the end of damage evolution defined by the *MP* factor (Figure 6-42). However, trials to enhance this effect lead to numerical convergence problems. The compression state also shows a stress decrease near the rupture state.

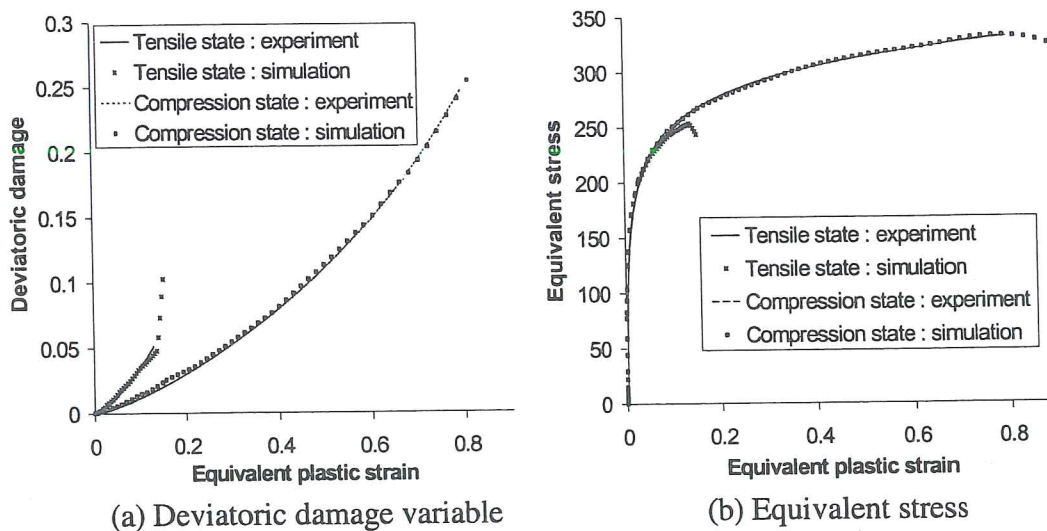


Figure 6-44 Comparison of model prediction and experiments (from Castagne *et al.* to appear).

6.3.3 Validation

This model is now applied to the same validation experiments as already presented in Bodner's damage model (section 6.2.10). The bending case is not reproduced here because the simulations have not converged due to early numerical bifurcation phenomena.

A. Tensile test of a notched specimen

First, tensile tests realized on notched cylindrical bars (Figure 6-18) are studied. The relative displacement is measured on a 25 mm basis. Three different meshes are tested in order to analyze the mesh sensitivity of the results. The experiment has been reproduced several times with very close results, which explains why only one experimental curve is presented on Figure 6-45a.

In the first simulations, very local strong damage increases with loss of convergence happened. A kinematic scalar indicator based on an idea proposed by Vilotte and used in Pierry 1997 proved the appearance of bifurcations. These localization phenomena were pointed out long before the rupture event. A viscous regularization method to improve the numerical stability as well as the suppression of the slope modification (MP) taking voids coalescence into account were introduced but this did not solve the problem.

An analysis of the damage map shows that damage increases more in the zones where triaxiality is very high. Compared to experiment, damage evolution is too important and predicts high local damage value long before rupture. This effect is enhanced when the slope of the $(B-d)$ curve is reduced. To limit the damage growth and to allow a better convergence of the simulation, a weight factor p limiting the influence of the hydrostatic energy term ψ_m has been introduced in the model. This is equivalent to a modification of the damage surface shape (6-42):

$$F_d = \frac{2\hat{\psi}^e}{1-d} + p \langle \tau \rangle \frac{2\psi_m}{1-\delta} - B_0 - B(\beta) \quad (6-51)$$

The weight factor obtained is $p = 0.1$. It gives a correct evolution of the damage and maintains the difference of behavior between the tensile and the compression state. The graphs of Figure 6-44 were in fact drawn taking into account this factor. Indeed, the calibration has to be done with the final model.

The curve representing the force on Figure 6-45a is lower than the one obtained by the experiment although the rupture by coalescence in tensile state has been removed from the model for those simulations.

Figure 6-45b presents damage state at experimental fracture and not at the beginning of necking event as on Figure 6-23. It shows that damage increases more in some elements located at the middle of the specimen, where triaxiality is very high

(Needleman and Tvergaard, 1984) and can reach 1.6 in this example. Introducing in the model a d_{coales} would introduce a more important increase of the damage variable that could induce greater convergence problems in this high triaxiality case.

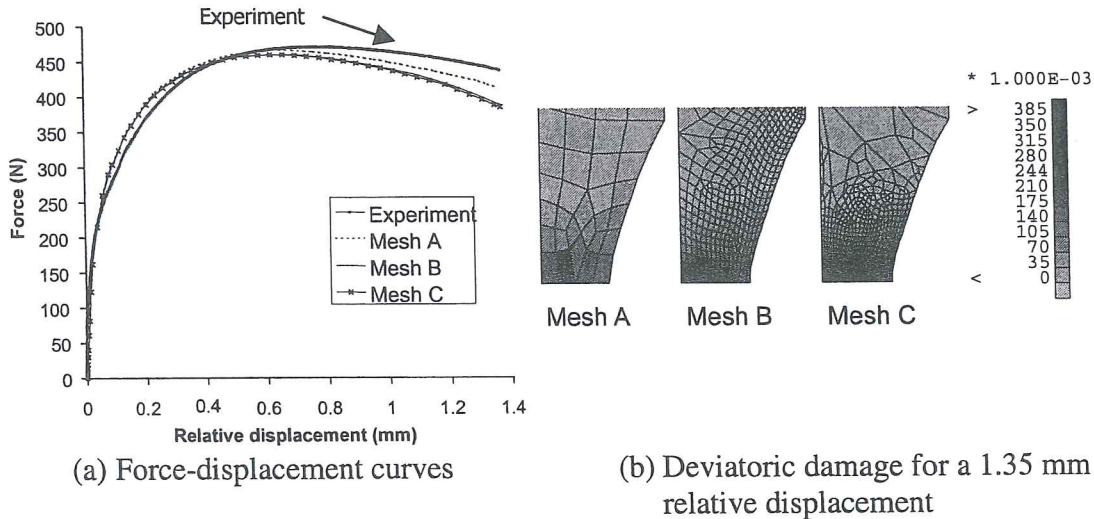


Figure 6-45 Results of model without d_{coales} and MP (from Castagne *et al.* to appear).

B. Tensile test of a perforated specimen

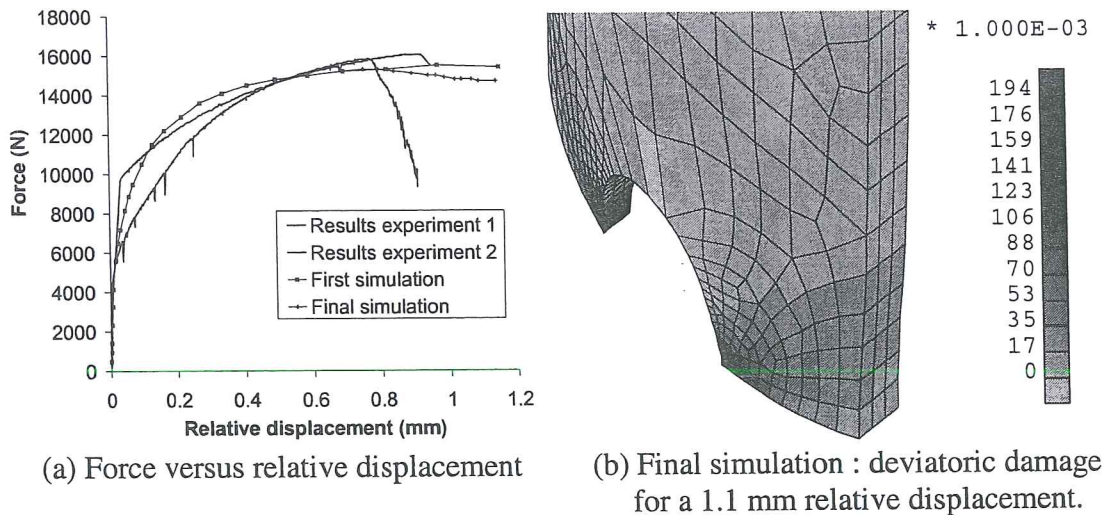
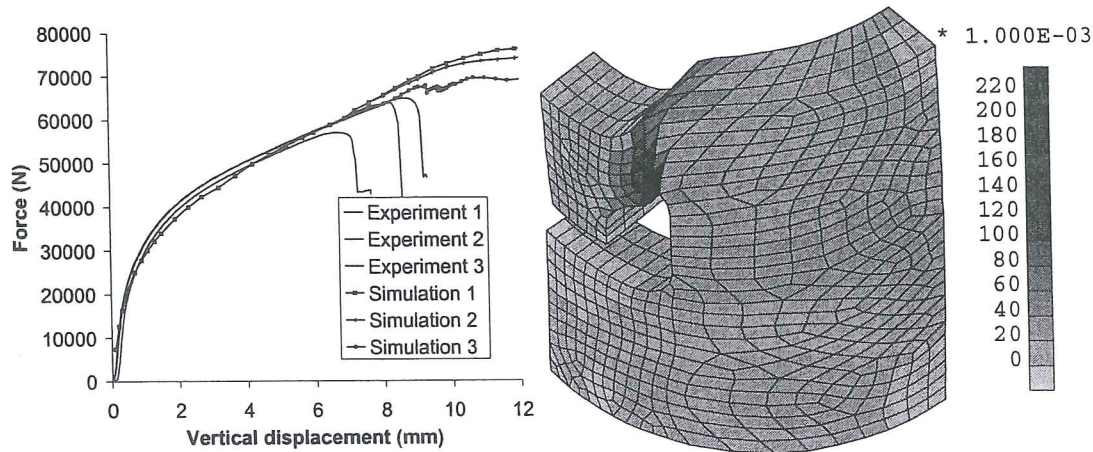


Figure 6-46 Comparison of experimental measures and simulation results (from Castagne *et al.* to appear).

The second experiment is a tensile test on a curved bar with a hole inside (Figure 6-24). The first simulation on Figure 6-46a does not include the reduction of the $(B-d)$ slope when coalescence of voids happens. Otherwise the final simulation has been realized with $d_{coales} = 0.12$ and $MP = 0.25$. One can observe that with the second simulation, a weak decrease of the force appears at the moment corresponding to the

experimental rupture. Figure 6-46b shows that the damage is maximum near the hole but its value remains low compared to the values obtained with the notch tests. Indeed, the maximum triaxiality here is 0.5 while it is 1.6 for the notch tests. The state described on Figure 6-46b happens a little later than the one described on Figure 6-30 and computed by Bodner's model.

C. Shear test of perforated tube



(a) Force versus vertical displacement of the tool

(b) Simulation 3, deviatoric damage for a 9.1 mm displacement of the tool

Figure 6-47 Comparison of experimental measures and simulation results (from Castagne *et al.* to appear).

On Figure 6-47a, the first simulation corresponds to a case with no coalescence, the second simulation has been computed with $d_{coales} = 0.15$ and $MP = 0.5$ and the last one with the same parameters as the second simulation from previous section (tensile test of a perforated specimen). For this last simulation, a reduction of the force can be observed at an imposed displacement of 7.7 mm, followed by oscillations. Figure 6-47b shows that damage begins near the hole as checked by the experiment; again this damage state is presented later than for the Bodner's damage model (Figure 6-40). Triaxiality reaches 0.6, which implies damage values lower than for the notch tests and similar to those observed during the perforated specimen test.

6.3.4 Damage criterion

The preceding experiment simulations show a strong dependence of damage level on triaxiality. The instant of rupture does not simply correspond to reaching a threshold value of the damage variable but must be linked to different factors.

The initial Zhu's model already contains the effect of triaxiality on damage through the volumic energy term. This parameter induces a too important damage growth, which leads to non convergence of the numerical simulations. The process followed here consists in limiting the triaxiality effect in order to avoid convergence problems. The coalescence damage level used in this model is a constant for the material. It is achieved earlier in a simulation where triaxiality is high since this factor increases the damage growth variable, even if the phenomenon is reduced with the modified model. The prediction of rupture, from a slope variation of the global force displacement curve, is not always possible : a too localized fracture can not be detected on this curve. On the other hand, d_{coales} the coalescence limit allows the detection of the micro-crack event and its consequences.

As it is not possible to define a unique threshold value of d_{coales} indicating a macroscopic rupture event, a rupture criterion coupling damage and triaxiality for instance should be determined. Nevertheless, the available tests are not numerous and accurate enough to establish this threshold value of the damage as a function of triaxiality. To get more data, new experiments on bars with various notch radii, corresponding to different triaxiality values, are required.

It is interesting to note that the difficulty to define a damage threshold value is not surprising, as, in reality, this limit depends on triaxiality. In fact Gurson's type model faces an identical problem. The general study of Benzerga *et al.* 1999 presents curves of the critical porosity f_{cr} depending on triaxiality T . Depending on the initial porosity value, f_{cr} is quite constant or increases with low (≈ 0.5) to mean values of T (0.8 – 1.2), then decreases for mean to high T values (>1.5), see Figure 4-14. This result from Benzerga *et al.* 1999 helps to understand why, depending on cases they study, authors like Needleman 1984, Koplik & Needleman 1988, Brocks *et al.* 1995, Brethenoux *et al.* 1997 have found various influences of T on critical porosity.

6.3.5 Conclusions

The initial Zhu's model does not apply to the studied aluminum alloy because the damage increases too rapidly in the zones where triaxiality is high. A modification of the law, that induces a less important damage increase, provides a solution.

The cracks initiation site is correctly predicted by this model, as well as their propagation directions. For shapes and loadings that correspond to a low triaxiality, if the damage zone is not too localized, the modified model allows to predict the sample rupture characterized by the drop in the force-displacement curve.

Additional experimental results are necessary for the establishment of a rupture criterion. When known, this criterion should predict the crack evolution according to damage and triaxiality.

Finally, the opportunity to use a non constant damage ratio τ should be investigated instead of introducing the reduction parameter p in equation (6-51). Indeed, Figure 6-43 shows the evolution of τ , which is not actually a constant for the studied material. Most of all, the analysis of the effect of the parameter p in the second term of equation (6-51) shows that it influences the value of τ in a nonlinear way.

6.4. Conclusions on the applied damage models

Sections 6.2. and 6.3. summarize a work performed at various times and with various co-workers, so it is not perfectly integrated. However, even if the damage figures are not related to the same time, it can be observed that the adapted Zhu's model is more sensitive to triaxiality than Bodner's damage version. This explains why it has not been possible to define a simple damage threshold limit to detect microcrack events for this model. As suspected, the numerical stability of the damage elasto-plastic approach is lower than the damage elasto-visco-plastic version and numerical bifurcations prevent an easy use of the model.

Different conclusions can be drawn from this work and the general literature review:

- Macroscopic damage approach can be applied to detect microcrack; however simple damage threshold value is of limited use. A criterium linking triaxiality and damage value is necessary. If one chooses to stay on a macroscopic level, systematic axisymmetric notch tests with various radii must be performed to define this limit curve, or to fit more elaborate fracture criteria by inverse modeling. Such a systematic approach would have allowed a better scientific work; however the available material shape and the cost of these experiments prevent this research extension.
- Global criteria on force-displacement are mesh sensitive if no additional regularization is applied. Non-local approaches with internal length seem to be necessary to stabilize this global information. Such non-local or gradient methods are required, if one wants to follow crack propagation.
- A microscopic material investigation, defining inclusion size and distribution, would greatly help FEM and macroscopic model users. It is necessary to be able to use rupture criteria as Thomason's or simply Rice's. It helps to adapt FEM size as explained by Rousselier. To perform a cell model analysis to define the macroscopic model parameters is not possible without knowledge of inclusion size or repartition. Even if inverse modeling based on macroscopic experiments allows fitting of models like Gurson's, a microscopic material study fixes physical variables values as initial porosity and helps to keep the advantage of the microscopic foundation of the model. In this research for instance, no discussion about the choice of model 1 or 2 in Bodner's damage approach has been possible without further microscopic information.

References

- Basuroychowdhury, I.N., Voyiadijis, G.Z. (1998) A multiaxial cyclic plasticity model for non-proportional loading cases, *IJP*, 14-9, 855-870.
- Benzerga, A., Besson, J., Pineau, A. (1999) Coalescence-controlled anisotropic ductile fracture. *J. Eng. Mat. Eng.* 121, 221-229.
- Bodner, S.R., Partom, Y. (1975) Constitutive equations for elastic-viscoplastic strain-hardening material, *J. of Applied Mechanics*, 42, 385-389.
- Brethenoux, G., Mazataud, P., Bourgain, E., Muzzi, M. & Giusti, J. (1997) A mesoscopic approach of ductile damage during cold forming processes, *Advanced Methods in Materials Processing Defects*, M. Predeleanu & P. Gilormini, 23-32.
- Brocks, W., Sun, D.Z., Honig, A. (1995) Verification of the transferability of micromechanical parameters by cell model calculations with visco-plastic materials, *Int. J. Plasticity*, 11-8, 971-989.
- Brown, L.M., Embury, J.D. (1973) The initiation and growth of voids at second phase particles. *Proceedings of the 3rd Int. Conf. on the Strength of Metals and Alloys, ICSMA3*, Cambridge, England, 164-169.
- Castagne, S. (1998) Application d'un modèle isotrope élastoplastique couplé à l'endommagement à un aluminium. Travail de fin d'études, Ingénieur Physicien, Université de Liège.
- Castagne, S., Habraken, A.M., Cescotto, S. (to appear) Application of a damage model to an aluminium alloy, accepted in *Intern. Journ. of Damage Mechanics*.
- Cescotto, S., Wang, X.C. & ZHU, Y.Y. (1993) Programme mobilisateur multimatériaux de la région wallonne, procédés intelligents de mise en œuvre par forgeage dynamique (forgeage rotatif), rapport final de la première phase.
- Chan, K.S., Bodner, S.R., Lindholm, U.S. (1988) Phenomenological modeling of hardening and thermal recovery in metals, *J. of Eng. Mat. & Techn.*, 110, 1-8.
- Chevalier, L. (1988) Etude des caractéristiques des matériaux tréfilés après l'opération de tréfilage, Thèse de doctorat, Université de Paris 6, ENS Cachan.
- Cordebois, J.P., Sidoroff, F. (1979) Damage induced elastic anisotropy, *F. Euromech*, 115.
- Dombrovsky, L.A. (1992) Increment constitutive equations for Miller and Bodner-Partom viscoplastic models, *Comp. & Struct.* 44, 1064-1072.
- Gattoufi, B. (1984) Effets de la prédéformation d, due au filage sur le comportement des métaux, Thèse de docteur de 3^{ème} cycle, Université de Paris.
- Gologanu, M., Leblond, J.B., J. Devaux (1994) Numerical and theoretical study of coalescence of cavities in periodically voided solids, *Computational Material Modeling, ASME, AD- 42/PVP-. 294*.
- Gurson, A.L. (1977) Continuum theory of ductile rupture by void nucleation and growth. *J. Engng. Materials Technology*, 99, 2-15.
- Habraken, A.M., Zhu, Y.Y., Charlier, R., Wang, X.C. (1995), A Damage Model for Elasto-Visco-Plastic Materials at Large Strains, *Computational Plasticity*.

- Fundamentals and Applications*, Owen, D.R.J., Onate, E., editors, Pineridge Press, Swansea UK, 1083-1094.
- Habraken, A.M., Wang X.C. (1996) Programme mobilisateur multimatériaux de la région wallonne, procédés intelligents de mise en œuvre par forgeage dynamique (forgeage rotatif), rapport final de la deuxième phase.
- Habraken, A.M., Zhang, L.H., Wauters, M. (1997) La calibration de l'Alu TAC, rapport interne MSM n° 230.
- Habraken, A.M., Zhang, L.H., Wang, X.C., Cescotto, S. (1999) A new elastic-viscoplastic damage model for annealed aluminium, Part 1: Theory, Calibration, Part 2 Validation, internal report, MSM department, University of Liège.
- Habraken, A.M., Zhang, L.H., Wang, X.C., Cescotto, S. (2000) A new elastic-viscoplastic damage model for annealed aluminium: Theory, Calibration, Validation, in *Continuous Damage and Fracture* edited by Benallal A. at Elsevier, The Data Science Library.
- Hayakawa, K., Murakami, S. (1998) Space of damage conjugate force and damage potential of elastic-plastic-damage materials, *Damage Mechanics in Engineering Materials*, Voyiadjis, G.S., Ju, J.W., Chaboche, J.L. Eds, 27-44.
- Koplik, J., Needleman, A. (1988) Void growth and coalescence in porous plastic solids. *Int. J. Solids Structures*, **24-8**, 835-853.
- Ladevèze, P. (1984) Sur une théorie de l'endommagement anisotrope, Rapport interne 34, LMT, Cachan, France.
- Leblond, J.B., Perrin, G., Devaux, J. (1995) An improved Gurson-type model for hardenable ductile metals, *Eur. J. Mech. A/Solids*, **14**, 499-527.
- Lemaître, J. (1985) Coupled elastoplasticity and damage constitutive equations, *J. Comp. Meth. in Appl. Mech. and Eng.* **51**, 31-49.
- Lemaître, J., Chaboche, J.L. (1985) *Mécanique des matériaux solides*, Dunod, Paris.
- Mudry, F. (1982) Etude de la rupture ductile et de la rupture par clinage d'aciers faiblement alliés, thèse d'état, Université Technologique de Compiègne.
- Needleman, A., Tvergaard, V. (1984) An analysis of ductile rupture in notched bars, *J. Mech. Phys. Solids*, **32**, 461-490.
- Pardoën, T. (1998) Ductile fracture of cold-drawn copper bars : experimental investigation and micromechanical modelling, Doctorat en sciences appliquées, Université de Louvain-La-Neuve.
- Perzyna, P. (1986) Internal state variable description of dynamic fracture of ductile solids, *Int. J. Solids & Struct.*, **22**, 797-818.
- Phillips, A., Tang J.L., Ricciuti, M. (1974) Some new observations on yield surfaces, *Acta Mechanica*, **20**, 23-39.
- Pierry, J. (1997), Modélisation des bandes de cisaillement et adaptation de maillages. Application à la coupe de la roche. Université de Liège, thèse de doctorat en sciences appliquées.
- Rousselier, G. (1987) Ductile fracture models and their potential in local approach of fracture, *Nuclear Engineering and Design*, **105**, 97-111.
- Szabo, L. (1985) Evaluation of elasto-viscoplastic tangent matrices without numerical inversion, *Comp. & Struct.* **21**, 1235-1236.
- Thomason, P.F. (1993) Ductile fracture by the growth and coalescence of microvoids of non uniform size and spacing, *Acta Metall. Mater*, **41-7**, 2127-2134.

- Wang, X.C., Zhu, Y.Y., Cescotto S. (1994a) Strain-rate-sensitivity in rotary tube forging problems : finite element modelling with Bodner's constitutive model, *Proc. of 3rd Belgian Nat. Congr. of Th. & Appl. Mech.*, Liège, Belgium, 314-317.
- Wang, X.C., Zhu, Y.Y., Cescotto S. (1994b) Analytical solutions and finite element modelling of rotary tube forging, *Proc. of Metal Forming Process Simulation in Industry*, Baden-Baden, Germany, 249-269.
- Wang, X.C., Habraken, A.M., Cescotto, S. (1995) Two- and three-dimensional finite element modelling of the industrial tube forging process, *Simulation of materials processing : theory, methods and applications*, SF. Shen&P.R. Dawson Eds, Balkema, Rotterdam/Brookfield, 899-905.
- Wang, X.C. (1996) Le modèle de Bodner avec endommagement pour Alu-TAC. Une nouvelle calibration et la validation. Rapport partiel 2-9 du projet "Procédés intelligents de mise en œuvre par forgeage dynamique (2^{ème} phase)". Programme Mobilisateur de la Région Wallonne, Convention 2394.
- Wang, X.C., Habraken, A.M. (1996) An elastic-visco-plastic damage model : from theory to application, *supplément au Journal de Physique*, **6**, 549-558.
- Zhu, Y.Y., Cescotto (1991) Modèles viscoplastiques unifiés pour le comportement dynamique des matériaux soumis à de grandes vitesses de déformation. Etude bibliographique. Programme mobilisateur multimatériaux de la Région Wallonne, Procédés intelligents de mise en œuvre par forgeage dynamique (forgeage rotatif), phase 1.
- Zhu, Y.Y. (1992) Contribution to the local approach of fracture in solid dynamics, Ph. D. Thesis, University of Liège, Department MSM.
- Zhu, Y.Y., Cescotto, S. and Habraken, A.M. (1992) A fully coupled elastoplastic damage modeling and fracture criteria in metalforming processes, *J. of Mater. Processing Technology* **32**, 197-204.
- Zhu, Y.Y., Cescotto, S. (1994) A unified elasto-visco plastic theory of the Bodner model and an effective integration procedure, *J. DYMAT* **1**, 63-99.
- Zhu, Y.Y., Cescotto, S. and Habraken, A.M. (1995a) Modelling of fracture initiation in metalforming processes, *Materials Processing Defects*, S.K. Gosh, M. Predeleanu Eds., 155-170, Elsevier Science B.V.

7. STUDY OF STEEL SHEETS

7.1. Introduction

This chapter presents in a unified way, compatible with the notations introduced in Chapter 3, the work performed by numerous co-workers. Its goal is to give an overview of the present state of the model as its theory, finite element implementation and experimental identifications have been built by a lot of different researchers: Zhu Yongyi, Raphaël Estevez, Jean-François Charles, Serge Munhoven, Anne-France Cambron, Michaël Wauters, with Anne-Marie Habraken acting as “memory”, stimulator and coordinator. Zhu Yongyi has developed the first theoretical model (Zhu 1992), which is described in section 7.2. The approach used to follow the local axes is due to Munhoven 1995 and is described in section 7.3. Raphaël Estevez has proposed a first approach of the identification method (Estevez & Habraken 1996). Anne-France Cambron has tried to apply this approach on a Zinc sheet (Cambron 1997). Jean-François Charles has performed and analyzed a first set of experiments on RDCS steels (IF ULC Ti steel and SPXI steel) related to the model identification (Charles & Habraken 1996). Finally, Michaël Wauters (Wauters 1997, 1998, 1999, 2000) has improved the model, the identification method (summarized in section 7.4) and the experimental device. His experimental results are presented in section 7.5. He has also made some steps towards a validation (Wauters 2000 and Wauters *et al* 2000) that are presented in sections 7.6 and 7.7. The final simulation on Nakazyma biaxial test is due to Charles *et al.* 1997.

In industry, simulations of sheet metal forming operations with FEM codes are becoming a necessity during product and process development. However, researches are still required to increase accuracy and correctly predict location and moment of failure events.

The anisotropic behavior of steel sheets is well known. For instance a circular cup drawn from a circular piece of metal sheet using axisymmetric tools often presents an undulating rim called earring. The origin of such a behavior is the crystallographic nature of the plastic metal deformation. The use of anisotropic elasto-plastic models allows the description of such phenomena. Current cases of 4 ears can be predicted by a classical Hill's model (Hill 1948), but more singular cases of 6 ears request an accurate yield locus shape based for instance, on texture measurements and polycrystal plasticity (see Part B of this thesis).

An initial accurate yield locus is not sufficient to model difficult sheet metal forming processes as complex strain paths induce size and shape modifications of the yield locus. So, the work-hardening rate requires a particular attention, if one wants to model Bauschinger's effect and the cross effect. For instance, the physics based work-hardening model proposed by Teodosiu & Hu 1995 is an interesting alternative to conventional phenomenological models, as this model complexity is still

reasonable to implement in a FEM code. Nevertheless, a macroscopic energetic approach is considered hereafter.

As recalled in Chapter 2, damage models such as Gurson's (Gurson 1977) or its recent improvement proposed by Gologanu *et al.* 1994 require precise data to describe accurately nucleation, growth and coalescence of voids. Such information is difficult to get from macroscopic tests and must rely on microscopic measurements of voids which consists in a very long investigation. The models proposed by Lemaître & Chaboche 1985 are perhaps less anchored in microscopic physics but offer the advantage of being calibrated by macroscopic tests; this is the major reason of MSM choice of such a type of models. Zhu's anisotropic elasto-plastic model is an attempt to extend such a model to anisotropic cases.

7.2. Zhu's anisotropic elasto-plastic damage model

7.2.1. Model characteristics

A short literature review of anisotropic elasto-plastic damage models based on thermodynamic approach can be found in Zhu 1992. The goals of the research conducted after Zhu's departure were the development of a calibration method for his model, a better understanding of the effect of the model assumptions and finally a validation step. In fact, Zhu's model is a modified version from previous constitutive laws proposed by Cordebois & Sidoroff 1979 or Cordebois 1983. Its main features are the following ones :

- three major anisotropies are taken into account: anisotropic elasticity, anisotropic plasticity and anisotropic damage;
- the generalized damage effect tensor \underline{M} proposed by Chow and Wang 1987 is used;
- a new damage characteristic tensor \underline{J} based on the hypothesis of damage energy equivalence is proposed;
- an effective computational integration algorithm with two steps split operators is proposed;
- as large displacements and strains happen, the definition of local axes fitted on material principal axes is necessary, the local reference system proposed by Munhoven *et al.* 1996 is used;
- Hill's yield locus is adapted to describe plastic behavior; however the plastic tensor \underline{H} is not assumed to be constant during hardening; a plastic energy equivalence rule is adopted;
- a very simple function is chosen to describe damage potential, the goal is to describe damage evolution with a limited number of material parameters.

As already presented in Chapter 3 concerning general thermodynamic approach, the concept of effective stress is used. This basic assumption is translated by means of a "damage effect tensor" $\underline{M}(\underline{D})$ applied to the stress tensor $\underline{\sigma}$, which defines the effective stress tensor $\bar{\underline{\sigma}}$:

$$\bar{\underline{\sigma}} = \underline{M}(\underline{D}) : \underline{\sigma} \quad \text{or} \quad \bar{\underline{\sigma}} = \underline{M}(\underline{D}) : \underline{\sigma} \quad (7-1)$$

where the damage effect tensor is a second-order $\underline{M}(\underline{D})$ or a fourth-order tensor $\underline{M}(\underline{D})$ tensor, depending on the damage tensor order \underline{D} . Note that four fundamental variables of continuum damage mechanics have been introduced in these assumptions, i.e. the damage tensor \underline{D} , the damage effect tensor $\underline{M}(\underline{D})$, the effective stress tensor $\bar{\underline{\sigma}}$ and effective strain tensor $\bar{\underline{\varepsilon}}$.

By simplicity, anisotropic damage is characterized by a symmetric second-order tensor \underline{D} . There is no uniquely defined mathematical formulation of $\underline{M}(\underline{D})$; Zhu's choice is the one proposed by Chow & Wang 1987, which offers the advantages of a possible reduction to a scalar variable for isotropic damage and of having a simple expression outside the stress tensor principle directions.

In the principal co-ordinate system of damage, which in the present formulation is the material principal system where Hill yield locus is expressed, the effective stress tensor is computed by:

$$[\bar{\sigma}_{11} \bar{\sigma}_{22} \bar{\sigma}_{33} \bar{\sigma}_{23} \bar{\sigma}_{31} \bar{\sigma}_{12}]^T = \underline{M} [\sigma_{11} \sigma_{22} \sigma_{33} \sigma_{23} \sigma_{31} \sigma_{12}]^T \quad (7-2)$$

with the fourth rank symmetric tensor :

$$\underline{M} = \text{diag} \left[\frac{1}{1-D_1}, \frac{1}{1-D_2}, \frac{1}{1-D_3}, \frac{1}{\sqrt{(1-D_2)(1-D_3)}}, \frac{1}{\sqrt{(1-D_3)(1-D_1)}}, \frac{1}{\sqrt{(1-D_1)(1-D_2)}} \right] \quad (7-3)$$

So no special computation is required to follow damage principal directions; damage is simply defined by 3 scalars. This simple choice is of course poorer than Fichant's 1996 model (see section 3.2.7) or Gallerneau's 1995, where damage principal directions can rotate. The approaches of Hayakawa & Murakami 1998 (see section 3.2.4) or Gelin & Danescu, 1992 also use a second rank symmetric damage tensor that takes into account rotation of damage principal directions with stress or strain evolution. However as verified by sections 7.5 and 7.6, this chosen simple damage characterization is able to model anisotropic damage effect with a limited number of experiments to define the damage parameters.

Instead of the conventional postulate of strain or stress equivalence, an hypothesis of energy equivalence is used. It states that the complementary elastic energy for a damaged material has the same form as a fictitious undamaged material except that the stress is replaced by the effective stress in the energy formulation. Mathematically, this yields:

$$\psi^e(\underline{\sigma}, \underline{D}) = \psi^e(\underline{\bar{\sigma}}, \underline{D}) \quad \text{or} \quad \frac{1}{2} \underline{\bar{\sigma}}^T : \underline{\underline{C}}^{e-1} : \underline{\bar{\sigma}} = \frac{1}{2} \underline{\sigma}^T : \underline{\underline{C}}^{e-1} : \underline{\sigma} \quad (7-4)$$

where $\underline{\underline{C}}^e$ and $\underline{\underline{C}}^{e-1}$ are the stiffness tensors for the virgin and damaged elastic material respectively. By recalling (7-1), it can be easily proved that :

$$\underline{\underline{C}}^{e-1} = \underline{\underline{M}}(\underline{D}) : \underline{\underline{C}}^{e-1} : \underline{\underline{M}}(\underline{D}) \quad (7-5)$$

and, according to the hypothesis of energy equivalence, the effective elastic strain vector is :

$$\underline{\bar{\epsilon}}^e = \underline{\underline{M}}^{-1} : \underline{\epsilon}^e \quad (7-6)$$

where :

$$\underline{\underline{M}}^{-1} = \text{diag} \left[1 - D_1, 1 - D_2, 1 - D_3, \sqrt{(1 - D_2)(1 - D_3)}, \sqrt{(1 - D_3)(1 - D_1)}, \sqrt{(1 - D_1)(1 - D_2)} \right] \quad (7-7)$$

7.2.2. General thermodynamic analysis

The internal variables used in the thermodynamic analysis are listed in Table 7-1 together with their associated thermodynamic forces. The general structure of the constitutive equations is furnished by the well-established thermodynamic theory of irreversible processes described in Chapter 3. Hereafter, isothermal condition is assumed.

State variables	Associated thermodynamic forces
Elastic strain $\underline{\epsilon}^e$	Cauchy stress $\underline{\sigma}$
Accumulated plastic strain p	Plastic hardening threshold R
Damage variable $\underline{D} = (D_1 \ D_2 \ D_3)$	Damage energy release rate $\underline{Y} = (Y_1 \ Y_2 \ Y_3)$
Overall damage β	Damage strengthening threshold B

Table 7-1 State variables and associated thermodynamic forces (from Zhu 1992).

As it has been indicated in Lemaître 1985, uncoupled plasticity and elasticity are assumed so that the elastic properties depend only on damage variables and not on the dislocation density represented by p . For practical purposes, another hypothesis is introduced: energies involved in plastic flow and damage processes, dissipated by heat or stored in the material, are independent. Consequently, in the present model,

the Helmholtz free energy takes the following form, as proposed by Valliappan *et al.* 1976 or Hayakawa & Murakami 1998:

$$\rho\psi(\underline{\varepsilon}^e, \underline{D}, p, \beta) = \psi^e(\underline{\varepsilon}^e, \underline{D}) + \psi^p(p) + \psi^d(\beta) \quad (7-8)$$

where $\psi^e(\underline{\varepsilon}^e, \underline{D})$ is the elastic strain energy, $\psi^p(p)$ the free energy due to plastic hardening and $\psi^d(\beta)$ the free energy due to damage hardening. The complementary energy is obtained from the Legendre transformation of the free energy with respect to strain, i.e.

$$\rho\Pi(\underline{\sigma}, \underline{D}, p, \beta) = \underline{\sigma} : \underline{\varepsilon}^e - \rho\psi(\underline{\varepsilon}^e, \underline{D}, p, \beta) = \psi^e(\underline{\sigma}, \underline{D}) - \psi^p(p) - \psi^d(\beta) \quad (7-9)$$

According to the energy equivalence hypothesis, the elastic strain energy $\psi^e(\underline{\varepsilon}^e, \underline{D})$ and the complementary elastic energy $\psi^e(\underline{\sigma}, \underline{D})$ can be evaluated. Following the rules of thermodynamics of irreversible processes, the associated thermodynamic forces are given by :

$$\begin{aligned} \underline{\sigma} &= \frac{\rho \partial \psi}{\partial \underline{\varepsilon}^e} = \underline{\underline{M}}^{-1} : \underline{\underline{C}}^e : \underline{\underline{M}}^{-1} \underline{\varepsilon}^e \\ R &= \rho \frac{\partial \psi}{\partial p} = \frac{\partial \psi^p(p)}{\partial p} \\ B &= \rho \frac{\partial \psi}{\partial \beta} = \frac{\partial \psi^d(\beta)}{\partial \beta} \\ \underline{Y} &= \rho \frac{\partial \psi}{\partial \underline{D}} = -\rho \frac{\partial \Pi}{\partial \underline{D}} = -\frac{\partial \psi^e(\underline{\sigma}, \underline{D})}{\partial \underline{D}} = -\underline{\sigma}^T : \underline{\underline{M}} : \underline{\underline{C}}^{e-1} : \frac{\partial \underline{\underline{M}}}{\partial \underline{D}} : \underline{\sigma} \end{aligned} \quad (7-10.a,b,c,d)$$

The negative of \underline{Y} can be considered as the elastic strain energy rate associated with a unit damage increment, as it is easy to show that :

$$-\underline{Y} = \left. \frac{1}{2} \frac{d\psi^e}{d\underline{D}} \right|_{\text{at constant } \underline{\sigma}} \quad (7-11)$$

\underline{Y} is often given the name of "damage energy release rate". For this model, the Clausius-Duhem inequality recalled in Chapter 3 is written:

$$\Phi = \underline{\sigma} : \dot{\underline{\varepsilon}}_p - R \dot{p} - \underline{Y} : \dot{\underline{D}} - B \dot{\beta} \geq 0 \quad (7-12)$$

Within the hypothesis of independence of energy dissipations between plastic flow and damage process, equation (7-12) can be separated into two parts such that :

$$\underline{\sigma} : \dot{\underline{\varepsilon}}_p - R \dot{p} \geq 0 \quad \text{and} \quad -\underline{Y} : \dot{\underline{D}} - B \dot{\beta} \geq 0 \quad (7-13a, b)$$

Equations (7-13a, b) show the existence of a plastic dissipative potential and a damage dissipative potential, i.e.:

$$F_p(\underline{\sigma}, \underline{D}, R) = 0 \quad \text{and} \quad F_d(\underline{Y}, B) = 0 \quad (7-14a, b)$$

in which the former represents the plastic yield criterion; the latter is the damage evolution criterion. In the case where the criteria $F_p = 0$ and $F_d = 0$ are satisfied, the actual values of $\underline{\sigma}$, R , Y , B will make the dissipation power of equation (7-12) a stationary value. If Lagrange multipliers $\dot{\lambda}_p$ and $\dot{\lambda}_d$ are introduced, equation (7-12) can be written:

$$\Phi = \underline{\sigma} : \underline{\dot{\epsilon}}^p - R\dot{p} - Y : \underline{\dot{D}} - B\dot{\beta} - \dot{\lambda}_p F_p - \dot{\lambda}_d F_d \quad (7-15)$$

The final evolution rules are:

$$\begin{aligned} \frac{\partial \Phi}{\partial \underline{\sigma}} = 0 &\Rightarrow \underline{\dot{\epsilon}}^p = \dot{\lambda}_p \frac{\partial F_p}{\partial \underline{\sigma}} & \frac{\partial \Phi}{\partial Y} = 0 &\Rightarrow \underline{\dot{D}} = -\dot{\lambda}_d \frac{\partial F_d}{\partial Y} \\ \frac{\partial \Phi}{\partial R} = 0 &\Rightarrow \dot{p} = \dot{\lambda}_p \frac{\partial F_p}{\partial R} & \frac{\partial \Phi}{\partial B} = 0 &\Rightarrow \dot{\beta} = -\dot{\lambda}_d \frac{\partial F_d}{\partial B} \end{aligned} \quad (7-16a, b, c, d)$$

This approach finally recovers Hayakawa & Murakami's 1998 proposals, as their experiments certify the assumption of damage potential identical to the damage surface and the corresponding normality rule for damage evolution equation.

7.2.3. Fully coupled anisotropic elasto-plastic damage model

A. Anisotropic elasticity and damage

When a material is damaged, its constitutive relation is:

$$\underline{\sigma} = \underline{\underline{C}}^e : \underline{\epsilon}^e \quad \text{or} \quad \underline{\epsilon}^e = \underline{\underline{C}}^{e-1} : \underline{\sigma} \quad (7-17)$$

The classical Hooke's elastic tensor for orthotropic materials combined with equation (7-5) yields the following expression :

$$\begin{Bmatrix} \epsilon_{11} \\ \epsilon_{22} \\ \epsilon_{33} \\ \epsilon_{23} \\ \epsilon_{31} \\ \epsilon_{21} \end{Bmatrix} = \begin{bmatrix} \frac{1}{E_1(1-D_1)^2} & \frac{-\nu_{12}}{(1-D_1)(1-D_2)E_1} & \frac{-\nu_{13}}{(1-D_1)(1-D_3)E_1} & 0 & 0 & 0 \\ \frac{-\nu_{21}}{(1-D_1)(1-D_2)E_2} & \frac{1}{E_2(1-D_2)^2} & \frac{-\nu_{23}}{(1-D_3)(1-D_2)E_2} & 0 & 0 & 0 \\ \frac{-\nu_{31}}{(1-D_1)(1-D_3)E_3} & \frac{-\nu_{32}}{(1-D_2)(1-D_3)E_3} & \frac{1}{E_3(1-D_3)^2} & 0 & 0 & 0 \\ 0 & 0 & 0 & \frac{1}{2G_{23}(1-D_2)(1-D_3)} & 0 & 0 \\ 0 & 0 & 0 & 0 & \frac{1}{2G_{32}(1-D_1)(1-D_3)} & 0 \\ 0 & 0 & 0 & 0 & 0 & \frac{1}{2G_{12}(1-D_1)(1-D_2)} \end{bmatrix} \begin{Bmatrix} \sigma_{11} \\ \sigma_{22} \\ \sigma_{33} \\ \sigma_{23} \\ \sigma_{31} \\ \sigma_{12} \end{Bmatrix} \quad (7-18)$$

In order to guarantee the positive definiteness of $\underline{\underline{C}}^e$, the following conditions should be satisfied :

$$0 < \Delta_c \leq 1 \text{ with } \Delta_c = 1 - \nu_{21}\nu_{12} - \nu_{31}\nu_{13} - \nu_{32}\nu_{23} - \nu_{12}\nu_{23}\nu_{31} - \nu_{21}\nu_{13}\nu_{32} \quad (7-19)$$

$$0 < 1 - \nu_{ij}\nu_{ji} \leq 1 \text{ (no sum on } i, j), \quad 0 \leq D_i < 1$$

$$G_{23} > 0, \quad G_{31} > 0, \quad G_{12} > 0, \quad E_1 > 0, \quad E_2 > 0, \quad E_3 > 0$$

Orthotropic symmetry assumes also the following equalities expressed in the initial state ($D_1 = D_2 = D_3 = 0$) :

$$\frac{\nu_{12}}{E_1} = \frac{\nu_{21}}{E_2}, \quad \frac{\nu_{31}}{E_3} = \frac{\nu_{13}}{E_1}, \quad \frac{\nu_{32}}{E_3} = \frac{\nu_{23}}{E_2} \quad (7-20)$$

B. Anisotropic plastic yield surface

In the damage characterization of materials undergoing large plastic strains, Hill's yield criterion in stress space is expressed in the following form :

$$F_p(\underline{\underline{\sigma}}, \underline{\underline{D}}, R) = F_p(\underline{\underline{\sigma}}, R) = \bar{\sigma}_F - \sigma_y - R(p) = 0 \quad (7-21)$$

where σ_y is the initial plastic stress.

The effective equivalent stress $\bar{\sigma}_F$ is:

$$\bar{\sigma}_F = \left\{ \frac{1}{2} \underline{\underline{\sigma}}^T : \underline{\underline{H}} : \underline{\underline{\sigma}} \right\}^{1/2} = \left\{ \frac{1}{2} \underline{\underline{\sigma}}^T : \underline{\underline{H}} : \underline{\underline{\sigma}} \right\}^{1/2} \quad (7-22)$$

The effective plastic characteristic tensor $\underline{\underline{H}}$ is given by :

$$\underline{\underline{H}} = \underline{\underline{M}}(\underline{\underline{D}}) : \underline{\underline{H}} : \underline{\underline{M}}(\underline{\underline{D}}) \quad (7-23)$$

The positive definite tensor $\underline{\underline{H}}$ for orthotropic materials is represented by a 6x6 matrix in the material principal system (Hill 1948):

$$\underline{\underline{H}} = \begin{bmatrix} G+H & -H & -G & 0 & 0 & 0 \\ -H & H+F & -F & 0 & 0 & 0 \\ -G & -F & F+G & 0 & 0 & 0 \\ 0 & 0 & 0 & N & 0 & 0 \\ 0 & 0 & 0 & 0 & L & 0 \\ 0 & 0 & 0 & 0 & 0 & M \end{bmatrix} \quad (7-24)$$

where F, G, H, L, M, N are parameters characterizing the current state of plastic anisotropy. For a strain-hardening material, the uniaxial yield stress varies with increasing plastic strain and, therefore, the anisotropic parameters should also vary, since they are functions of the current yield stress (see Valliappan *et al.* 1976). For

sheet metal forming, this can be easily verified experimentally by measuring the well-known Lankford coefficient r , ratio of transversal and thickness strain rate during a tensile test. This ratio depends on the angle between the tensile and the rolling direction, its value is directly connected to $F G H L M N$ parameters, expression of the anisotropic property of the sheet. However, the Lankford coefficient is not constant during every tensile test : it depends on plastic strain; this leads to the conclusion that \underline{H} tensor must vary. As this increases the model complexity, a lot of implementations of Hill's model neglect this fact and use a constant \underline{H} tensor.

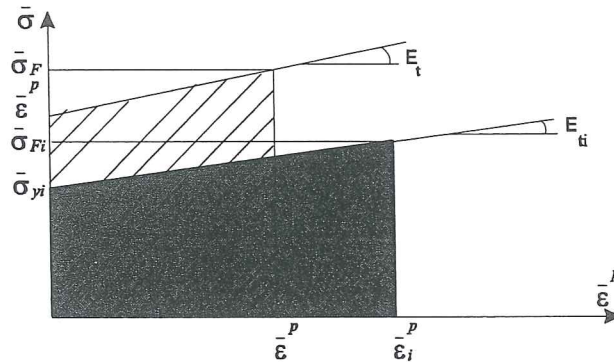


Figure 7-1 Equating plastic work for simple linear plastic behavior (from Zhu 1992).

- $\bar{\sigma}_y$ = initial effective equivalent plastic stress,
- $\bar{\sigma}_{yi}$ = initial effective plastic stress in direction i ,
- $\bar{\sigma}_F$ = effective equivalent stress corresponding to p ,
- $\bar{\sigma}_{Fi}$ = effective stress in direction i leading to the same plastic work as $\bar{\sigma}_F$,
- E_t = slope of effective equivalent stress plastic strain curve,
- E_{ti} = slope of effective stress plastic strain curve in direction i .

In Zhu's model, the evolution of the \underline{H} tensor is based on the plastic work equivalence in each direction (Figure 7-1). Practically, one direction is chosen as the reference one (generally the rolling direction) and a uniaxial tensile test in this direction gives the stress-plastic strain equivalent curve $(\bar{\sigma} \bar{\epsilon}^p)$ where for shortness no equivalence or reference indice is noted. For any material state, the knowledge of the internal variable p and equation (7-21) yield to the associate effective equivalent stress $\bar{\sigma}_F$; then, with the help of $(\bar{\sigma} \bar{\epsilon}^p)$ curve, the equivalent plastic work is estimated. Knowing $(\bar{\sigma} \bar{\epsilon}^p)_i$ curves in each direction i , the stress level $\bar{\sigma}_{Fi}$ giving the same plastic work in each direction can be found. The ratios between $\bar{\sigma}_F$ and $\bar{\sigma}_{Fi}$ are directly connected to the anisotropic parameters of the sheet (7-27).

The simple case of a linear work hardening material described by Figure 7-1 gives:

$$W^p = \frac{1}{2E_{ti}}(\bar{\sigma}_{Fi}^2 - \bar{\sigma}_{yi}^2) = \frac{1}{2E_t}(\bar{\sigma}_F^2 - \bar{\sigma}_y^2) = \text{plastic work} \quad (7-25)$$

In this simple case, equating plastic work leads to following ratios :

$$a_i = \left(\frac{\bar{\sigma}_F}{\bar{\sigma}_{Fi}} \right)^2 = \frac{\bar{\sigma}_F^2}{(E_{ii} / E_t)(\bar{\sigma}_F^2 - \bar{\sigma}_y^2) + \bar{\sigma}_{yi}^2} \quad (7-26)$$

with $i = 1, 2, 3, 23, 31, 12$.

The relations between a_i and classical anisotropic parameters are listed hereafter:

$$\begin{cases} G + H = 2a_1 & -H = -a_1 - a_2 + a_3 & N = 2a_{23} \\ H + F = 2a_2 & -G = -a_1 + a_2 - a_3 & L = 2a_{31} \\ F + G = 2a_3 & -F = a_1 - a_2 - a_3 & M = 2a_{12} \end{cases} \quad (7-27)$$

Obviously, if direction 1 is taken as reference direction, $a_1 = 1$. This hardening approach induces changes in yield shape and size.

As Zhu's proposal of linear hardening was too limited to fit with any material behavior, a multi-linear curve has been implemented by Wauters 1998. This choice of multi-linear description was preferred to a classical analytical curve description in order to retain generality. Note that the maximum number of linear segments is very high so very smooth curves can be introduced and they can accurately reproduce a large number of material behaviors.

The plastic constitutive equations incorporating material damage may be derived by taking the yield criterion (7-21) as a potential function. By assuming an associated flow rule, the plastic strain is characterized as follows :

$$\begin{cases} \dot{\epsilon}^p = \dot{\lambda}_p \frac{\partial F_p}{\partial \underline{\sigma}} = \frac{\underline{M} : \underline{H} : \underline{M} : \underline{\sigma}}{2\sigma_F} \dot{\lambda}_p \\ \text{(plastic flow rule)} \end{cases} \quad (7-28)$$

$$\begin{cases} \dot{R} = \dot{\lambda}_p \frac{dR}{dp} \\ \text{(isotropic hardening rule)} \end{cases} \quad (7-29)$$

$$\begin{cases} F_p \leq 0, \dot{\lambda}_p \geq 0, \dot{\lambda}_p F_p = 0 \\ \text{(plastic loading/unloading rule)} \end{cases} \quad (7-30)$$

C. Damage evolution law and damage surface

In a similar way to the arguments leading to plastic dissipative potential, one can assume that there exists a surface $F_d=0$, which separates the damaging domain from

the undamaging domain. A damage criterion in the form of a quadratic homogeneous function of the damage energy release rate \underline{Y} was proposed by Cordebois & Sidoroff 1979 and Cordebois 1983:

$$F_d = Y_{eq} - B_o - B(\beta) = 0 \quad (7-31)$$

where the equivalent damage energy release rate Y_{eq} is defined by :

$$Y_{eq} = \left[\frac{1}{2} \underline{Y}^T : \underline{J} : \underline{Y} \right]^{1/2} \quad (7-32)$$

in which \underline{J} is the damage characteristic tensor.

The determination of a suitable damage characteristic tensor \underline{J} , which is simple enough to be applied and still accurately describes the non-linear nature of damage growth, is perhaps the most important aspect in the present formulation of anisotropic damage evolution law. \underline{J} should be a fourth order tensor as \underline{H} . This has been adopted by Hayakawa & Murakami 1998 (see tensor \underline{L} equations (3-38) and (3-39)). However, since Zhu's model works in the principal co-ordinate system of damage, \underline{J} can be treated like a second order tensor \underline{J} . The purpose of introducing a damage characteristic tensor \underline{J} (like the introduction of plastic characteristic tensor \underline{H} in the theory of plasticity) is to take into account the anisotropic nature of damage growth. The damage characteristic tensor \underline{J} proposed by Zhu is an extension of the formulation due to Lu & Chow 1990; it is based on the damage energy equivalence assumption.

$$\underline{J} = 2 \begin{bmatrix} J_1 & \sqrt{J_1 J_2} & \sqrt{J_1 J_3} \\ \sqrt{J_1 J_2} & J_2 & \sqrt{J_2 J_3} \\ \sqrt{J_1 J_3} & \sqrt{J_2 J_3} & J_3 \end{bmatrix} \quad (7-33)$$

In the case of damage hardening materials, the equivalent damage energy release rate Y_{eq} increases with the total damage growth and, hence, the anisotropic parameters (J_1, J_2, J_3) in the above equation should also vary. Their evolution follows the same principle as \underline{H} tensor components except that plastic work is here replaced by damage work. For the case of linear damage hardening and the choice of component Y_1 as reference direction, J_2 and J_3 are computed by relation (7-34) and $J_1 = 1$.

$$J_i = \frac{Y_1^2}{(D_{ii} / D_{11})(Y_1^2 - Y_{01}^2) + Y_{0i}^2} \quad (7-34)$$

with $i = 2$ or 3 . Figure 7-2 recalls $Y_1, Y_b, Y_{ol}, Y_{oi}, D_{11}, D_{ii}$ significances.

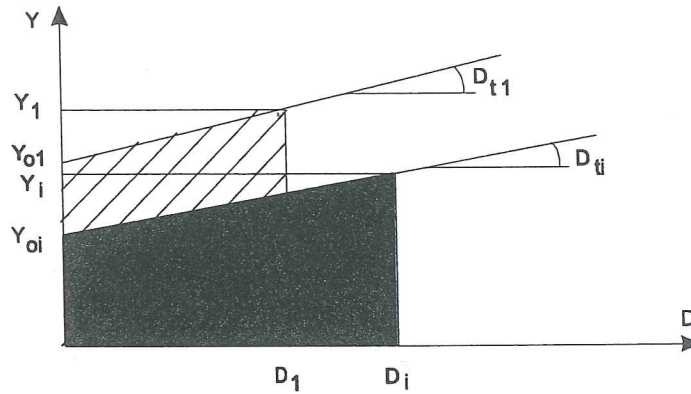


Figure 7-2 Equating damage work (from Zhu 1992).

As explained in section 7.4.4, the linear assumption of Y - D curves has strong effects on the model properties. However, for simplicity in the numerical model implementation and in the calibration method, this hypothesis is presently retained.

In the same way as the definition of plastic flow, the evolution law of anisotropic damage is characterized below:

$$\left\{ \begin{array}{l} \dot{D} = -\lambda_d \frac{\partial F_d}{\partial Y} = -\frac{J \cdot Y}{2Y_{eq}} \lambda_d = \underline{Y}^* \lambda_d \\ \text{with } \underline{Y}^* = -\frac{J \cdot Y}{2Y_{eq}} \\ \text{(damage evolution rule)} \end{array} \right. \quad (7-35)$$

$$\left\{ \begin{array}{l} \dot{\beta} = -\lambda_d \frac{\partial F_d}{\partial B} = \lambda_d \\ \dot{B} = \frac{dB}{d\beta} \dot{\beta} = \frac{dB}{d\beta} \lambda_d \\ \text{(damage hardening rule)} \end{array} \right. \quad (7-36)$$

$$\left\{ \begin{array}{l} F_d \leq 0, \lambda_d \geq 0, \lambda_d F_d = 0 \\ \text{(damage loading/unloading rule)} \end{array} \right. \quad (7-37)$$

D. Final constitutive relations

The complete set of equations is available in Zhu 1992, Zhu & Cescotto 1995; here the algebraic way to reach it and the final form of the result are presented. According to the elastic constitutive relations and effective strain tensor definition (7-6):

$$\underline{\underline{\dot{\sigma}}} = \underline{\underline{C}}^e : \underline{\underline{M}}^{-1} : \underline{\underline{\dot{\varepsilon}}}^e \quad (7-38)$$

Using the additive decomposition of strain rate into an elastic and plastic part as well as the time derivative of the inverse of the damage effect tensor and the damage rate equation (7-35), the objective rate form of equation (7-38) is obtained :

$$\underline{\underline{\dot{\sigma}}} = \underline{\underline{C}}^e : \underline{\underline{M}}^{-1} : \underline{\underline{\dot{\varepsilon}}} - \underline{\underline{C}}^* \dot{\lambda}_p - \underline{\underline{D}}^* \dot{\lambda}_d \quad (7-39)$$

where $\underline{\underline{C}}^*$ and $\underline{\underline{D}}^*$ are explicitly defined in Zhu & Cescotto 1995 and, $\overset{\nabla}{\dot{\sigma}}$ subscript means objective rate. So, the objective rate of the stress tensor is easily computed as :

$$\overset{\nabla}{\dot{\sigma}} = \underline{\underline{M}}^{-1} : \overset{\nabla}{\dot{\sigma}} - \underline{\underline{M}}^{-1} : \underline{\underline{\dot{M}}} : \underline{\underline{\sigma}} \quad (7-40)$$

Concerning damage evolution, starting from the damage energy released rate $\underline{\underline{Y}}$ in (7-10d), its time derivative is computed :

$$\underline{\underline{\dot{Y}}} = \underline{\underline{J}}^* \dot{\varepsilon} + \underline{\underline{H}}^* \dot{\lambda}_p + \underline{\underline{T}}^* \dot{\lambda}_d \quad (7-41)$$

where $\underline{\underline{J}}^*$, $\underline{\underline{H}}^*$ and $\underline{\underline{T}}^*$ are second order tensors explicitly defined in Zhu & Cescotto 1995. The final set of equations is composed by equations (7-28, 7-29, 7-30, 7-35, 7-36, 7-37, 7-40, 7-41).

7.3. Computational algorithms for anisotropic damage model

7.3.1. Local axis computation

As the anisotropic yield locus and the damage locus are defined according to material principal axes, some local reference system must follow these material axes during the large strains and rotations of the sheet. Real material axes attached to a deforming body are subjected to distortion, while local axes remain cartesian. So, there is no unique definition of a local frame, however the various possible choices differ only through a spurious rigid body rotation. In Lagamine code, the method implemented to follow material axes is due to Munhoven and details can be found in Munhoven 1995 or Munhoven *et al.* 1995. As it is an important point for the present anisotropic damage law, but also for the anisotropic laws related to texture analysis described in Part B of this thesis, this approach is summarized here. Working in hypo-elastic formulation, constitutive equations are not required for a plastic spin. This choice of hypo-elastic formulation has different advantages and remains physically sound as long as the elastic strains are small. A discussion on this choice can be found in Hoferlin 2001. In Hoferlin 1999, this scientist also links the method proposed by Munhoven to the one presented by Ponthot 1995.

Let $\underline{x} = \underline{x}(x_0, t)$ be the mapping at time t of the solid initial configuration $\gamma_0 = \gamma(t_0)$ onto the current one $\gamma(t)$ in the global frame. The Jacobian matrix also called the global *deformation gradient* is:

$$\underline{F} = \frac{\partial \underline{x}}{\partial \underline{x}_0} \quad (7-42)$$

while the global *velocity gradient* with respect to the current configuration γ is defined as:

$$\underline{L} = \frac{\partial \dot{\underline{x}}}{\partial \underline{x}} = \dot{\underline{F}} \underline{F}^{-1} \quad (7-43)$$

The symmetric and skew-symmetric parts of \underline{L} are \underline{D}^c , the *rate of deformation* tensor, and $\underline{\Omega}$, the *spin* tensor. The index c (for cinematic) aims to differentiate the \underline{D}^c tensor from the second order damage tensor \underline{D} :

$$\underline{D}^c = \frac{1}{2}(\underline{L} + \underline{L}^T) \quad \underline{\Omega} = \frac{1}{2}(\underline{L} - \underline{L}^T) \quad (7-44)$$

$$\underline{D}^c = \underline{D}^{cT} \quad \underline{\Omega} = -\underline{\Omega}^T \quad \underline{L} = \underline{D}^c + \underline{\Omega} \quad (7-45)$$

In the step by step procedure adopted in the nonlinear finite element LAGAMINE code, a strain path has to be chosen between 2 consecutive configurations, $\gamma(t_A)$ and $\gamma(t_B)$ with $t_B = t_A + \Delta t$, in order to integrate the constitutive equations. Different assumptions are possible in this context:

- velocity gradient based on *constant velocities* and with respect to the *initial* configuration $\gamma(t_A)$;
- velocity gradient based on *constant velocities* and with respect to the *final* configuration $\gamma(t_B)$;
- velocity gradient based on *constant velocities* and with respect to *substepped* configuration;
- constant velocity gradients.

This last possibility seems to be the most interesting assumption. As demonstrated by Cescotto 1992, this path is incrementally objective which explains its accuracy for steps including large rotations. First developed in two dimensions by Godinas & Cescotto 1984, this approach has been extended to three dimensions by Charles & Habraken 1998. Without computational details, this constant velocity gradient is reached by the following approach. The matrix system of differential equations is:

$$\underline{L} = \dot{\underline{F}} \underline{F}^{-1} = \underline{C}^{te} \quad (t_A < t < t_B) \quad (7-46)$$

which yields the following solution, with $(t_A < t < t_B)$:

$$\underline{F}(t) = \exp(\underline{L}(t - t_A)) \underline{F}_A \quad (7-47)$$

$$\underline{L} = \frac{1}{\Delta t} \ln(\underline{F}_{AB}) \quad (7-48)$$

Knowing that:

$$\underline{F}_A = F(t_A) = \frac{\partial \underline{x}_A}{\partial \underline{x}_0} \quad \underline{F}_B = F(t_B) = \frac{\partial \underline{x}_B}{\partial \underline{x}_0}$$

$$\underline{F}_{AB} = \underline{F}_B \underline{F}_A^{-1} \quad (7-49a, b, c)$$

The global incremental deformation gradient tensor F_{AB} is in general non-symmetric. In fact, Munhoven's idea is to require that the velocity gradient expressed in the local frame and called \underline{L}' is *symmetric*, thus spin free and *constant*. This implicitly fixes the rotations of the local frame relative to the global axes. In what follows, quantities with reference to the local frame are identified by a prime. The constraints are:

$$\underline{L}' = \underline{L}'^T = \underline{D}' \quad \underline{L}' = C^{ie} \quad t_A < t < t_B \quad (7-50)$$

As \underline{L}' is symmetric, \underline{F}'_{AB} is also symmetric and easily computed:

$$\underline{F}'_{AB} = \exp(\underline{L}'(t_B - t_A)) = \underline{F}'_{AB}{}^T \quad (7-51)$$

In general, the following relation holds between the global and local deformation gradient tensors:

$$\underline{F} = \frac{\partial \underline{x}}{\partial \underline{x}_0} = \frac{\partial \underline{x}}{\partial \underline{x}'} \frac{\partial \underline{x}'}{\partial \underline{x}_0} \frac{\partial \underline{x}_0}{\partial \underline{x}_0} = \underline{R} \underline{F}' \underline{R}_0^T \quad \text{or} \quad \underline{F}' = \underline{R}^T \underline{F} \underline{R}_0 \quad (7-52a, b)$$

If, initially, global and local axes coincide, $\underline{R}_0 = \underline{I}$ and the above equations simplify to:

$$\underline{F} = \underline{R} \underline{F}' \quad \text{and} \quad \underline{F}' = \underline{R}^T \underline{F} \quad (7-53a, b)$$

So the local incremental deformation gradient tensor \underline{F}'_{AB} is related to the global one \underline{F}_{AB} by:

$$\underline{F}'_{AB} = \underline{F}'_B \underline{F}'_A{}^{-1} = \underline{R}_B^T \underline{F}_B \underline{F}_A^{-1} \underline{R}_A = \underline{R}_B^T \underline{F}_{AB} \underline{R}_A \quad (7-54)$$

The tensor \underline{F}_{AB}^* is defined by:

$$\underline{F}_{AB}^* = \underline{F}_{AB} \underline{R}_A \quad (7-55)$$

According to equation (7-54), it appears that \underline{R}_B and \underline{F}_{AB} form the right polar decomposition of \underline{F}_{AB}^* :

$$\underline{F}_{AB}^* = \underline{R}_B \underline{F}_{AB} \quad (7-56)$$

As relation (7-55) is known from global frame definition and incremental step from t_A to t_B , relation (7-56) allows to reach \underline{R}_B defining the position of local axis at time t_B . In practice, this local frame choice implies the following procedure during the stress integration scheme:

- Rotate the initial stress tensor from global to local axis:

$$\underline{\sigma}'_A = \underline{R}_A^T \underline{\sigma}_A \underline{R}_A \quad (7-57)$$

- Compute the constant symmetric velocity gradient \underline{L}' and the final rotation \underline{R}_B :

$$\underline{L}' = \frac{1}{2\Delta t} \ln((\underline{F}_{AB} \underline{R}_A)^T (\underline{F}_{AB} \underline{R}_A)) \quad (7-58)$$

$$\underline{R}_B = (\underline{F}_{AB} \underline{R}_A) \exp(-\underline{L}' \Delta t) \quad (7-59)$$

- Integrate the local constitutive equations:

$$\begin{Bmatrix} \underline{\sigma}'_B \\ q_B \end{Bmatrix} = \begin{Bmatrix} \underline{\sigma}'_A \\ q_A \end{Bmatrix} + \int_{t_A}^{t_B} \begin{Bmatrix} \underline{f}'_{\sigma} \\ f'_q \end{Bmatrix} dt \quad (7-60)$$

where q are state variables (scalars, vectors or tensors), \underline{f}'_{σ} and f'_q represent the set of constitutive relations defining $\underline{\dot{\sigma}}$ and \dot{q} .

- Rotate back the final stress tensor from local to global axes:

$$\underline{\sigma}_B = \underline{R}_B \underline{\sigma}'_B \underline{R}_B^T \quad (7-61)$$

This approach has the advantage of requiring only limited additional storage for the rotation \underline{R} . In moderate tension and shear tests with superimposed large rigid-body rotations, this procedure performs quite well. Even if no explicit link with objective Jaumann stress rate is done, $\underline{\dot{\Omega}} = 0$ involves $\underline{\dot{\Omega}} = \dot{\underline{R}} \underline{R}^T$. In consequence, under very large shear deformations, meaningless oscillating results are found (Szabo & Balla 1989).

7.3.2 Time integration procedure

The return mapping algorithms with the operator splitting methodology proposed by Simo and Ortiz (1985) is applied to Zhu's anisotropic elasto-plastic damage model. This results in a fully coupled integration scheme with a two-step procedure: elastic predictor and coupled plastic-damage corrector. There exists two coupled surfaces, and, for every iteration, the plastic surface and damage surface are both corrected. The details can be found in Zhu & Cescotto 1995.

7.4. Identification method of Zhu's anisotropic elastoplastic damage model

7.4.1. Description of the tests

As implemented in LAGAMINE code, Zhu's model requires the following data:

- the effective stress strain curves $\bar{\sigma} - \bar{\epsilon}$ in each tensile and shear direction (11, 22, 33, 23, 31, 12) in the material reference frame;
- the initial damage energy release rate Y_i versus associated damage component D_i in each material principal direction 1, 2, 3;
- the initial material reference frame position (1,2,3) expressed according to global axis (x,y,z) used for finite element mesh as shown on Figure 7-3.

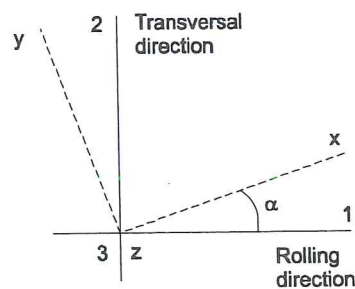


Figure 7-3 Definition of reference axes.

Considering a sheet, where rolling direction is assumed to be direction 1, three different sets of experiments are performed:

- Normalized tensile tests in directions 11, 22 and in direction x with $\alpha = 45^\circ$ (Figure 7-3 defines α angle) with accurate measurements in the field of small strains allow to reach anisotropic *elastic* parameters.

- Normalized tensile tests in direction x with different values of angle α and accurate measurements in the field of large strains provide anisotropic *plastic* parameters. As explained by section 7.4.4 the *damage* parameters can also be deduced from these experiments and no specific damage tests are necessary if a linear assumption of $(Y_i D_i)$ curves is chosen.
- In order to validate damage evolution law, non classical tensile tests with numerous loading and unloading cycles in directions 11 and 22 have been performed with sample shape adapted to localize necking position.

The sample geometry used for elastic and plastic measurements is deduced from European standard and adapted to the limits of available extensometers. It is presented on Figure 7-4.

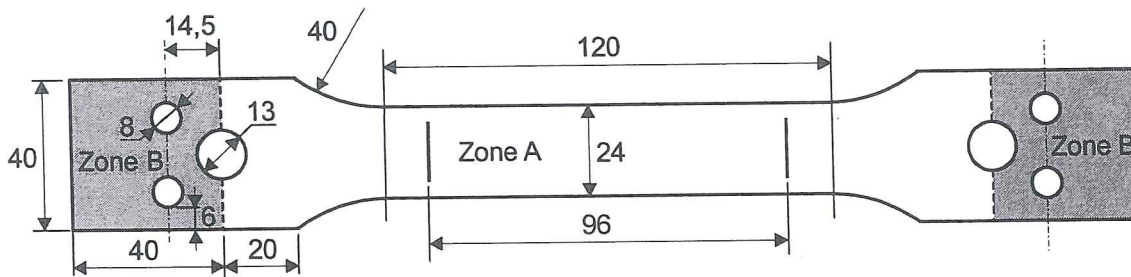


Figure 7-4 Description of the sample shape used for elastic and plastic measurements (from Wauters 2000).

Tensile tests out of orthotropic material directions require some care as principal stress and strain directions do not coincide (Boehler *et al.* 1987). If classical clamped boundary conditions are imposed, the sample tends to take a “S shape”, characteristic of anisotropic solids and the homogeneity of stress and strain fields is lost. Figure 7-5 describes the grip developed by Ph. D. student Wauters to prevent this “S-shape”. At one extremity, it allows the grip to rotate relative to the press by means of a kneecap piece, so the load will be well centered and applied longitudinally. At the other extremity, the grip presents 2 ball bearings, which allow a cylinder bar connected to the sample to rotate freely. Figure 7-6 defines *A* and *B* zones used in the FEM simulations and identifies points *D*, *C*, *E* required to define boundary conditions.

Figures 7-7a and b show the transversal displacement distribution produced by simulations of tensile test for an angle α of 45° . The material is the SPXI steel sheet studied in section 7.5. The boundary conditions are either imposed axial displacement of point *C* (see Figure 7-6), to model the grip described by Figure 7-5, or fixed transversal displacement and imposed axial displacement of segment *DCE*, to model a clamped test. Zone *A* is simulated by an elasto-plastic law and zone *B* by an elastic material to take into account the effect of the plate screwed tight on the sample. One can observe the “S shape” on Figure 7-7a computed with a clamped model, while the kneecap model leads to a more symmetric distribution (see Figure 7-7b).

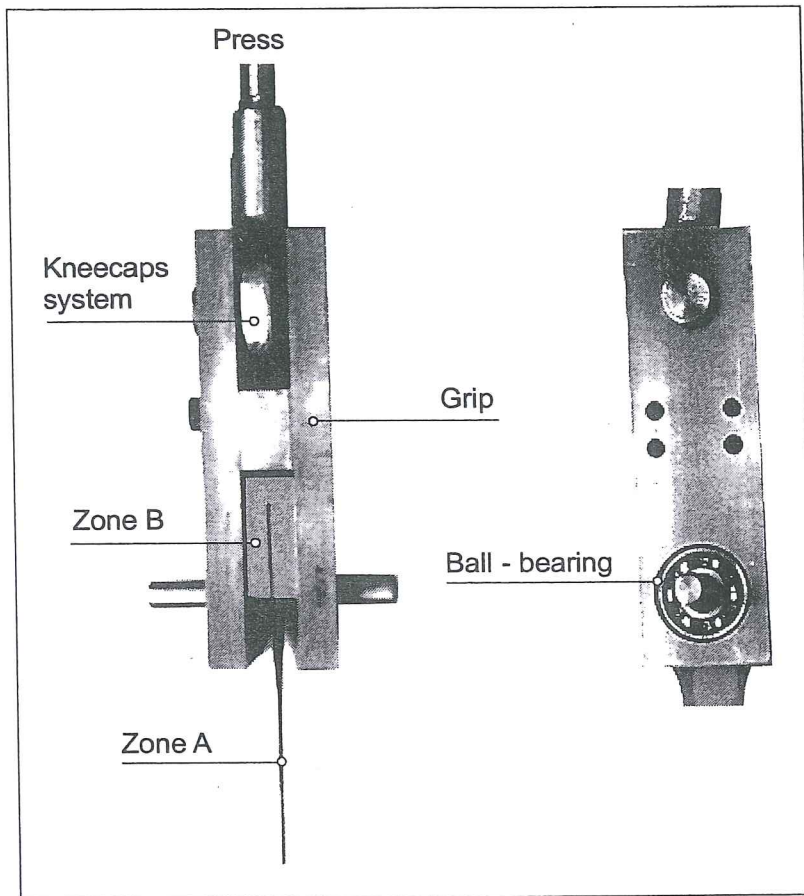


Figure 7-5 Description of the grip adapted to perform tensile tests out of material axes, (from Wauters 2000).

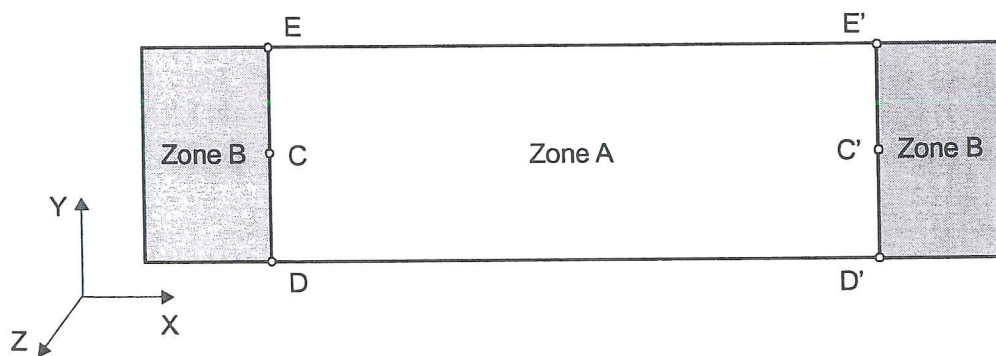
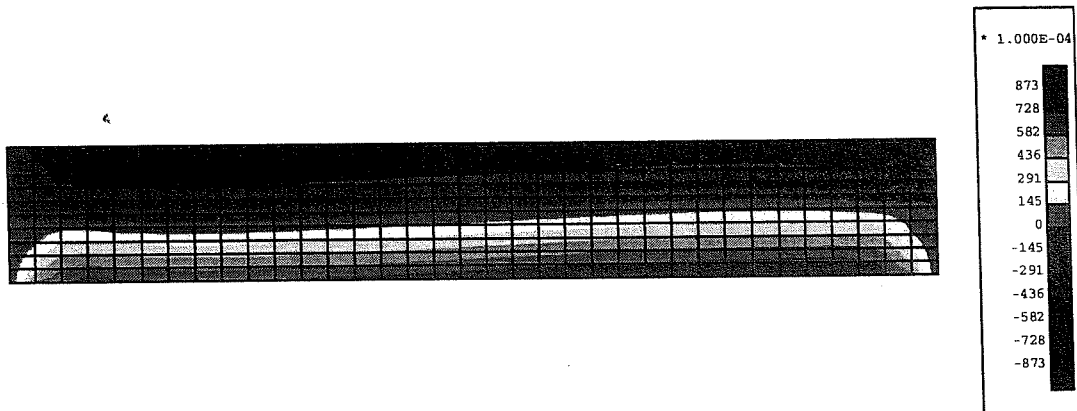
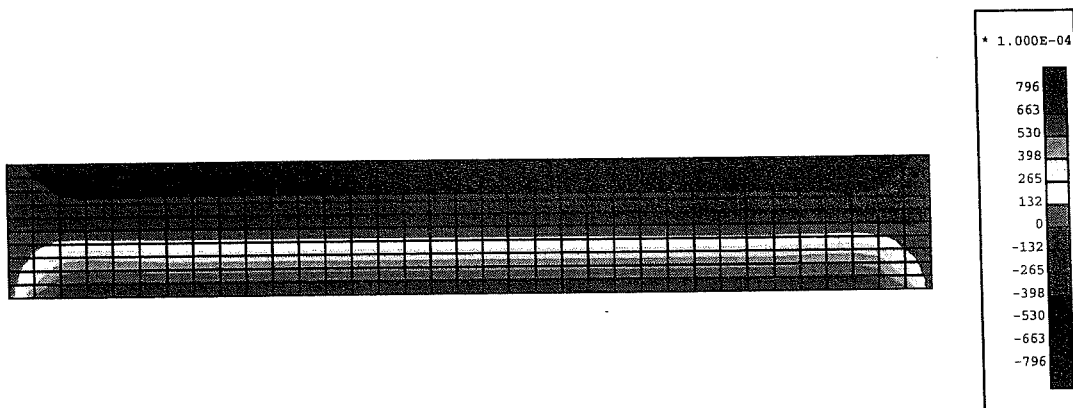


Figure 7-6. FEM model of the sample (from Wauters 2000).



a) clamped model,



b) kneecap grip model

Figure 7-7 Simulations of tensile test with $\alpha=45^\circ$, transversal displacement distribution for an imposed axial displacement of 2mm,SPXI steel sheet (from Wauters 2000).

To determine the elastic parameters, the measurement device is a bi-directional MTS extensometer leading to longitudinal and lateral displacement measurements. The reference bases are respectively 25 and 24 mm. The thickness variation is measured by a thickness extensometer (Sadner).

For plastic parameters, the large strains domain prevents the use of the above bi-directional extensometer. The longitudinal extensometer of the press, with a reference basis of 50 mm, is used as well as a transversal extensometer, with a 24 mm reference basis. The same thickness extensometer as for elastic parameters is applied. The results are more accurate since the displacements are larger.

For the damage tests, cyclic loading-unloading tests are performed in order to measure the evolution of elastic moduli. Two sample geometries were deduced using an optimization shape process based on FEM simulations (Wauters 1999). A reduced section leads to localize the damage event, where measurements are performed. Computed with the damage-elasto-plastic model, the FEM simulations verify the homogeneity of stress, strain, and damage fields, which depends on the sample

geometry. As large strains are targeted, the same extensometer could not accurately cover all the tests. So sample 1 (Figure 7-8) is fitted for strain from 0 to 20 % with an extensometer of reference basis of 25 mm. Sample 2 (Figure 7-9) covers the near rupture zone; small extensometers with reference bases of 10 mm are used until 20% strain, then strain gages are pasted on the sample and used until rupture. These samples will also provide the material required for texture measurements after 5, 10, 20 and 30% of deformation

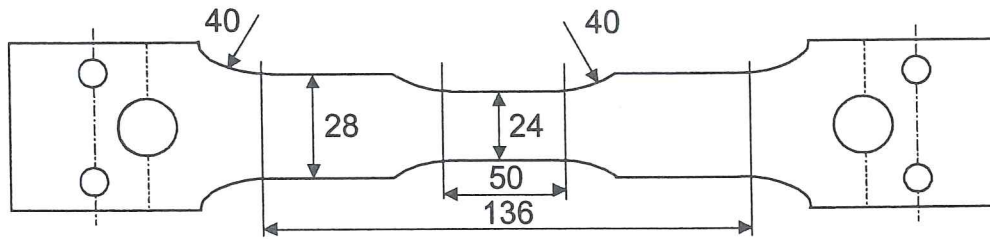


Figure 7-8 Sample geometry used for damage measures for strains less than 20% (from Wauters 2000).

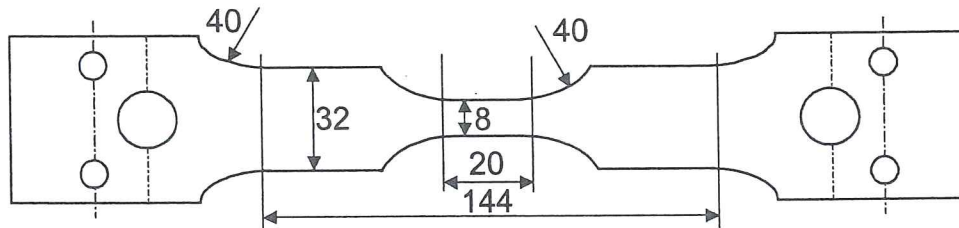


Figure 7-9 Sample geometry used for damage measure for strains greater than 20% (from Wauters 2000).

All the tensile tests have been performed on a 60 T Schenk press piloted by displacement and, for statistical reasons, repeated 5 times. The detailed procedure to deduce model parameters from these tests is described hereafter.

7.4.2. Identification of the initial anisotropic elastic properties

Tensile tests in direction x with $\alpha = 0, 45$ and 90° are performed with accurate measurements of longitudinal ϵ_x , transversal ϵ_y and thickness ϵ_z strains. Figure 7-3 defines local axes during tensile experiment (x,y,z) and material reference frame $(1, 2, 3)$. Recalling classical rotation equations, local stress and strain components $(\sigma_x, \sigma_y, \sigma_{xy}, \epsilon_x, \epsilon_y, \epsilon_{xy})$ are directly related to stress and strain components in material axes $(\sigma_{11}, \sigma_{22}, \sigma_{12}, \epsilon_{11}, \epsilon_{22}, \epsilon_{23})$.

$$\begin{Bmatrix} \xi_{11} \\ \xi_{22} \\ \xi_{12} \end{Bmatrix} = \begin{bmatrix} \cos^2 \alpha & \sin^2 \alpha & -2 \cos \alpha \sin \alpha \\ \sin^2 \alpha & \cos^2 \alpha & 2 \cos \alpha \sin \alpha \\ \cos \alpha \sin \alpha & -\cos \alpha \sin \alpha & \cos^2 \alpha - \sin^2 \alpha \end{bmatrix} \begin{Bmatrix} \xi_X \\ \xi_Y \\ \xi_{XY} \end{Bmatrix} \quad (7-62)$$

where ξ can be replaced by σ or ε .

Equation (7-18), written in material reference axes, describes the stress-strain relation in the elastic field. When damage has not yet occurred ($D_1, D_2, D_3 = 0$), one finds:

-for tensile test $\alpha = 0^\circ$:

$$E_1 = \frac{\sigma_x}{\varepsilon_x} \quad \nu_{12} = \frac{-E_1 \varepsilon_{yy}}{\sigma_x} \quad \nu_{13} = \frac{-E_1 \varepsilon_{zz}}{\sigma_x} \quad (7-63)$$

-for tensile test $\alpha = 90^\circ$:

$$E_2 = \frac{\sigma_x}{\varepsilon_{xx}} \quad \nu_{21} = \frac{-E_2 \varepsilon_{yy}}{\sigma_x} \quad \nu_{23} = \frac{-E_2 \varepsilon_{zz}}{\sigma_x} \quad (7-64)$$

-for tensile test $\alpha = 45^\circ$:

$$\begin{aligned} \varepsilon_{11} &= \frac{\sigma_{11}}{E_1} - \nu_{12} \frac{\sigma_{22}}{E_1} = \frac{\varepsilon_{xx} + \varepsilon_{yy}}{2} \\ \varepsilon_{22} &= \frac{\sigma_{22}}{E_2} - \nu_{21} \frac{\sigma_{11}}{E_2} = \frac{\varepsilon_{xx} + \varepsilon_{yy}}{2} \\ \varepsilon_{12} &= \frac{\sigma_{12}}{2G_{12}} = \frac{\varepsilon_{xx}}{2} - \frac{\varepsilon_{yy}}{2} \\ \sigma_{11} &= \sigma_{22} = \sigma_{12} = \frac{\sigma_{xx}}{2} \end{aligned} \quad (7-65)$$

which yields to:

$$\frac{1}{G_{12}} = \frac{4\varepsilon_{xx}}{\sigma_x} - \frac{1-\nu_{12}}{E_1} - \frac{1-\nu_{21}}{E_2} \quad (7-66)$$

With such an identification procedure E_3 , G_{23} and G_{31} are still missing and the following assumptions have been done:

$$\begin{aligned} G_{12} &= G_{31} = G_{23} \\ E_3 &= \frac{E_1 + E_2}{2} \end{aligned} \quad (7-67)$$

In the present research, a collaboration with professor van Houtte from Katholieke Universiteit Leuven provides elastic parameters deduced from texture measurements and physical crystal metallurgy for the two studied steel sheets. These values (see Table 7-3) help to choose the final elastic moduli. The nine independent coefficients

defining the elasticity of an orthotropic material are reduced to three (Gallerneau 95) in case of cubic anisotropy (additional symmetry of order 3 along the diagonal of the cube). For such a material, relation (7-67a) has a physical meaning. So, the assumption of a unique shear modulus is an extension of a cubic crystal property to textured polycrystal cubic material.

7.4.3. Identification of a classical Hill's matrix for plastic behavior

As described in section 7.4.5, this intermediate step is necessary in order to reach the required effective $(\bar{\sigma} \bar{\varepsilon})_i$ curves. So forgetting the frame of damage approach, the classical Hill's parameters must be adjusted from tensile experiments. The method proposed by Noat *et al.* 1995 has been chosen. The computed plastic parameters take into account both stress and strain measurements in a nice weighted way. However, this method was modified according to the plastic work equivalence assumption in each direction.

The classical Hill's model can be retrieved from (7-22, 7-23, 7-24) equations where no damage is assumed. This leads to the following expression:

$$F(\sigma_{22} - \sigma_{33})^2 + G(\sigma_{11} - \sigma_{33})^2 + H(\sigma_{11} - \sigma_{22})^2 + 2N\sigma_{12}^2 + 2L\sigma_{23}^2 + 2M\sigma_{31}^2 = 2\sigma_F^2 \quad (7-68)$$

Using axes transformation relation (7-62) and Hill's formula (7-68), the plastic stress for a tensile test in the α direction can be expressed by:

$$\sigma_H^2(\alpha) = \frac{2\sigma_F^2}{(H + G) + (F - G)\sin^4(\alpha) + (2N - 2H - G)\sin^2(\alpha)\cos^2(\alpha)} \quad (7-69)$$

Lankford's coefficient can be expressed by means of the normality rule applied to Hill's criterion. This gives the final result:

$$r_H(\alpha) = \frac{H - (F + G + 4H - 2N)\sin^2(\alpha)\cos^2(\alpha)}{F\sin^2(\alpha) + G\cos^2(\alpha)} \quad (7-70)$$

In relations (7-69) and (7-70), H index means: value deduced from Hill's plasticity, and in the following functional ϕ , exp index identifies values deduced from experiments:

$$\phi = \sum_{i=1,j} (1 - \eta) \left[\frac{\sigma_H(\alpha_i) - \sigma_{exp}(\alpha_i)}{\sigma_{Fexp}} \right]^2 + \eta [r_H(\alpha_i) - r_{exp}(\alpha_i)]^2 \quad (7-71)$$

where j gives the total number of different directions α_i explored by experiments, η is a weighting factor defining the weight of stress and strain measurements and $\sigma_{F exp}$ is the stress measurement average.

The set of parameters F, G, H, N is determined by minimizing the functional ϕ by a classical least square method for k different material states. Each material state k is characterized by its internal variable $(p)_k$ and by its plastic work $(W^p)_k$ estimated from the reference stress-strain curve. The experimental stress $\sigma_{exp k}(\alpha_i)$ in each direction α_i giving the same plastic work $(W^p)_k$ is selected and introduced in relation (7-71). Such a procedure leads to one set of $(F G H N)_k$ parameters for each studied plastic work $(W^p)_k$. From the general Hill's formula (7-68) and the knowledge of plastic work level, the required multi-linear stress-strain curves $(\sigma_{11} \epsilon_{11}), (\sigma_{22} \epsilon_{22}), (\sigma_{33} \epsilon_{33}), (\sigma_{12} \epsilon_{12})$ can be produced. As no information on $(\sigma_{13} \epsilon_{13})$ and $(\sigma_{23} \epsilon_{23})$ curves are available, they are assumed to be equal to $(\sigma_{12} \epsilon_{12})$ curve or, equivalently, $N=L=M$ can be used. As the physical reality of the material concerns stress and strain, η is chosen equal to 0,5, which means an equal weight for stress and strain prediction.

7.4.4. Identification of the damage model

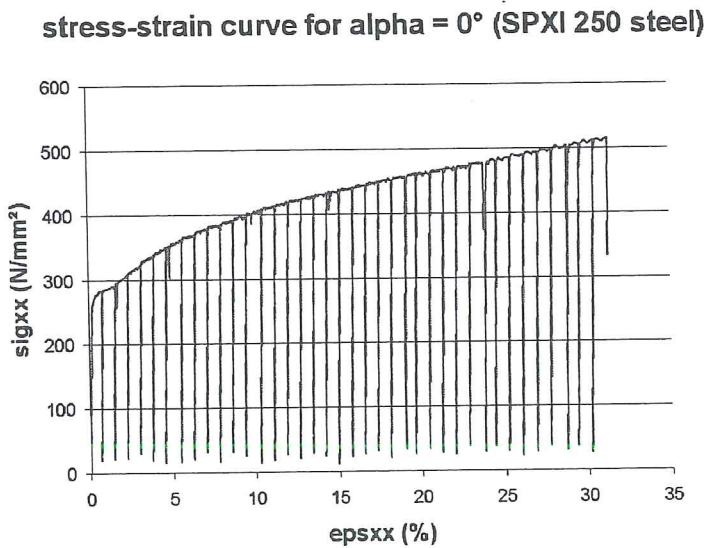


Figure 7-10 Loading-unloading cycles, tensile test in Rolling Direction, SPXI steel sheet (from Wauters 2000).

The required curves are the “damage energy release rate-damage” ones : $Y_i D_i$. From equation (7-10d) applied on a tensile test in direction i , one gets:

$$Y_i = \frac{\sigma_{ii}^2}{E_{0i}(1 - D_i)^3} \tag{7-72}$$

By means of loading-unloading cycles (Figure 7-10), the evolution of the effective Young's modulus $\bar{E}_i(\epsilon_{ii})$ is measured. This curve, associated with equation (7-18), gives the damage component evolution $D_i(\epsilon_{ii})$:

$$D_i(\epsilon_{ii}) = 1 - \sqrt{\frac{\bar{E}_i(\epsilon_{ii})}{E_{0i}}} \quad (7-73)$$

where E_{0i} is the initial value of the Young's modulus. This evolution is clear in Figure 7-11.

Evolution of the Young modulus E1 according to the plastic strain - test for alpha = 0° (SPXI 250 steel)

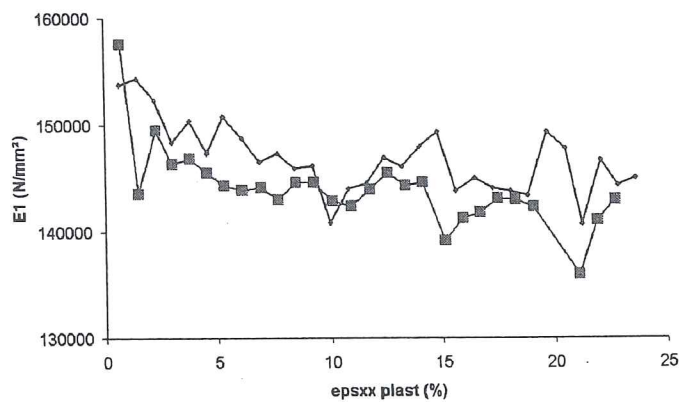


Figure 7-11 Decrease of Young's modulus measured by 2 sets of experiments, SPXI steel sheet (from Wauters 2000).

Evolution of the damage energy release rate Y1 according to the damage D1 - test for alpha = 0° (SPXI 250 steel)

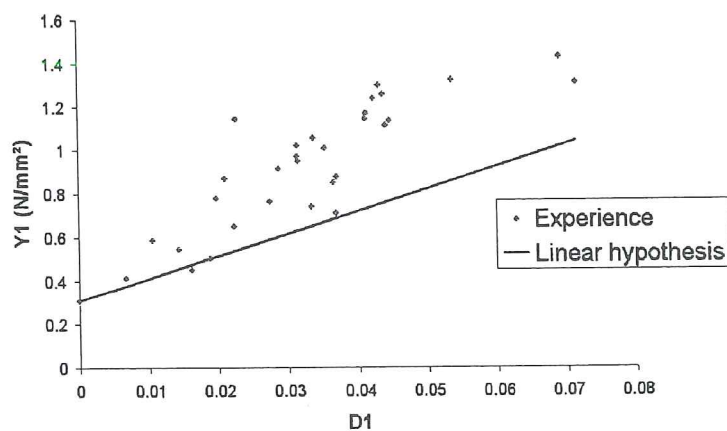


Figure 7-12 Linear description of the “damage energy release rate curve-damage” $Y(N/mm^2) - D$ for SPXI steel (from Wauters 2000).

As $\sigma_{ii}(\epsilon_{ii})$ is known by measurement and $D_i(\epsilon_{ii})$ is defined by equation (7-73), using equation (7-72), it is easily possible to produce points of $Y_i D_i$ curves for i equal 1 and 2. The experimental results shown in Figure 7-12 allow adjusting a simple linear model as proposed by Zhu 1992.

Concerning the thickness direction, such a direct approach cannot be applied because it is not possible to perform cyclic tensile test in this direction. However, the Y_{03} value can be directly deduced from equation (7-72), where D_3 is assumed to be equal 0 until plasticity entrance. For D_{13} value, a direct algebraic transformation of equation (7-18) and the thickness measurement during the performed tensile tests give:

$$D_3(\epsilon_{ii}) = 1 + \frac{V_{3i} \sigma_{ii}}{(1 - D_i(\epsilon_{ii})) E_3 \epsilon_{33}} \quad (7-74)$$

Knowing the damage work associated to ϵ_{ii} and assuming damage work equivalence in each direction, D_{13} can be obtained. As accuracy of thickness measurements is poor, D_{13} is really difficult to reach by this way.

In fact, the final approach to define $Y_i D_i$ curves is not the one described here above. The simplicity of the assumption of linear behavior reduces the free parameters to two per curve: Y_{0i} and D_{ii} . The first one is imposed by the hypothesis that damage begins at plasticity entrance. In consequence, Y_{0i} is directly given in uniaxial state by relation (7-72) with $D_i=0$ and $\sigma_{ii} = \sigma_{yi}$. The second parameter D_{ii} is fixed by the knowledge of σ_{maxi} maximal stress in direction i in case of uniaxial state. Replacing Y_i by its linear expression ($D_{ii} D_i + Y_{0i}$) in relation (7-72) yields a non linear equation $\sigma_i(D_i)$. For instance in direction 1:

$$\frac{\sigma_{11}^2}{E_{01}(1 - D_1)^3} = D_{11} D_1 + Y_{01} \quad (7-75)$$

The maximum of this non linear relation must coincide with σ_{max1} , so D_{11} is computed by the following relation:

$$\sigma_{1max} = \sqrt{\frac{27 E_{01}}{256 D_{11}^3} (D_{11} + Y_{10})^2} \quad (7-76)$$

As the 3 values σ_{maxi} can be deduced from Hill's yield locus determined on section 7.4.3, the damage parameters do not require any additional specific tests. This is of course very convenient but strongly limits the damage evolution that this model can reproduce. Consequently, the above described damage test provides the first validation of the model. Figure 7-12 compares experimental points to the linear behavior of (Y-D) curve.

7.4.5 Computation of effective stress-strain curves

The previous experiments, analytical analysis and hypothesis give:

- $(\bar{\sigma}_{ii} \bar{\epsilon}_{ii})$ multi-linear curves for $i = 11, 22, 33, 13, 32, 12$ (see sections 7.4.2 and 7.4.3) ;
- $Y_i D_i$ linear curves for $i = 11, 22, 33$ (see section 7.4.4).

Using relation (7-75) describing a uniaxial test in one direction allows computing damage evolution. Then $(\bar{\sigma}_{ii} \bar{\epsilon}_{ii})$ curves are easily obtained for directions 11, 22, 33 by means of relations (7-2) and (7-3). For shear curves 23, 31, 12, analytical work provides damage evolution. Relation (7-10d) gives, in case of pure shear in 12 direction:

$$-Y_1 = \frac{\sigma_{12}^2}{2G_{12}^0(1-D_1)^2(1-D_2)} \quad -Y_2 = \frac{\sigma_{12}^2}{2G_{12}^0(1-D_1)(1-D_2)^2} \quad (7-77)$$

Then, the equivalent damage energy release rate Y_{eq} is computed by relation (7-32):

$$Y_{eq} = Y_1 + \sqrt{J_2} Y_2 \quad (7-78)$$

where J_2 is defined by (7-34).

The damage surface (7-31) imposes a first constraint:

$$Y_{eq} - (D_{11}D_1 + Y_{10}) = 0 \quad (7-79)$$

and the second relation required to solve $D_1 D_2$ is the equivalence of damage work (Figure 7-2):

$$\frac{D_1(Y_1 + Y_{10})}{2} = \frac{D_2(Y_2 + Y_{20})}{2} \quad (7-80)$$

$$Y_1 = D_{11}D_1 + Y_{01} \quad \text{and} \quad Y_2 = D_{12}D_2 + Y_{02} \quad (7-81)$$

The resolution of the system (7-79; 7-80), with the additional assumption of increasing damage, provides the damage evolution $D_1 D_2$ in pure shear state. This approach is repeated for each shear direction and the effective shear curves $(\bar{\sigma}_{ij} \bar{\epsilon}_{ij})$ are easily obtained for directions 23, 31, 12 using relations (7-2) and (7-3).

7.5 Model identification for two different steel sheets

The above procedure has been applied on a classical deep drawing steel sheet (IF ULC Ti) and a "high-tensile" steel sheet (SPXI), both 0,8 mm thick. Microscopic investigations about these two materials are not discussed here. They are part of Wauters' Ph. D. thesis, which is still in progress. Table 7-3 gives the final set of elastic

parameters (called “experiment”) issued from the various experiments described in section 7.4. A comparison is proposed with the values (called “texture”) computed by professor van Houtte’s team from texture measurements of non deformed samples. Repeating the computation of elastic parameters from texture measurements performed on deformed samples, it has been verified that, for these two steels and for tensile tests performed in rolling and transversal direction, texture evolution does not modify these computed “texture” elastic values (see Figure 7-13). One can conclude that damage is responsible for Young’s modulus decrease observed for instance on Figure 7-11.

SPXI steel						
	E ₁	E ₂	E ₃	G ₁₂	G ₁₃	G ₂₃
Texture	205834	204256	196748	80385	85220	86231
Experiment	203407	209274	206341	77268	77268	77268
Gap (%)	1.19	2.4	4.65	4.03	10.29	11.6
	v ₁₂	v ₂₁	v ₁₃	v ₃₁	v ₂₃	v ₃₂
Texture	0.2748	0.2727	0.3135	0.2995	0.3188	0.3070
Experiment	0.2884	0.2967	0.3135	0.3180	0.3188	0.3143
Gap(%)	4.7	8.09	0.00	5.81	0.00	2.33
IF ULC Ti steel						
	E ₁	E ₂	E ₃	G ₁₂	G ₁₃	G ₂₃
Texture	207954	206048	201789	80796	80796	80796
Experiment	204129	185016	194573	82993	82993	82993
Gap (%)	1.87	11.37	3.71	2.65	0.57	2.01
	v ₁₂	v ₂₁	v ₁₃	v ₃₁	v ₂₃	v ₃₂
Texture	0.2813	0.2787	0.3028	0.2937	0.3092	0.3027
Experiment	0.3371	0.3055	0.3028	0.2884	0.3092	0.3251
Gap(%)	16.55	8.78	0.00	1.77	0.00	6.90

Table 7.3 Elastic material parameters, Young’s moduli in N/mm² (from Wauters 2000).

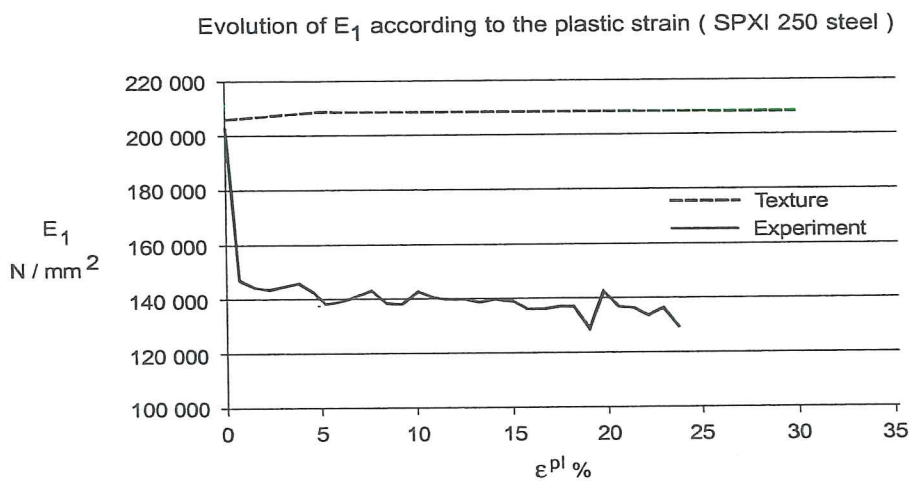


Figure 7-13 Young’s modulus of SPXI steel from loading-unloading cyclic tensile tests or deduced from texture measurements (from Wauters 2000).

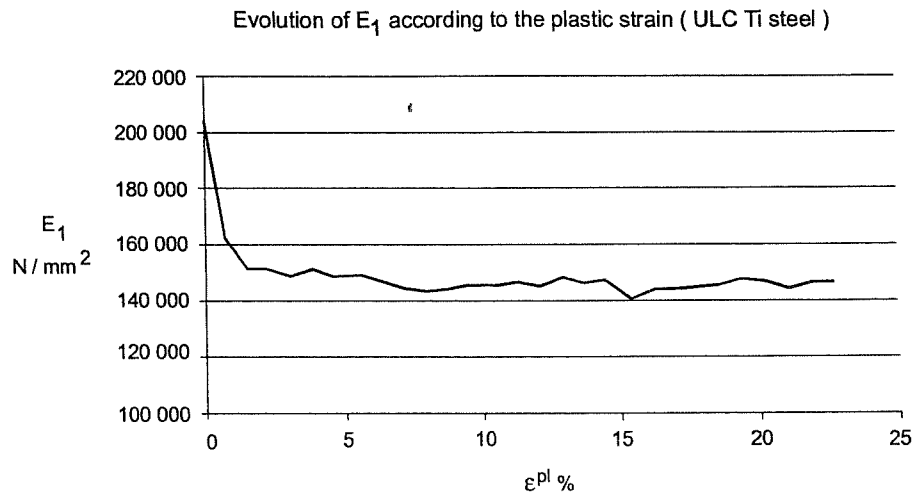


Figure 7-14 Young’s modulus evolution during tensile test in Rolling Direction, IF ULC Ti steel (from Wauters 2000).

The decrease of Young’s modulus at plasticity entrance and with damage has already been discussed in Chapter 3, section 3.2.1. Such results have also been presented in Chapter 6, section 6.2.7 for an aluminum alloy.

The identification of Hill’s parameters has been performed by means of tensile tests in large strains in seven directions ($\alpha = 0, 15, 30, 45, 60, 75, 90$) and with the weighting coefficient η equal to 0,5. The four resulting stress strain-curves in 1, 2, 3 directions and in 12 shear state are given in Wauters’ 2000 DEA thesis for both steel sheets. The shear behaviors in 23, 13 directions are assumed identical to 12 direction.

SPXI steel					
Y_{10}	Y_{20}	Y_{30}	DT_1	DT_2	DT_3
0.3055	0.2989	0.2914	10.802	10.885	12.265

IF ULC Ti steel					
Y_{10}	Y_{20}	Y_{30}	DT_1	DT_2	DT_3
0.0623	0.0649	0.0647	7.96	8.33	15.769

Table 7.4 Linear data describing “damage energy release rate-damage” curves (from Wauters 2000).

The results of damage identification are summarized in Table 7.4. Figure 7-14 shows Young’s modulus evolution for the IF ULC TI steel. The decrease of Young’s modulus for this IF steel is not as clear as the one of SPXI steel but still exists. Figure 7-15 presents the result of damage computation during a simulated tensile test

and the value computed using relation (7-18) and experimental observations. The latter value is directly computed with the initial Young's modulus and not with Young's modulus after plasticity. The possible choices have already been discussed in section 6.2.7.

Evolution of D_1 according to the plastic strain (SPXI 250 steel)

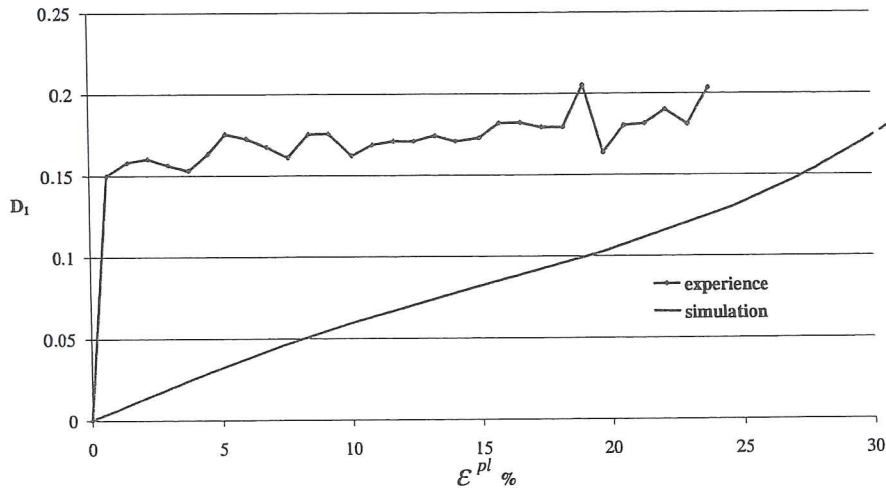


Figure 7-15 Simulated and measured damage component 1, during a tensile test, SPXI steel (from Wauters 2000).

With these final sets of parameters, a uniaxial tensile test in Rolling direction is simulated for each studied steel. Figure 7-16 and 7-17 compare experimental and simulated true stress-strain curves and present effective stress-strain curves.

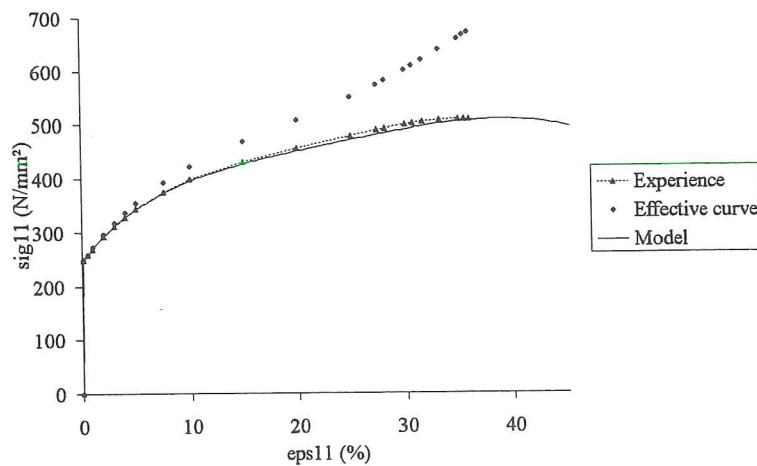


Figure 7-16 Stress-strain curves for a uniaxial tensile test, SPXI steel (from Wauters *et al.* 2000).

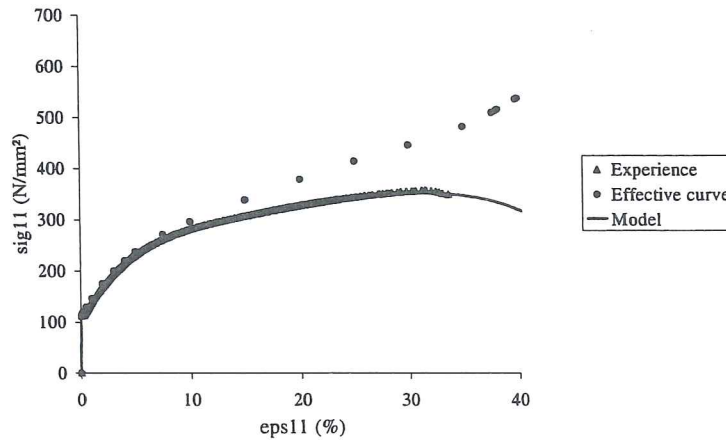


Figure 7-17 Stress-strain curves for a uniaxial tensile test, IF ULC TI steel (figure provided by Wauters, not yet published).

The model accurately reproduces the experimental tests.

7.6. Yield locus

Figure 7-18 shows the evolution of the global yield locus shape and size due to the damage and plastic processes during a tensile test in Rolling Direction. The assumption of energy equivalence in each direction to define hardening behavior induces a slight shape modification superposed with a strong increase of the yield locus size. If one looks at the “yield locus without damage”, the perfect symmetry around the diagonal line present in the “initial yield locus” has been lost. When the coupled elasto-plastic-damage model is used, one can observe an additional change of shape as well as a decrease of the yield locus due to damage.

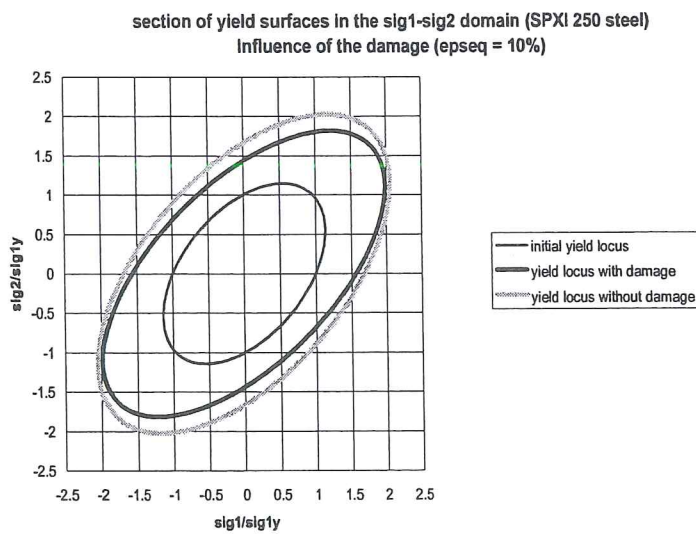


Figure 7-18 Initial and predicted yield loci of SPXI steel (from Wauters *et al.* 2000).

7.7 Validation

7.7.1 FLD prediction

The Forming Limit Diagram and Marciniak-Kuczynski's approach have already been presented in Chapter 4. The first validation is the prediction of FLD diagram with the developed model.

As shown on Figure 7-19, the application of the model with the parameters defined on section 7.5 is quite far from the reality. A modification (Figure 7-20) of the slope of $Y_i - D_i$ curve provides a better correlation. This fact demonstrates how difficult it is to define this slope. The best solution should result from the inverse analysis of a set of experiments. The linear choice for $Y_i - D_i$ curve is perhaps very simple but too poor to give accurate predictions.

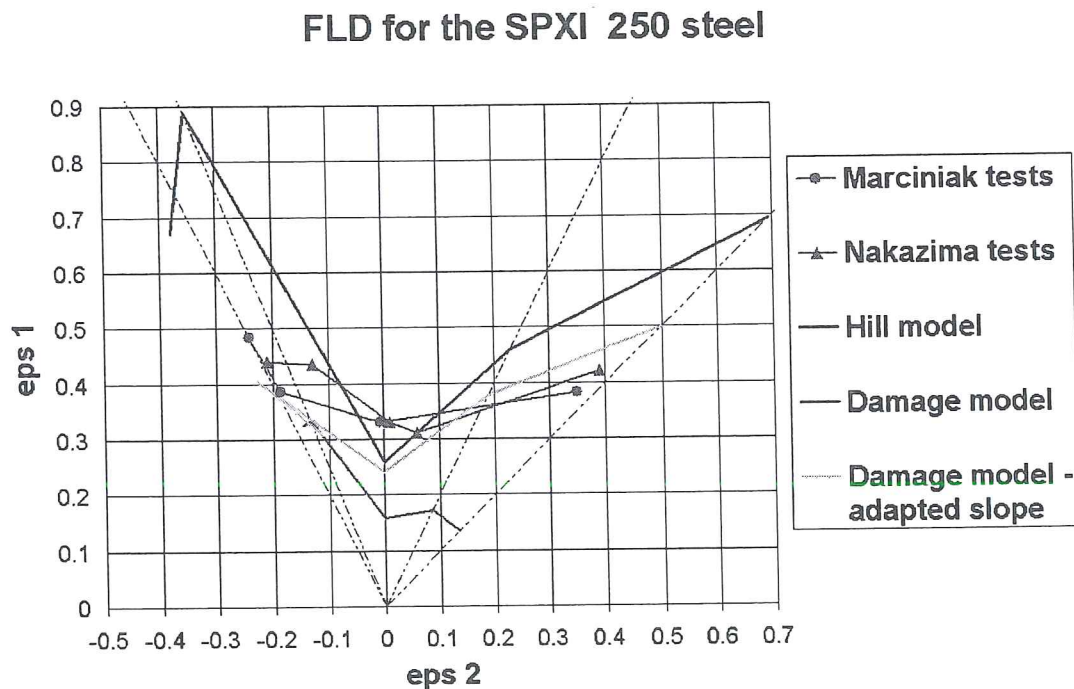


Figure 7-19 FLD predictions and measurements for SPXI steel (from Wauters *et al.* 2000).

**Evolution of the damage energy release rate $Y1$
according to the damage $D1$ - test for $\alpha = 0^\circ$
(SPXI 250 steel)**

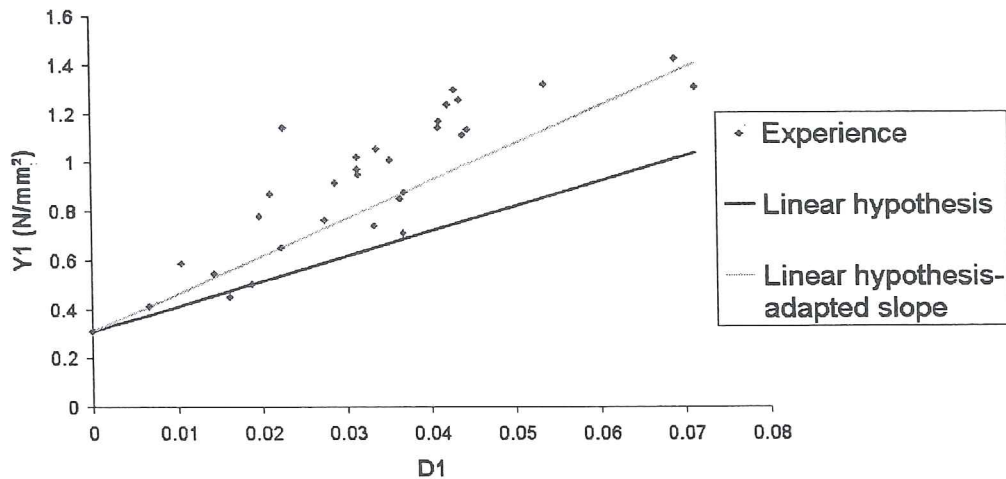


Figure 7-20 Damage energy release curves (Wauters *et al.* 2000).

7.7.2 Finite element simulations

Zhu's thesis 1992 already presented experiments and simulations such as hemispherical punch stretching or deep drawing by cylindrical and square punches, where data were adjusted on literature. Biaxial Nakazima's tests performed on the studied steel sheets have been simulated. These tests can be described by the following features:

- initial rectangular blank 0.8 mm thick;
- spherical punch with a radius of 80 mm;
- Coulomb's friction coefficient of 0,05;
- blankholder shape and die shape are defined on Figure 7-21.

The simulations are computed with the LAGAMINE code. The volume finite element discretization consists in one layer of 705 8-nodes mixed elements. The tools are modeled by a spherical segment for the punch and two sets of 20 and 140 triangles respectively for the blankholder and die. The contact problem is treated by 1410 surface contact elements based on a penalty approach with a penalty coefficient of 500 Mpa/mm³. The simulation is driven by the vertical punch displacement and is stopped for a punch depth of 32 mm. By symmetry only one quarter of the experiment is simulated. Figure 7-22 presents the equivalent strain at the punch depth of 30 mm; the material dependence is clearly illustrated. The IF ULC Ti steel shows a large distribution of the strain while the SPXI steel has a more localised strained zone with higher strain level. The equivalent damage component is very

interesting; again a different behavior can be verified for each steel (Figure 7-23). The rupture localization predicted by the higher value of damage is in good concordance with the experimental crack (Figure 7-24).

As underlined by experimenters, Marciniak's tests are very sensitive to friction. Some scientists doubt that the different material behaviors induce the crack localization. As great care has been given to the material surface state and lubrication, some confidence is given to this validation. However, it is clear that additional validations would be welcome.

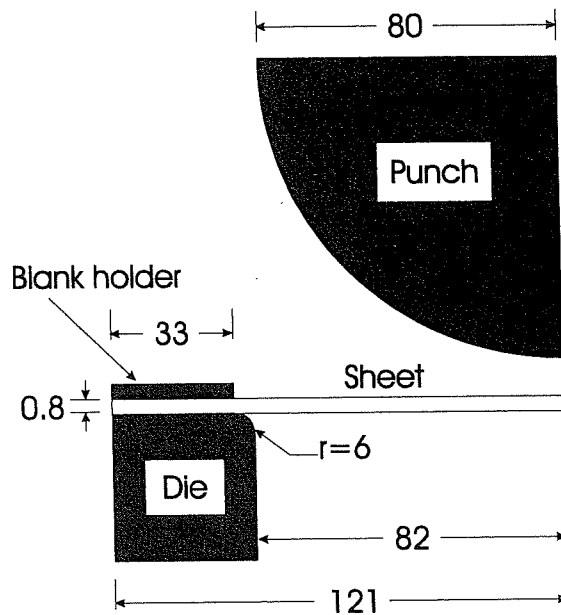
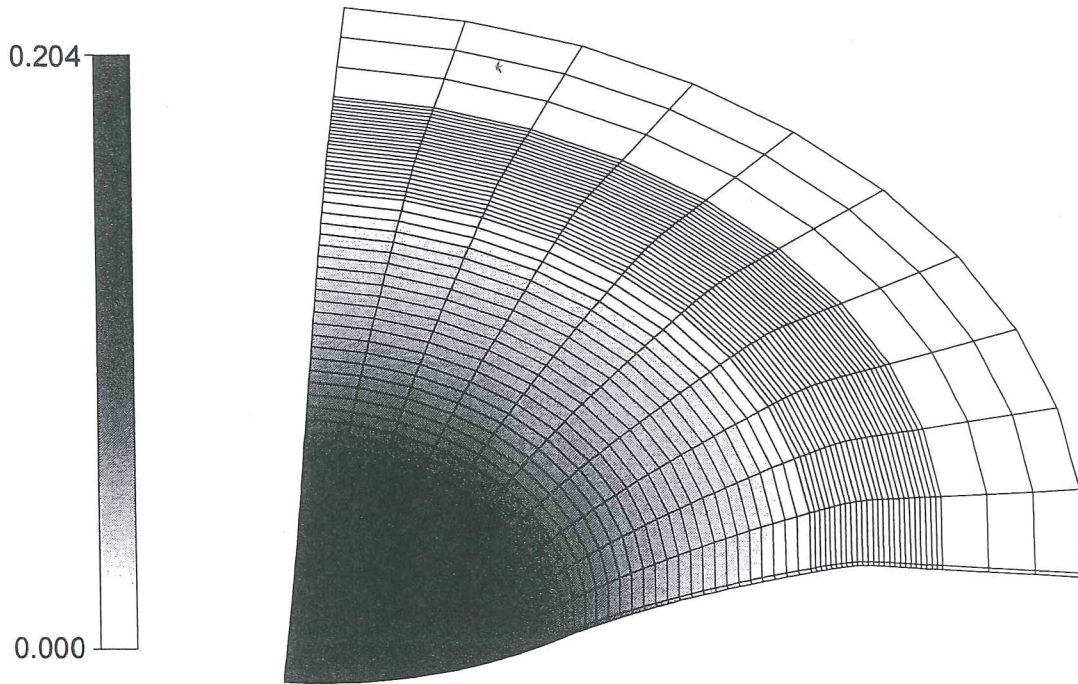
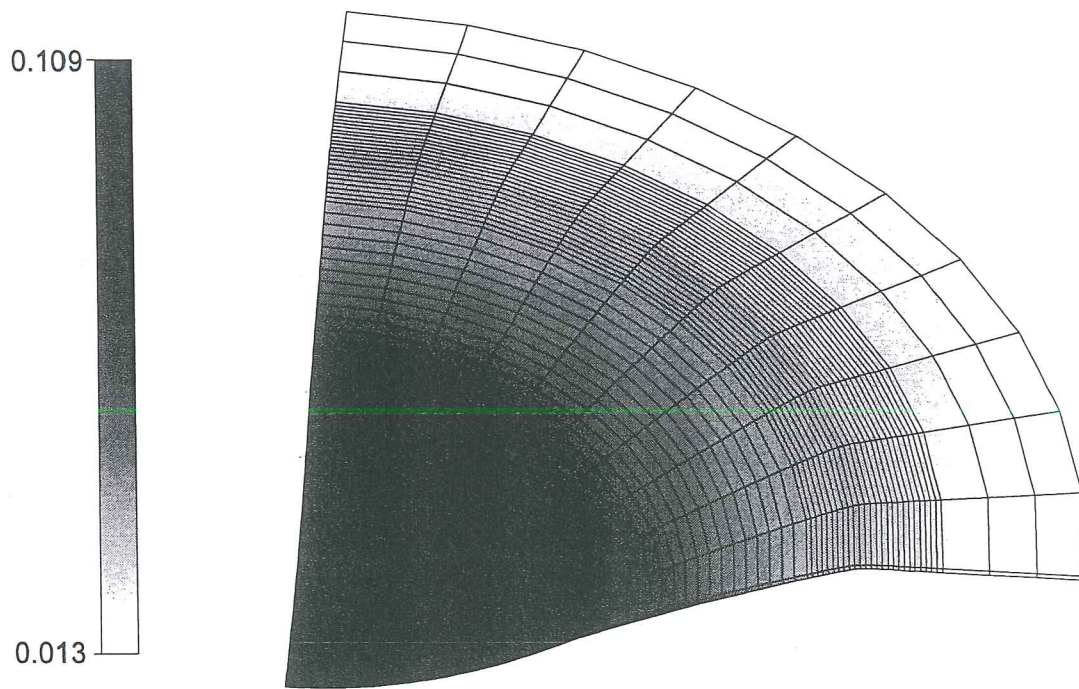


Figure 7-21 Description of Nakazima biaxial test (from Habraken 1999).

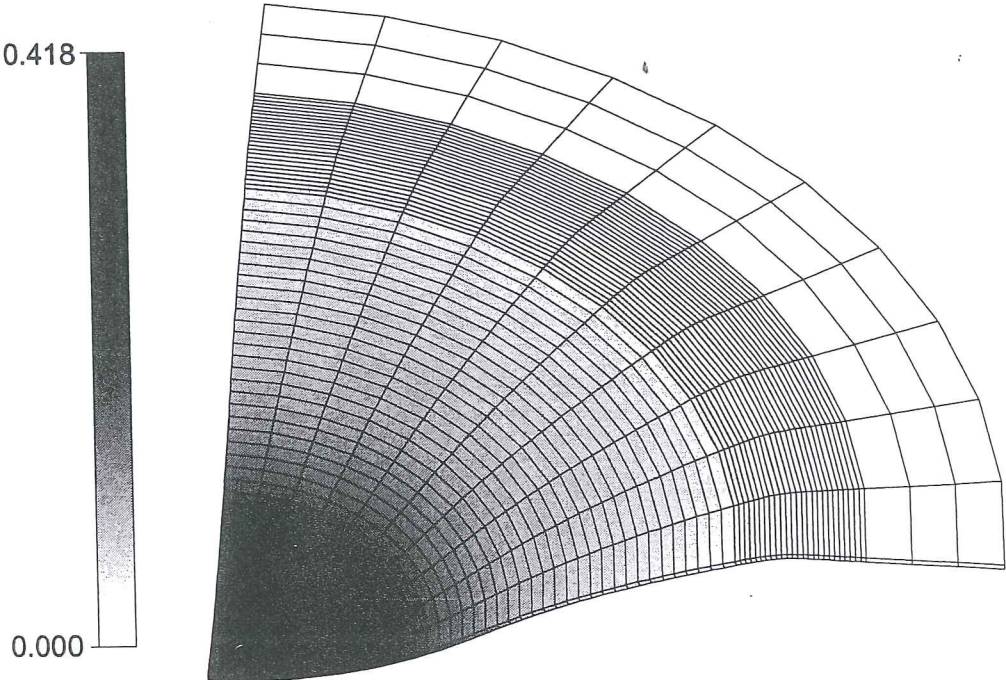


SPXI steel

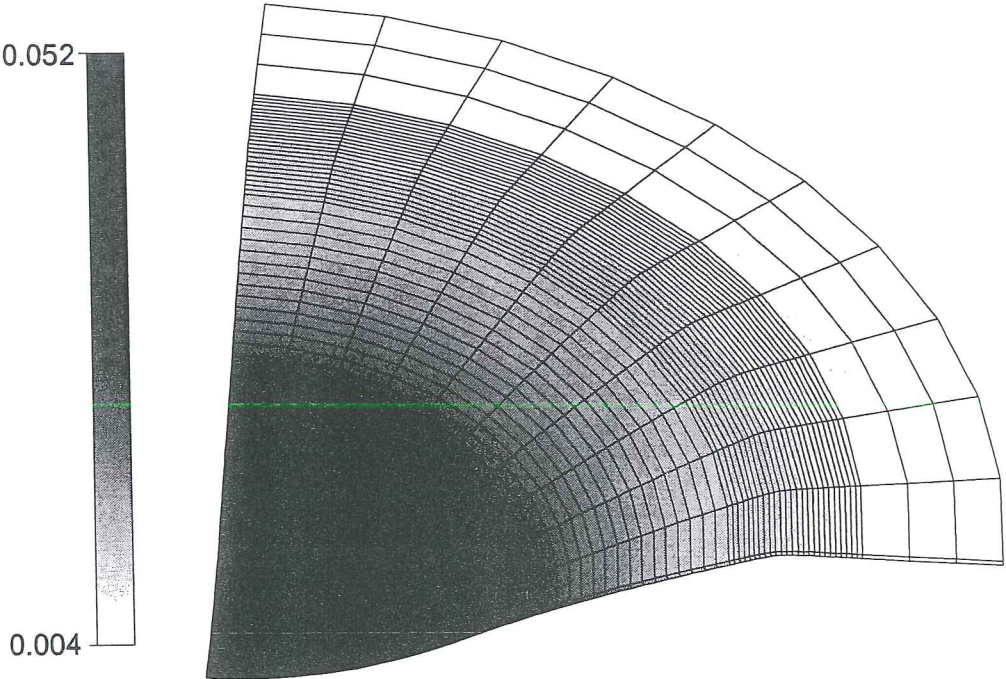


IF ULC Ti steel

Figure 7-22. Equivalent strain distribution for a punch depth of 30 mm (from Charles *et al.* 1997).

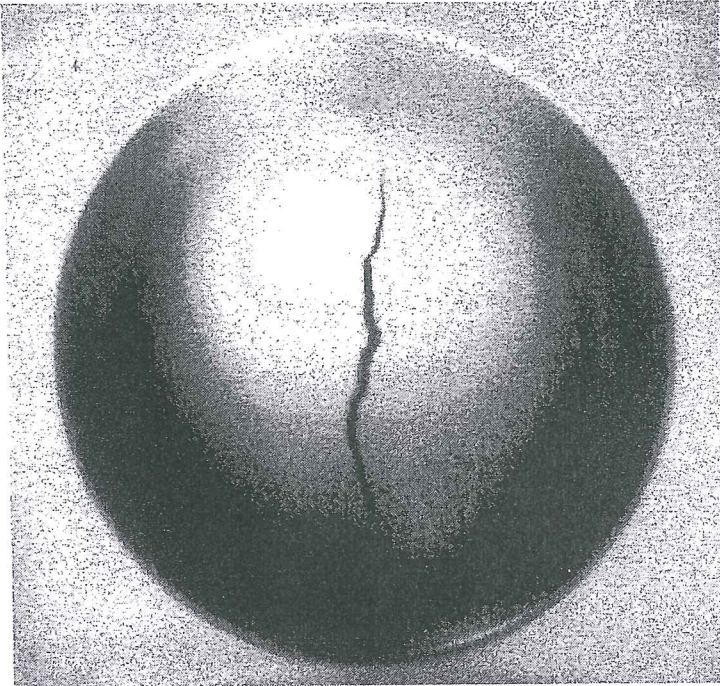


SPXI steel

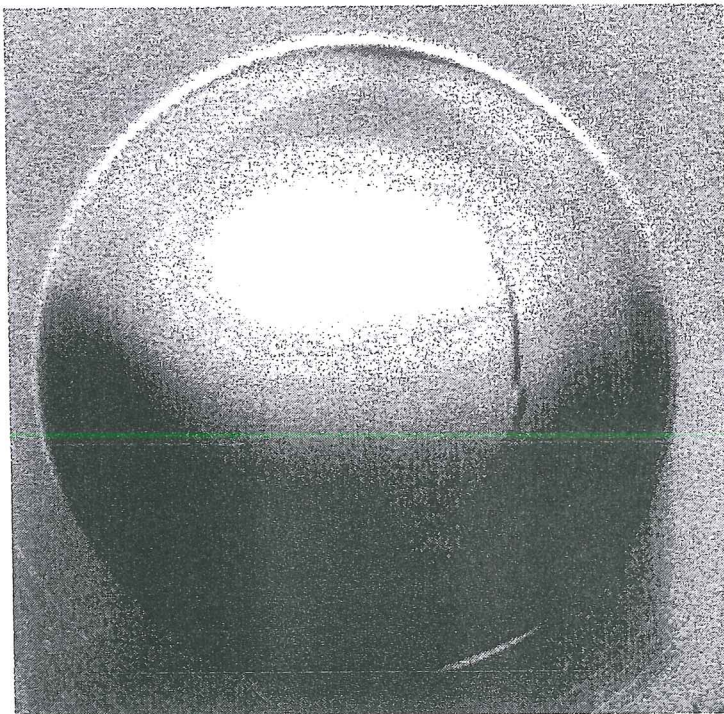


IF ULC Ti steel

Figure 7-23 Equivalent damage distribution for a punch depth of 30 mm (from Charles *et al.* 1997)



SPXI steel



IF ULC Ti steel

Figure 7-24 Nakazyma's tests, punch displacement 69 mm
(from Habraken 1999).

7.8 Conclusion

To conclude, one can tell that the anisotropic model developed by Zhu 1992 has been improved. Now, this constitutive law proposes multiple linear segments to describe the hardening plastic curve. An experimental approach has been defined to determine the material parameters. The simple choice of a linear description of the damage energy release rate–damage curve has been proposed. It allows a quick identification process of the anisotropic elasto-plastic-damage model, without damage experiment. However, the performed damage experiments and the validation simulations (section 7.7.1) show that this choice has a limited range of applications. The slope curve is not easy to determine (section 7.4.4) and should result from a compromise between tensile stress-strain curves and FLD prediction. To increase the flexibility and accuracy of the model, one possibility is to use multi linear curves for damage energy release rate–damage curve.

An interesting result of this study consists in the fact that both studied steel sheets present Young's modulus decrease, which cannot be attributed to texture evolution. This damage effect, that is not well known, was interesting to verify.

Further experimental validations of the assumption of energy equivalence in each direction are required. Simulation of deep drawing processes, where cracks occur, should also be done to go on with the damage validation step. This work is still in progress.

References

- Bockler, J.P., El Aoufi, L., Raclin, S. (1987) On experimental testing method for anisotropic materials, *Res Mechanica*, **21**, 73-95.
- Cambron, A-F. (1997), La prédiction de fissures, Travail de fin d'études, Ingénieur physicien, Université de Liège.
- Charles, J.F., Habraken, A.M. (1996) Dépouillement des essais de traction nécessaires à la calibration de la loi anisotrope élastoplastique avec endommagement de Y.Y. Zhu, Convention Région Wallonne n°2748, rapport intermédiaire n° 9.
- Charles, J.F., Zhu, Y.Y., Habraken, A.M., Cescotto, S., Traversin, M. (1997) A fully elasto-plastic damage theory for anisotropic materials, in *Advanced Methods in Materials Processing Defects*, Predeleanu, M., Gilormini, P. editors, Elsevier Science.
- Charles, J.F., Habraken, A.M. (1998) Amélioration de la version 3D de la loi Norton-Hoff, Convention Région Wallonne n°2748, rapport intermédiaire n° 24.
- Chow, C.L., Wang, J. (1987) An anisotropic theory of elasticity for continuum damage mechanics, *Int. J. Fracture*, **33**, 3-16.
- Cordebois, J.P., Sidoroff, F. (1979) Damage induced elastic anisotropy, F. *Euromech*, **115**.

- Cordebois, J.P. (1983) Critères d'instabilité plastique et endommagement ductile en grandes déformations, applications à l'emboutissage, Doctoral Thesis, Paris.
- Estevez, R., Habraken, A.M. (1996) Calibration method of an anisotropic elastoplastic model coupled with damage, *Nuphymat'96*, Workshop on numerical and physical study of material forming processes, final meeting, CEMEF, Sophia-Antipolis, Final Report.
- Gallerneau, F. (1995) Etude et modélisation de l'endommagement d'un superalliage monocristallin revêtu pour aube de turbine, Thèse Docteur en sciences et génie des matériaux, Ecole Nationale Supérieure des Mines de Paris.
- Golin, J.C., Danescu, A. (1992) Constitutive model and computational strategies for finite-strain elasto-plasticity with isotropic or anisotropic ductile damage, *3rd COMPLAS int. conf.*, D.R.S. Owen et al. editors, *Pineridge Press*, 1413-1424.
- Godinas, A., Cescotto, S. (1984) Calcul des gradients de vitesses constants au cours d'un pas, rapport interne MSM n° 159, Université de Liège.
- Gologanu, M., Leblond, J.B., Devaux, J. (1994) Numerical and theoretical study of coalescence of cavities in periodically voided solids, *Computational Material Modeling*, ASME, AD- 42/PVP- 294.
- Gurson, A.L. (1977) Continuum theory of ductile rupture by void nucleation and growth. *J. Engng. Materials Technology*, **99**, 2-15.
- Habraken, A.M. (1999) Prise en compte des interactions micro-macro dans la modélisation par éléments finis de la mise à forme des métaux, Convention Région Wallonne n° 2748, Rapport final.
- Hayakawa, K., Murakami, S. (1998) Space of damage conjugate force and damage potential of elastic-plastic-damage materials, *Damage Mechanics in Engineering Materials*, Voyiadjis, G.S., Ju, J.W., Chaboche, J.L. Eds, 27-44.
- Hoferlin, E., van Bael, A., van Houtte, P., Teododiu, C. (1999) An accurate model of texture and strain-path induced anisotropy, *Proc. 4th Int. Conf.: Numerical Simulation of 3-D Sheet Metal Forming Processes. NUMISHEET'99*, Ed. J.C. Gélín and P. Picart, University of Franche Comté
- Hoferlin, E. (2001), Incorporation of an accurate model of texture and strain-path induced anisotropy in simulations of sheet metal forming, Ph. D thesis , Hatholieke Universiteit Leuven
- Hill, R. (1948) A theory of the yielding and plastic flow of anisotropic materials. *Proc. Royal Soc. London*, **A193**, 281-297
- Lemaître, J., Chaboche, J.L. (1985) *Mécanique des matériaux solides*, Dunod, Paris.
- Lemaître, J. (1986), Local approach of fracture, *Eng. Fracture Mech.*, **25**, 523-537.
- Lu, T.J., Chow, C.L. (1990) On constitutive equations of inelastic solids with anisotropic damage, *J. Theory Appl. Fract. Mech.*, **14**, 187-218.
- Munhoven, S., Habraken, A.M., Van Bael A., Winters J. (1996b) Anisotropic finite element analysis based on texture. *Proc. 3rd Int. Conf.: Numerical Simulation of 3-D Sheet Metal Forming Processes. NUMISHEET'96*, Ed. L.K. Lee, G.L. Kinzel, R.H. Wagoner, The Ohio State University, Columbus, 112-119.

- Noat, P., Montmitonnet, P., Chastel, Y., Shahani, R. (1995) Anisotropic 3-D modelling of hot rolling and plane strain compression of Al alloys, *Simulation of Materials Processing*, 959-964.
- Ponthot, J.P. (1995) Mécanique des milieux continus solides en grandes transformations et traitement unifié par la méthode des éléments finis, Ph. D thesis, University of Liège
- Szabo, L. & Balla, M. (1989) Comparison of some stress rates, *Int. J. Solids&Structures*, **25**, 279-297.
- Szabo, L. (1985) Evaluation of elasto-viscoplastic tangent matrices without numerical inversion, *Comp. & Struct.* **21**, 1235-1236.
- Teodosiu, C., Hu, Z. (1998) Microstructure in the continuum modelling of plastic anisotropy, Proceedings of the 19th Riso Int. Symp. on Materials Science : Modelling of Structure and Mechanics of Materials from Microscale to Products, Carstensen, J.V., Leffers, T. Eds.
- Valliappan, S., Boonlaulohr, P., Lee, I.K., (1976) Non-linear analysis for anisotropic materials, *Int. J. Num. Meth. in Eng.*, **10**, 597-606.
- Wauters, M. (1997) Etude de la rupture des matériaux métalliques : approche expérimentale et simulations numériques par éléments finis couplés à la théorie de l'endommagement, FRIA, rapport annuel.
- Wauters, M. (1998), Etude de la rupture des matériaux métalliques : approche expérimentale et simulations numériques par éléments finis couplés à la théorie de l'endommagement, FRIA, rapport annuel.
- Wauters, M. (1999) Etude de la rupture des matériaux métalliques : approche expérimentale et simulations numériques par éléments finis couplés à la théorie de l'endommagement, FRIA, rapport annuel.
- Wauters, M. (2000) Calibration of an anisotropic elasto-plastic damage model for sheet metal forming, Diplôme d'Etudes approfondies en Sciences Appliquées, Université de Liège.
- Wauters, M., Habraken, A.M., Duchêne, L. (2000) A fully elasto-plastic damage model applied to anisotropic materials, Proceedings of 14th Engineering Mechanics Conference, Austin Texas, USA.
- Zhu, Y.Y. (1992) Contribution to the local approach of fracture in solid dynamics, Ph. D. Thesis, University of Liège, Department MSM.
- Zhu, Y.Y., Cescotto, S. (1995) A fully coupled elasto-visco-plastic damage theory for anisotropic materials. *Int. J. Solids & Structures*, **32-11**, 1607-1641.

8. CONCLUSIONS

An overview of damage models applied to ductile rupture has been proposed to the reader, providing background for the macroscopic models developed in MSM and described in Chapters 6 and 7.

Concerning rupture during sheet metal processes, Chapter 4 enhances the interest of criteria, such as those developed by Hora-Brunet or Boudeau-Gelin. The advantage of Thomason's criterion, based on microscopic roots and coupled with macroscopic results, has also been demonstrated. However, this latter criterion requires microscopic data. So it can only be applied if mechanical and metallurgical teams work together to study a material. The last investigated direction is rupture criteria based on energy consideration, as in fracture mechanics. Damage models developed by MSM have not yet been coupled with these criteria. This could be included in a possible extension of this work.

The thesis is limited to rupture detection, and the implemented models do not apply to the study of crack propagation as explained in chapter 5. Even for rupture detection, some mesh dependency problems appear when damage elasto-plastic models are used (see section 6.3). This problem also provides a development direction for further study.

This research on macroscopic models will go on. For instance, the validation of the anisotropic damage-elasto-plastic model is clearly not achieved.

The purely macroscopic mechanical experimental approach has prevented the use of interesting parameters such as the material characteristic length to define finite element sizes or apply Thomason's criterion. So for future research, collaborations with the metallurgy service are foreseen to provide such information.

Microscopic aspects are very important and a micro-macro approach such as that of Chaboche & Feyel 2001 seems very interesting from a scientific point of view. These authors use, at each integration point of the FE macroscopic mesh, another finite element mesh to study the material behavior on a microscopic scale with an elastoviscoplastic and damage constitutive law. Such research provides basic understanding of rupture and this will probably give new components to include in macroscopic models. However, even if parallel computation opens new dreams, macroscopic approaches (Gurson's model or Lemaître's law) retain their interest. They cover different types of loading and can provide a reliable prediction of rupture. They are easily included into a forming process optimization where free parameters are tool shape, sheet thickness and low value of damage parameters. To conclude, even if the micro-macro link is important to investigate and can provide new trends to develop new materials, the classical macroscopic approach still has a role to play in practical industrial problems.

Reference

Chaboche, J.L., Feyel, F. (2000) On the multiscale analysis of composite structures by using FE² technique and fibre-matrix damage mechanics, *Continuous Damage and Fracture*, Benallal, A. editor, Elsevier.

PART D

CONCLUSIONS AND PERSPECTIVES

**Thèse présentée en vue de l'obtention du grade d'Agrégé de l'Enseignement
Supérieur
par Anne-Marie HABRAKEN**

Année académique 2000-2001

CONCLUSIONS AND PERSPECTIVES

Two types of material constitutive laws for finite element models have been investigated: micro-macro approaches based on texture analysis and damage models. In each case, the proposed literature review helps to understand the context of the models developed by the MSM team.

In the texture field, this thesis summarizes in a first step the results of the MSM collaboration with Professor van Houtte: the implementation of a 6th order yield locus in the stress space and the use of his Taylor's software. In a second step, original proposals are described. The hyperplane method was developed; however its stability and convergence were not sufficient. Consequently, a second idea, in which more attention is given to continuity requirements, has been proposed. It consists in a new interpolation method, rather than an additional yield locus function. This interpolation approach can be considered as an extension to the five dimensional deviatoric stress space of the concept of isoparametric finite elements. The interest of this yield locus local description is linked to the goal of following texture evolution during FE computation. It is clear that if this evolution can be neglected, an accurate global yield locus function requires less CPU time. Validation of this method as well as optimization of its parameters to provide low CPU time is currently in progress with Laurent Duchêne's Ph. D. thesis.

In the damage field, the summarized research is characterized by the fact that new models are not only proposed but also applied to a large set of different loading states. Their numerical implementation, the identification of their parameters as well as their validation have been conducted. The damage extension of Bodner's elasto-visco-plastic law is able to localize a rupture event with simple damage criteria such as the threshold value of the damage parameter in a limited range of triaxiality value. The limits of an isotropic damage elasto-plastic model applied to the same experimental set as above Bodner's model have been demonstrated. Improvements of the anisotropic elasto-plastic model proposed by Zhu have been implemented. A method to identify these model parameters has been proposed; a simple choice can even ignore damage measurements. New skills have been developed in the MSM laboratory to provide accurate Young's modulus measurements and to perform tensile tests away from material anisotropy axes. An optimization of the sample shape according to the measurement devices has been performed. These results are available for next experiments to identify the parameters of the anisotropic damage model applied to sheet. For a classical deep drawing steel and a high tensile steel, the decrease of Young's modulus with plastic strain has been verified. The advantages and limitations of macroscopic damage models are defined.

The important state-of-the-art study performed for this thesis allows using it as material for third cycle courses and provides perspectives for further work. Some possible extensions or new fields connected to this research are as follows:

- Development of parallel computation adapted to the MSM micro-macro model based on texture analysis;
- Further investigation to find criteria telling when a texture updating is required;
- Implementation of a more sophisticated hardening rule in the MSM micro-macro model based on texture analysis;
- Development of experiments to identify this sophisticated hardening rule;
- Investigation of the variational multi-scale approach;
- Implementation of new criteria to detect damage;
- Development of non-local or gradient formulation of damage elasto-plastic laws;
- Mesh adaptation: the idea is to study an industrial process with a macroscopic damage model, then where possible rupture is detected, to remesh and provide a finer analysis of microscopic event;
- Specific development of finite elements able to model crack propagation;
- Robust inverse models to identify model parameters thanks to finite element simulations of experiment.

At the beginning of the thesis, applications of both anisotropic models developed for metal sheets (texture-based model described in Chapter 6, part B, and damage model described in Chapter 7, part C) were planned on both studied steel sheets (high tensile steel sheet or classical deep drawing steel sheet):

- FLD prediction;
- complete finite element simulations of biaxial Marciniak test.

However, as such results are not yet ready, they should be included in Duchêne's thesis (2001, 2002?). Note that, for a very large set of steel grades, Cayssials's approach provides an efficient way to predict FLD. Thus, FLD prediction is no longer such an important goal to save time and money, but rather becomes a validation step of a constitutive law. If Marciniak's approach is used, the result also depends on the size of the imposed defect; thus the constitutive law is not the only factor defining the reliability of the prediction.

A set of cup drawing experiments are available for the two steel grades studied; the prediction of their accurate final shape and final texture will therefore provide an additional validation of the developed constitutive laws.

To summarize, parts B and C of this thesis describe Habraken's scientific involvement in two fields: micro-macro models and damage models. Appendices 1 and 2 give an idea of the thermo-metallurgical-mechanical laws developed to simulate hot forming processes and to study recrystallization phenomena. One model of contact between two deformable bodies is proposed in the third appendix.

Reference

Cayssials, F. (1998) A new method for predicting FLC, IDDRG, Conference Geneval, Brussels 6/98.